Order Number 9215862

# Modeling the biodegradation kinetics of dissolved organic contaminants in a heterogeneous two-dimensional aquifer

Odencrantz, Joseph Eric, Ph.D.

University of Illinois at Urbana-Champaign, 1992

U·M·I
300 N. Zeeb Rd.
Ann Arbor, MI 48106

# MODELING THE BIODEGRADATION KINETICS OF DISSOLVED ORGANIC CONTAMINANTS IN A HETEROGENEOUS TWO-DIMENSIONAL AQUIFER

BY

JOSEPH ERIC ODENCRANTZ

B.S., University of Maine, 1984
M.S., University of Illinois, 1986

THESIS

Submitted in partial fulfillment of the requirements for
the degree of Doctor of Philosophy in Civil Engineering
in the Graduate College of the
University of Illinois at Urbana-Champaign, 1992

Urbana, Illinois

UNIVERSITY OF ILLINOIS AT URBANA-CHAMPAIGN

THE GRADUATE COLLEGE

DECEMBER 1991

WE HEREBY RECOMMEND THAT THE THESIS BY

JOSEPH ERIC ODENCRANTZ

ENTITLED MODELING THE BIODEGRADATION KINETIC OF DISSOLVED ORGANIC CONTAMINANTS IN A HETEROGENEOUS TWO-DIMENSIONAL AQUIFER

BE ACCEPTED IN PARTIAL FULFILLMENT OF THE REQUIREMENTS FOR THE DEGREE OF DOCTOR OF PHILOSOPHY

Albert J. Valocchi  Bruce E. Rittmann
Director of Thesis Research

Neil M. Hawkins
Head of Department

Committee on Final Examination†

Albert J. Valocchi
Chairperson

Bruce E. Rittmann

Joel Massmann

† Required for doctor's degree but not for master's.

O 517

## ABSTRACT


MODELING THE BIODEGRADATION KINETICS
OF DISSOLVED ORGANIC CONTAMINANTS IN A
HETEROGENEOUS TWO-DIMENSIONAL AQUIFER

Joseph Eric Odencrantz, Ph.D.
Department of Civil Engineering
University of Illinois at Urbana-Champaign, 1992
Albert J. Valocchi and Bruce E. Rittmann, Co-Advisors

The goal of this dissertation was to develop a versatile groundwater transport model capable of incorporating various types of biodegradation kinetic sub-models, and to use the model to examine the interaction between transport and biodegradation processes in a two-dimensional heterogeneous aquifer. Operator splitting, which involves splitting the transport and kinetic equations and solving each with an appropriate method, was the numerical technique chosen because of the ease at which different biodegradation kinetic models can be changed. The differences between the Monod and biofilm kinetic models were shown to be negligible by model simulations and dimensionless analysis for realistic groundwater parameter ranges.

For dual limitation, two forms of the Monod model were examined, namely, the minimum-rate and multiplicative Monod models. Differences between the models could be quantified *apriori* by examining the kinetic parameters and substrate concentration values; maximum differences occur when one or both substrates are at subsaturation concentrations.

The effects of heterogeneity were quantified by studying transport in a two-layer stratified domain. The effects of dispersion were found to be significant when electron acceptor was injected into a background concentration of electron donor due to increased mixing of the two substrates. Biomass accumulated at the interface between the slow and

fast layers due to transverse dispersion of the electron acceptor from the fast into the slow layer.

The effect of adsorption was studied in a one–dimensional system in which electron acceptor was input into a background of electron donor. In general, increased retardation of the electron donor increased the amount of biodegradation. An initial period of rapid biological growth was followed by a pseudo–steady–state behavior. The lag time to the initial period of rapid biological growth increased with increasing retardation and decreasing velocity. Once the lag time was complete, the rate of biodegradation increased with increasing retardation factor. This increase was due mainly to the reservoir of adsorbed electron donor substrate, but was enhanced by greater overlap of the retarded donor and nonretarded acceptor fronts.

## ACKNOWLEDGMENTS

I am forever thankful to my co–advisers Professors Albert J. Valocchi and Bruce E. Rittmann for their support, suggestions, enthusiasm and friendship throughout the course of my doctoral studies. I owe most of what I have learned about research from both of them and will always be indebted to their honest and open attitudes.

There are numerous fellow graduate students of past and present as well as faculty whom I would like to mention a little about for the record and thank. Wookeun Bae for his greatly appreciated friendship and expert advice on laboratory studies. Eric Seagren for his consultation and mutual discussion on the power of units as well as his valuable suggestions toward the end of my graduate career. Phil Meyer's presence in the Hydrosystems Laboratory made life there much more enjoyable. Barth Smets for his patience and understanding when we were teaching assistants in water chemistry. Hernan Quinodoz for his sharing of valuable stochastic knowledge and for being an exceptional officemate for three years. Professors Ben Yen and W. H. C. Maxwell for their moral support. Several other fellow graduate students aided in boosting my morale and development at different times throughout my graduate career whom I would like to mention: Steve Melching, Jacques Manem, Ben Henry, Lahbib Chibani, Terrance Boyer, Amiri Abdelouahad, Rodolfo Camacho, Mark Varljen, Ted Chang and Pablo Saez.

I would like to thank Professor Edward Sudicky from the University of Waterloo for providing the principal direction computer code which was a vital part of this work. I would also like to thank Batelle Memorial Institute's Pacific Northwest Laboratory and the United States Department of Energy's Subsurface Science Program for financial assistance during my doctoral studies.

I am especially thankful for Ulrich K. Traegner's friendship, encouragement, worldly discussions, and mathematical ear, not to mention all the good times we had at Murphy's.

TABLE OF CONTENTS

## LIST OF TABLES

## LIST OF FIGURES

## LIST OF SYMBOLS

Fundamental quantities

| | |
|---|---|
| L | length |
| M | mass, in general |
| $M_s$ | mass of substrate |
| $M_x$ | mass of bacteria |
| T | time |

English symbols

| | |
|---|---|
| a | surface area per reactor volume ($L^{-1}$) |
| A | electron–acceptor concentration ($M_sL^{-3}$) |
| b | specific decay or maintenance–respiration coefficient ($T^{-1}$) |
| Co | Courant number |
| $d_p$ | particle diameter (L) |
| $D_f$ | molecular diffusion coefficient of substrate in biofilm ($L^2T^{-1}$) |
| $D_{ij}$ | hydrodynamic dispersion tensor ($L^2T^{-1}$) |
| $D_m$ | molecular diffusion coefficient of substrate in water ($L^2T^{-1}$) |
| $D_x$ | longitudinal hydrodynamic dispersion coefficient ($L^2T^{-1}$) |
| $D_z$ | transverse hydrodynamic dispersion coefficient ($L^2T^{-1}$) |
| J | substrate flux into biofilm ($M_sL^{-2}T^{-1}$) |
| $k_m$ | mass transfer coefficient ($LT^{-1}$) |
| $K_A$ | half–maximum–rate substrate concentration of the electron–acceptor ($M_sL^{-3}$) |
| $K_s$ | half–maximum–rate substrate concentration of the electron–donor ($M_sL^{-3}$) |
| L | thickness of effective diffusion layer (L) |
| $L_{fo}$ | initial biofilm thickness (L) |
| $L_x$ | grid length in the x–direction (L) |
| $L_z$ | grid length in the z–direction (L) |
| $M_S(t)$ | total mass of substrate at time t |
| $M_T$ | total active biomass concentration ($M_xL^{-3}$) |
| $M_{To}$ | initial total active biomass concentration ($M_xL^{-3}$) |
| Nc | number of microcolonies per unit aquifer volume ($L^{-3}$) |
| Pe | Peclet number |
| $q_m$ | maximum specific rate of substrate utilization ($M_sM_x^{-1}T^{-1}$) |
| $r_c$ | radius of microcolony (L) |
| $R_A$ | reaction rate of the electron–acceptor ($M_sL^{-3}$) |
| Re | Reynold's number |
| $R_{fS}$ | linear equilibrium retardation factor |
| $R_G$ | growth rate of the biomass ($M_sL^{-3}$) |

$R_M$ reaction rate of the biomass ($M_S L^{-3}$)
$R_S$ reaction rate of the electron-donor ($M_S L^{-3}$)
RSS relative sum of squares
S substrate concentration ($M_S L^{-3}$)
$S_{ai}$ analytical value of concentration ($M_S L^{-3}$)
Sc Schmidt number
$S_{in}$ substrate concentration upgradient of element ($M_S L^{-3}$)
$S_{Ni}$ numerical value of concentration ($M_S L^{-3}$)
$S_s$ substrate concentration in the biofilm ($M_S L^{-3}$)
$S^o$ influent concentration of rate-limiting substrate ($M_S L^{-3}$)
$S_s$ substrate concentration at liquid-biofilm interface ($M_S L^{-3}$)
$\Delta t$ time step of advection and dispersion (T)
$\Delta t_R$ time step of reaction (T)
t time (T)
v average linear groundwater velocity ($LT^{-1}$)
$v_i$ average linear groundwater velocity ($LT^{-1}$)
$v_x$ average linear groundwater velocity ($LT^{-1}$)
x longitudinal distance into the reactor (L)
$\Delta x$ grid-spacing in the longitudinal direction for the numerical model (L)
$\Delta z$ grid-spacing in the transverse direction for the numerical model (L)
$X_f$ biomass density in the biofilm ($M_x L^{-3}$)
Y true yield of bacterial mass per unit substrate mass utilized ($M_x M^s$)
z transverse distance (L)

Dimensionless symbols

$Da_{(mt)}$ Damkohler number for external mass transport

$$\left[ = 2L^* L_f^* D_f^* \frac{1}{S^*} \right]$$

$Da_{MAC}$ Damkohler number for loading and reaction rate

$$\left[ = \Delta x q_m M_T \frac{S_{in}}{K_S + S_{in}} / (\epsilon v S_{in}) \right]$$

$D_f^*$ dimensionless molecular diffusion coefficient of substrate in biofilm [$= D_f / D$]
$J^*$ dimensionless substrate flux into the biofilm

$$\left[ = \frac{J}{(K_s k X_f D_f)^{1/2}} \right]$$

$L^*$ dimensionless diffusive layer thickness $[= L/\tau]$

$L_f^*$ dimensionless biofilm thickness

$$\left[ = L_f \left[ \frac{kX_f}{(2K_s D_f)} \right]^{1/2} \right]$$

$Ss^*$ dimensionless substrate concentration at the liquid–biofilm interface

$$\left[ = S_s/K_s \right]$$

$S_b^*$ dimensionless bulk substrate concentration $[= S_b/K_s]$

Greek symbols

$\alpha_L$ transverse dispersivity (L)

$\alpha_T$ longitudinal dispersivity (L)

$\beta$ $S_f/S$

$\xi$ $Da_{(mt)} + \kappa - 1$

$\delta S_{max}$ maximum concentration difference ($M_s L^{-3}$)

$\epsilon$ porosity

$\gamma$ stoichiometric coefficient

$\kappa$ $K_S/S$

$\eta$ effectiveness factor, ratio of actual and fully–penetrated substrate fluxes at a given $S_s$

$\lambda$ first–order rate coefficient ($T^{-1}$)

$\rho_1$ numerical stability parameter, $Dx\Delta t/\Delta x^2$

$\rho_2$ numerical stability parameter, $Dz\Delta t/\Delta z^2$

$\tau$ standard biofilm depth dimension (L)

$\tau_c$ microcolony length (L)

$\Omega$ convergence criteria for steady–state

$\phi$ coefficient used in transient flux substrates

$$\left[ = \frac{\sqrt{2}\, L_f^*}{(1 + 2S_s^{*'})^{\frac{1}{2}}} \right]$$

$\zeta$ concentration tolerance ($M_s L^{-3}$)

# 1. INTRODUCTION

The most rapidly expanding area of groundwater research involves almost anything related to the area of *in situ* bioremediation, which is a promising technique for enhancing the clean–up rate of aquifers contaminated with organic pollutants, such as halogenated solvents, petroleum constituents, and pesticides. *In situ* projects typically involve a set of extraction and injection wells. Extraction wells are necessary for hydraulic containment of the contaminant plume and to establish a defined flow field. Injection wells allow the input of the material necessary to increase the microbiological activity in the subsurface. The injected material is a component whose normal lack of supply limits the growth of the target microorganisms and is usually an electron–acceptor, a carbon source, or a macro–nutrient. Injecting the proper amount of the limiting material creates a region of increased microbiological activity called the biologically active zone (BAZ) (Odencrantz et al., 1990).

Creation of a BAZ offers major advantages for aquifer clean–up, because microorganisms are in close proximity to all the contaminants, including those dissolved in water, those sorbed to aquifer solids, and those in a nonaqueous liquid phase. Thus, the relatively slow mechanism of flushing by water flow is replaced by degradation reaction very near the source of contaminants. As an example of the ineffectiveness of water flushing, Brown et al. (1987) found in a study of water extraction of various residually contaminated soils that 46 pore volumes of water effectively removed only 1.6% of the adsorbed gasoline fraction. Even after 500 pore volumes of flushed water, soil contamination was extremely high ($\sim$ 1400 mg gasoline/kg soil). This study demonstrates the ineffectiveness of traditional pump and treat systems and exemplifies the need to be able to attack the contaminant problem *in situ*.

Cell growth and accumulation in an aquifer depend on the availability of certain essential nutrients. These nutrients include an electron donor, an electron acceptor, and

several other elements, such as nitrogen, phosphorous, and sulfur. Usually, one of these factors is rate limiting and controls how much cell mass can be accumulated. The growth-limiting nutrient is called the limiting substrate. Which nutrient will become the limiting substrate is dictated by the particular contaminating situation. For instance, a leak or spill that creates high organic-contaminant concentrations is probably limited by the electron-acceptor or a nutrient. On the other hand, low-level contamination by a distant source can create a situation in which an organic electron donor is needed to allow significant growth.

Enhanced *in situ* bioreclamation usually involves adding the limiting substrate so that the growth limitation is eliminated and significant quantities of biomass are generated in the aquifer. Thus, a BAZ is created when the attached biomass is increased greatly from the small numbers commonly found on aquifer solids (around one million cells per gram dry aquifer solids), to a more substantial number able to utilize substrates rapidly. By creating a BAZ in contact with contaminated water and aquifer solids, an enhanced *in situ* biorelamation scheme greatly increases the rate of total aquifer clean-up.

## 1.1. Concepts of Microbial Activity in Porous Media

One of the challenges of modeling microbial activity in groundwater systems is that it can be conceptually viewed as existing in at least three different forms. The modeler is forced to choose from among these forms. The first form, called the biofilm, views the microbes as a layer-like aggregation of cells and polymers. The polymers hold the cells to each other and to a solid surface (Rittmann and McCarty, 1980) . The biofilm concept explicitly takes into account that the vast majority of bacteria in the subsurface are not suspended in the pore water, but rather are attached to sand grains and other solid surfaces that comprise an aquifer (Harvey and George, 1987). For example, Harvey et al. (1984) found that greater than 95% of the bacterial mass in a natural aquifer was attached to aquifer solids. The second form a modeler may choose is a microcolony. The microcolony is a discrete aggregation of bacteria that is attached to solid surfaces (Molz et

al., 1986). Like biofilms, microcolonies are present on the surfaces; however, unlike biofilms, microcolonies consist of cylindrical colonies of 10–100 cells that do not change in size, just number. The third form of biological activity can be termed macroscopic/Monod and is exemplified by Borden and Bedient (1986). This viewpoint assumes that the cells, although attached, are in intimate contact with the substrate concentration in the bulk pore fluid. In terms of kinetics, the macroscopic/Monod viewpoint treats all cells the same, as though they are in suspension, even though the large majority are attached and do not move with the water.

Baveye and Valocchi (1989) discussed differences among the viewpoints. They concluded that little practical difference exists between the biofilm and microcolony views when solute–transport modeling is the goal. On the other hand, their work concluded that the macroscopic approach differs significantly, because mass transport to the surface is ignored. No one has addressed the effects the differences in the above kinetic models have when modeling the groundwater transport processes involved in *in situ* bioremediation.

Besides conceptual differences in the biodegradation kinetic models, there are additional possible submodels when more than one nutrient controls the rate of growth of the bacteria. If the electron donor and acceptor control the overall biodegradation kinetics at the same time, a situation called dual–limitation, the Monod kinetic model can assume either a multiplicative or minimum–rate form. There has been no evaluation of whether the different submodels for dual limitation give significantly different results when *in situ* bioremediation is being modeled.

## 1.2 Coupling of Transport Processes and Biodegradation Kinetics in Groundwater

The coupling of transport processes, such as groundwater flow, dispersion, and sorption, with biodegradation kinetics is the key to determining the ability to form a successful BAZ in the subsurface. Heterogeneities, such as stratification, in groundwater flow systems can contribute to the success or failure of a healthy BAZ. The vast majority of knowledge available for the design of *in situ* bioremediation schemes has been obtained

from bench scale laboratory columns studies and the application of simplistic mathematical models. There have only been a few documented field scale experiments in controlled environments, and the numerous companies that market the *in situ* techniques generally keep their information privileged and confidential. Thus, we have a limited data base and must rely upon mechanistically based models to serve as tools for investigation of these complex systems. Therefore, the development of a versatile mathematical model that incorporates transport processes and alternate biodegradation models will allow the exploration of the important interacting phenomena such as stratification and sorption.

## 1.3 Scope and Organization

The goals of this dissertation are:

(a) Develop and test a computationally efficient numerical model that is flexible enough to handle alternative degradation submodels.

(b) Use the transport model to evaluate the implication of selecting alternative biodegradation submodels for simulation of *in situ* bioremediation systems; the alternative models are Monod vs. biofilm, and multiplicative vs. minimum–rate Monod for dual limitation.

(c) Use the transport model to investigate unique phenomena resulting from the coupling between transport and biodegradation in a stratified system.

(d) Use the transport model to investigate the interaction of sorption and biodegradation.

A short review of the relevant literature that pertains to the content of this thesis follows this chapter. In Chapter 3, the model choice and development are presented. In Chapter 4, the developed model is applied to quantify the differences between the Monod and biofilm biodegradation kinetics models combined with advection and dispersion for single substrate limitation. Chapter 5 quantifies the differences between the single–Monod (minimum–rate) and double–Monod (multiplicative) kinetic expressions for the case of dual substrate limitation. Chapter 6 explores the effect of hetereogeneity in the form of stratified layers on the development of biomass and the fate of organic

compounds. Chapter 7 examines the interactions between sorption and biodegradation in groundwater.

## 2. REVIEW OF BIODEGRADATION MODELING IN GROUNDWATER

An abundance of literature has been published over the last several years describing the transport of biodegradable substrates and the growth and decay of microorganisms. This is due in large part to the ever-increasing popularity of *in situ* bioremediation techniques as alternatives to pump-and-treat technology for clean-up of contaminated groundwater. Recent research demonstrating the diversity, activity, and number of microorganisms indigenous to the subsurface environment has been largely responsible for the rapid growth of designing *in situ* remediation strategies. The strategy is contingent upon stimulation of the background organisms as a result of nutrient addition. The ability to quantify some of the processes has become of paramount importance among researchers in the groundwater field.

Baveye and Valocchi (1989) categorized mathematical models that describe the simultaneous growth of bacteria and transport of biodegradable substrates in porous media. Figure 2.1 shows the three different conceptual bases for the modeling approaches: the Monod, microcolony, and biofilm models. The Monod model, termed the strictly macroscopic model by Baveye and Valocchi (1989), has been used by soil scientists over the past few decades to describe biodegradation in soil. In the Monod model, no assumption as to the distribution of the bacteria within the pore space is made, and the biodegradation kinetics are driven by the bulk concentration of the substrate. This model, proposed originally by Monod (1942), was developed to describe biodegradation kinetics of the exponential growth phase of suspended cells in various reactor types (mainly batch and chemostat). When the Monod model is incorporated as a nonlinear sink term in the solute-transport equation, it behaves as a bulk concentration-driven hyperbolic rate expression, $R_S = M_T q_m (S/(K_S + S))$, where $R_S$ is the degradation rate of S, S is the bulk pore-water concentration of the biodegradable substrate, $M_T$ is the concentration of cells, $q_m$ is the maximum specific rate of substrate utilization, and $K_S$ is

the half-velocity concentration of S. Figure 2.2 is an example of the rate variation from first- to zero-order as described by the Monod equation. The biomass growth is the degradation rate multiplied by a yield coefficient minus a cell decay term.

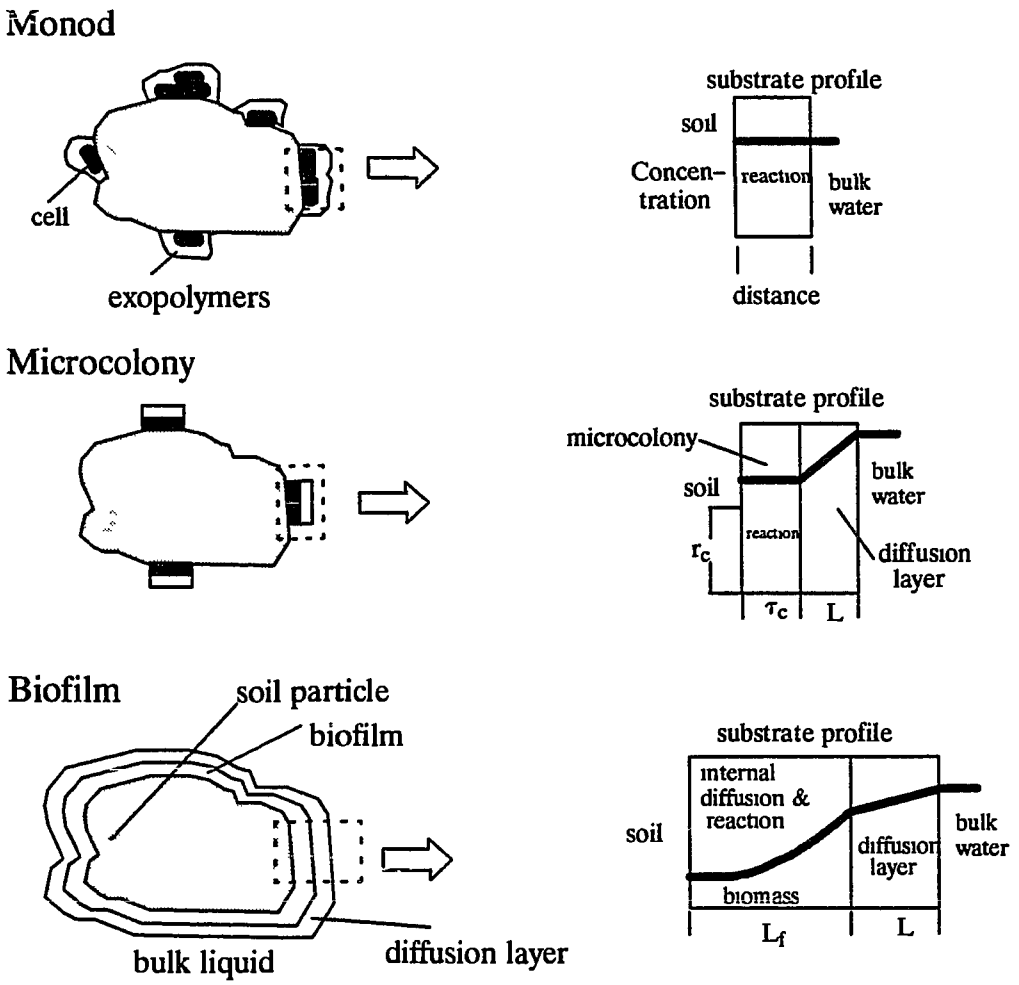


Figure 2.1. Conceptual models of biomass in aquifers. Bold lines represent the substrate concentration profile in the dashed-boxed area.

The microcolony model (Molz et al. 1986) assumes that the organisms distribute themselves on the surface of the soil particle in small, discrete colonies of 10–100 organisms. These colonies are assumed to be randomly distributed on the surface of the particle. The colonies are of fixed size, are cylindrical with a defined radius, $r_c$, and length, $\tau_c$, and the number of them per unit volume of aquifer, $N_c$, changes with time. The

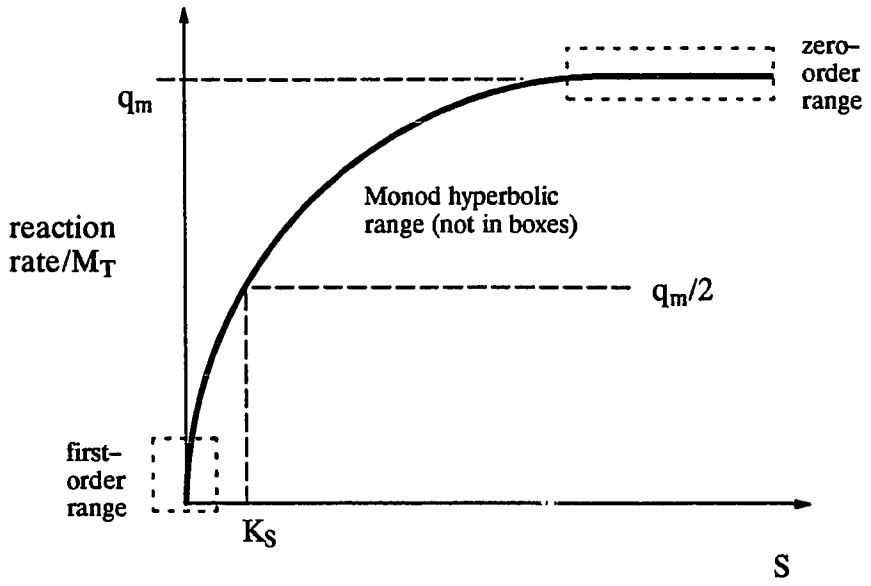


Figure 2.2. Example of Monod kinetics reaction variation.

microcolonies have a defined mass density, $\rho_c$. The substrate passes through an imaginary diffusion layer, L, accounting for external mass transport processes, before the Monod reaction kinetics describe the substrate utilization rate within the microcolony. The key assumption in the model is that the microcolony size is assumed small enough so that internal diffusion is negligible.

The biofilm model (Atkinson and How, 1971; Williamson and McCarty, 1976; Rittmann and McCarty 1980a,b; Rittmann and McCarty, 1981; Saez and Rittmann, 1988; Odencrantz et al. 1990) assumes that the bacteria and their exocellular polymers distribute themselves in the form of a film of thickness $L_f$, which uniformly covers the surface of the particles. The films are assumed to have a density $X_f$ have a constant surface area per unit volume a. The biomass concentration is defined as the product, $aX_fL_f$. This model originated in the field of environmental engineering where it is currently used to describe reaction kinetics in wastewater treatment-engineered reactors. The biofilm model include internal diffusion within the biofilm, which has been found to play a significant role in wastewater-treatment reactors. Molecular diffusion within the cell

matrix (biofilm) competes with Monod reaction and reduces the overall specific utilization rate. External mass transport is accounted for in the form of an external diffusion layer.

Several key issues isolated from the literature need to be examined in more detail. Their clarification would be a valuable contribution to the general groundwater research community. The first issue is the question of whether the different biodegradation models yield significantly different predictions when they are used to describe biodegradation kinetics in the groundwater environment. Each kinetic model increases in its complexity by accounting for additional physical properties; the key is to determine whether these processes are important under natural aquifer conditions. Furthermore, it is important to realize that the groundwater environment will be changed as a result of pumping to capture the contamination plume or to supply nutrients critical to the growth of the bacteria. These changes must also be included in any analysis designed to determine the suitability of different biodegradation models. To date, no investigation has compared the various submodels and their possible differences in describing biodegradation kinetics in groundwater. This issue is addressed in Chapter 4 by comparing the Monod and biofilm submodels, i.e. the two extremes of the three kinetic models discussed previously.

A second issue that has not been examined is the use of alternative Monod kinetic models for the commonly occurring case of dual limitation, in which there are simultaneously low concentrations of electron–donor and electron–acceptor. There are clearly two different schools of thought involved in the implementation of Monod kinetics, i.e., minimum–rate and multiplicative. Celia et al. (1989) and Frind et al. (1990) have applied the minimum–rate model to groundwater environments, while Borden and Bedient (1986a), Chiang et al. (1989), MacQuarrie et al. (1990), MacQuarrie and Sudicky (1990), Frind et al. (1989), Semprini and McCarty (1989) and Rifai and Bedient (1990) have applied the multiplicative–Monod model in groundwater environments. The practical implications of choosing either of these kinetic models to describe a realistic

remediation scenario are unclear, since this specific issue has not been previously addressed in the groundwater literature. It is obvious from the form of the equations of minimum–rate– and multiplicative–Monod kinetics that they could differ substantially depending on the kinetic parameters and concentrations of solutes involved. Chapter 5 will address the questions how much and under which conditions will they differ.

The third major issue involves the interaction of solute transport processes and coupled biodegradation processes for the case of heterogeneous aquifers. Since geologic heterogeneity plays an important role in transport and mixing processes, it should in turn play an important role in biodegradation, since biological activity depends strongly upon the presence of several dissolved constituents (e.g., electron–donor, electron–acceptor, and nutrients). Although some investigators (Molz and Widdowson, 1988; Widdowson et al., 1988; Chiang et al., 1989; Frind et al., 1989; MacQuarrie et al., 1990; MacQuarrie and Sudicky, 1990) have examined heterogeneity and its effect on biodegradation, we perform an in depth, focused analysis in Chapter 6 for the simplified case of stratified flow. Use of a stratified aquifer enables a more detailed examination of the role of heterogeneity–induced dispersion. Transverse dispersion of the electron–acceptor from a faster moving layer into a slower moving layer was addressed only fleetingly by Chiang et al. (1989), who showed that biomass accumulates between high and low conductivity layers. Widdowson et al. (1987) and Molz and Widdowson (1988) stress the importance of varying hydraulic conductivity and speculate that these varying layers of hydraulic conductivity play an important role in biodegradation processes.

The general effects of the interaction of biodegradation kinetics and sorption of contaminants should be examined in greater detail, because the studies to date (Borden and Bedient, 1986a; Chiang et al., 1989; and MacQuarrie et al., 1990) have not been comprehensive and have differing results. In Chapter 7, we focus upon the effects of sorption.

Examination of the three issues described above requires an efficient and flexible two–dimensional transport model. Development and validation of such a model is the subject of the next chapter.

# 3. DEVELOPMENT AND VALIDATION OF THE TWO-DIMENSIONAL SOLUTE TRANSPORT MODEL

## 3.1 Goal of the Model

Deriving a two-dimensional model capable of describing simultaneous advection, dispersion, biodegradation, and linear equilibrium adsorption is the goal of model development for this thesis. The unique feature that makes this modeling approach challenging occurs when the biodegradation models included as reaction sink terms make the transport equation severely nonlinear. In general, nonlinearity results because the biodegradation reaction rate is a nonlinear function of the concentration of one or more of the dissolved substrates undergoing advection and dispersion. Although several researchers have developed contaminant transport models which include a minimum-rate Monod reaction (Celia et al. 1989), a multiplicative Monod reaction (Borden and Bedient, 1988), and a biofilm reaction (Odencrantz et al. 1990), none of the contaminant transport models can interchange all three of the biodegradation reaction models.

## 3.2 Operator Splitting

Although the governing equations of two-dimensional solute transport combined with the nonlinear biodegradation terms can be solved in many ways, an approach to the solution of nonlinear partial differential equations which has recently regained popularity, termed operator splitting, was chosen for its many advantages over other numerical approaches. In particular, operator splitting is attractive because of the ease with which different biodegradation kinetics can be interchanged or added. Operator splitting involves solving the advection and dispersion terms separately from the reaction terms. Each solution is performed sequentially, using a numerical technique particularly suited for the operator (Wheeler, 1988). This 'decoupling' is a computationally efficient way of dealing with complex reactions, especially in the common case when the reaction

time scale is much smaller than the advective/dispersive time scale. Moreover, operator splitting leads to a modular code structure, which makes it relatively easy to implement alternative reaction submodels.

The best way to demonstrate operator splitting is to provide an example. The problem of interest in this research is the coupling of advection, dispersion, and biological reaction simultaneously for the electron donor, electron acceptor, and total biomass. In this case, the coupled governing mass balance equations are:

$$\frac{\partial S}{\partial t} = -v_i \frac{\partial S}{\partial x_i} + \frac{\partial}{\partial x_i} D_{ij} \frac{\partial S}{\partial x_j} - R_S \qquad ; i = 1,2 \tag{3.1}$$

$$\frac{\partial A}{\partial t} = -v_i \frac{\partial A}{\partial x} + \frac{\partial}{\partial x_i} D_{ij} \frac{\partial A}{\partial x_j} - R_A \qquad ; i = 1,2 \tag{3.2}$$

$$\frac{\partial M_T}{\partial t} = R_M \tag{3.3}$$

where S is the aqueous-phase concentration of electron donor, A is the aqueous-phase concentration of electron acceptor, $M_T$ is the total biomass concentration, $v_i$ is the average linear velocity, $D_{ij}$ is the hydrodynamic dispersion tensor, $R_S$ and $R_A$ are biodegradation kinetic loss terms for S and A, respectively, and $R_M$ is the net growth are of the biomass. The coupling of equations (3.1)–(3.3) arises because $R_S$, $R_A$, and $R_M$ are each functions of S, A, and $M_T$. The loss terms $R_S$ and $R_A$ could include sorption processes. When operator splitting is applied, equations (3.1) and (3.2) are broken up into two parts, one that is purely nonreactive, and other purely reactive:

$$\frac{\partial S}{\partial t} = -v_i \frac{\partial S}{\partial x_i} + \frac{\partial}{\partial x_i} D_{ij} \frac{\partial S}{\partial x_j} \tag{3.4}$$

$$\frac{\partial S}{\partial t} = -R_S \tag{3.5}$$

$$\frac{\partial A}{\partial t} = -v_i \frac{\partial A}{\partial x} + \frac{\partial}{\partial x_i} D_{ij} \frac{\partial A}{\partial x_j} - R_A \tag{3.6}$$

$$\frac{\partial A}{\partial t} = -R_A \tag{3.7}$$

In brief, the nonreactive solute transport equations (3.4) and (3.6) are solved over one time interval using an appropriate numerical method well suited for the advection–dispersion equation, and equations (3.3), (3.5) and (3.7) are solved using an ordinary differential equation solution technique. Further details about operator splitting are provided by Wheeler and Dawson (1987). Also, Rifai (1990) reports that a group at Rice University has implemented an operator splitting technique as the basis of their BIOPLUME II model.

The general solution procedure over one complete time step is summarized in Figure 3.1.

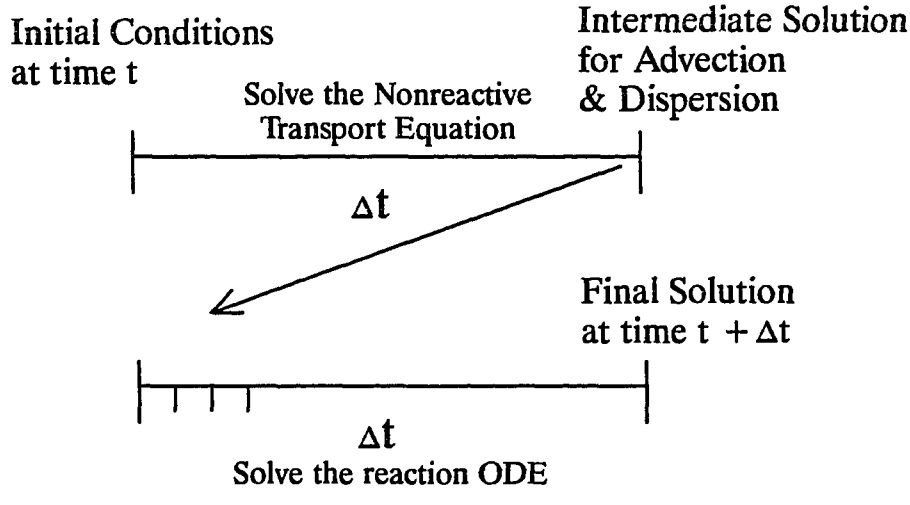


Figure 3.1. Summary of one complete operator split cycle for $\Delta t$.

This cycle is repeated n time steps until the final time of interest is reached. It is also possible to use a smaller time step for the second stage if necessary; this would be required if the reaction time scale were much less than the advective/dispersive time scale.

### 3.2.1 The Principal Direction Finite Element Method

The method of solving the two–dimensional, nonreactive, advection–dispersion equation is considered in this section. Due to extremely fine grid–spacing requirements and time discretization, standard finite–differences or finite elements are probably not

the most efficient approaches for solution. The Principal–Direction Finite Element Method (PD) was chosen because of its proven accuracy, stability, and efficiency for this type of problem (Frind, 1982; Frind and Germain, 1986; and MacQuarrie et al. 1990).

PD is more accurate and efficient than the conventional Finite Element Method (FEM). PD differs from the conventional FEM in that it is formulated in terms of the principal directions of transport and is structured as an alternating direction solution scheme (Frind, 1982). The principal directions of transport are defined by a natural coordinate system, which consists of the intersection of the streamlines and equipotentials of the flow field. The numerical advantage of this formulation is that the advective transport component is restricted to only one direction, which allows the grid Peclet and Courant criteria to be rigorously applied in the advective direction (MacQuarrie, et al., 1990). The implication of such a numerical framework is that the numerical solution in the transverse direction is free of classical numerical dispersion and oscillation, because only the pure dispersion equation needs to be solved in that direction. Also, because PD uses a natural coordinate system, the cross terms of the hydrodynamic dispersion coefficient vanish. Thus, the two components of dispersion in the longitudinal and transverse directions are written for the case of uniform flow in the x–direction as

$$D_x = a_L v_x + D_m \tag{3.8}$$

$$D_z = a_T v_x + D_m \tag{3.9}$$

where $\alpha_L$ is the longitudinal dispersivity, $\alpha_T$ is the transverse dispersivity, and $D_m$ is the molecular diffusion coefficient of the substrate in a porous medium. Efficiency is achieved by decoupling the two–dimensional transport equation into a set of one–dimensional equations, thus yielding tridiagonal coefficient matrices. This is accomplished by a standard alternating direction time splitting. The matrices are solved using the well–known Thomas algorithm. Further details concerning the formulation of the matrix equations and the alternating direction sweeping are given in Frind (1982).

The prime concern when applying PD to a defined transport problem is that the well-known Peclet and Courant criteria, along the advective direction, need to be satisfied to insure that numerical dispersion and oscillation are controlled. The Peclet number (Pe) provides a criterion to control oscillations due to spatial discretization (Daus and Frind, 1985) and can be physically interpreted as the ratio of advective to dispersive transport components. A Courant number violation is known to result in smearing of the front; the Courant number (Co) can be physically interpreted as the ratio of the advective distance travelled in one time step to the nodal spacing. The Peclet and Courant criteria (Frind, 1982; Daus, et al., 1985; Frind and Germain, 1986; MacQuarrie, et al., 1990) are

$$Pe \leq 2 \quad \text{where} \quad Pe = \frac{v_x \Delta x}{D_x} \tag{3.10}$$

$$Co \leq 1 \quad \text{where} \quad Co = \frac{v_x' \Delta t}{\Delta x} \tag{3.11}$$

where Pe is the Peclet number, Co is the Courant number, $v_x'$ is the retarded velocity in the case of linear equilibrium adsorption, and $\Delta x$ is the nodal spacing in the longitudinal direction, i.e., the direction of flow. MacQuarrie et al. (1990) suggest that the nodal spacing in the transverse direction perpendicular to the flow be chosen such that the transverse concentration profile is adequately represented by linear basis functions. Frind (1982) showed that the accuracy in the transverse direction is a function of a stability parameter $\rho_2$, where $\rho_2 = D_z \Delta t / \Delta z^2$. Daus and Frind (1985) refer to $\rho_2$ as a transverse spacing parameter and suggest that the optimal accuracy in the transverse direction will occur when the aspect ratio, $\rho_1/\rho_2$, is equal to unity. Frind (1982) found that for Co = 1 and Pe = 2 ($\rho_1 = 0.5$, $\rho_1 = Co/Pe$), values of $\rho_2 = 0.04$ ($\rho_1/\rho_2 = 12.5$) and 0.01 ($\rho_1/\rho_2 = 50.0$) gave the same accuracy as an analytical solution for a transverse profile 8 m from the source. For a profile 40m from the source, $\rho_2 = 0.04$ gave only slightly better results than $\rho_2 = 0.01$. His conclusion was that the sensitivity to $\rho_2$ is low. One important finding discussed in the paper was the fact that the discretization over the source function is a possible factor governing accuracy in the transverse direction. This finding was verified to be the primary

concern when choosing the transverse grid spacing in subsequent papers by Daus and Frind (1985) and Frind and Germain (1986). The bottom line on the selection of $\Delta z$ is to keep $\rho_1/\rho_2$ less than approximately 13.

Another interesting finding related to Peclet and Courant criteria was reported by Daus et al. (1985). They found that at late times into FEM method simulations with numerical dispersion criteria based upon Peclet and Courant criteria, the time-stepping could be relaxed, while the error remained at a constant level. The concept of an advective Peclet number was introduced (defined as the product of the Peclet and Courant numbers) to provide an upper ceiling on the time-step increase. Although this may be an interesting area to explore, there will be no consideration of increased time-stepping at large times in this thesis.

A number of different boundary conditions are implemented into the PD formulation. Dirichlet (first-type) and Cauchy (third-type) can be imposed at the source and domain boundaries. A free-exit boundary is imposed along the exit face and allows mass to advect and disperse freely without specifying an artificial boundary condition. A numerical solution incorporating a free-exit boundary behaves like an infinite-domain solution for advective dominated flow (Frind, 1988).

In summary, The PDFEM is used to solve the nonreactive transport equation in the first stage of the operator splitting technique; the time step ($\Delta t$) is chosen using the standard Peclet and Courant criteria for accurate, oscillation free numerical solution (see equations 3.10 and 3.11). Note that there are two, uncoupled transport equations solved in this stage, namely equation (3.4) for S and (3.6) for A; each equation may have different parameter values and different initial and boundary conditions.

### 3.2.2 Solution of the System of Differential Equations

The second stage of operator splitting entails solution of the reaction equations (3.3), (3.5) and (3.7). For convenience these are reported below

The solution for the ODEs (equations (3.12)-(3.14)) can be found using the Runge-Kutta

$$\frac{dS}{dt} = -R_S \tag{3.12}$$

$$\frac{dA}{dt} = -R_A \tag{3.13}$$

$$\frac{dM_T}{dt} = R_M \tag{3.14}$$

method, which is a commonly used numerical technique for solving systems of nonlinear ordinary differential equations (Dennis and Schnabel, 1983). Wheeler (1988) and Chiang et al. (1989) used a second-order Runge-Kutta method to solve the system of reaction equations with reaction time steps 100-1000 smaller than the advection-dispersion time step (see Figure 3.1). Unfortunately, no results were presented to illustrate how sensitive the solution of the ODEs were to the number of times Runge-Kutta was applied in one time step (henceforth referred to as the number of Runge-Kutta steps). A fourth-order Runge-Kutta integration was selected to solve the system of equations here, because it is fifth-order accurate in time, as opposed to the second-order scheme used by Wheeler (1988) and Chiang et al. (1989), which is only third order accurate in time. Because of the severe nonlinearity of these equations, the Runge-Kutta method is employed numerous times (ranging from 5-100 times) in one $\Delta t$ of advection/dispersion.

An example of the application of the fourth-order Runge-Kutta integration of equations (3.12) and (3.13) over one time step of reaction is done with the following procedure (Lee, 1968):

$S^{t+\Delta tR} = S^t + 1/6\,(m_1 + 2m_2 + 2m_3 + m_4)$

$A^{t+\Delta tR} = A^t + 1/6\,(l_1 + 2l_2 + 2l_3 + l_4)$

where

$m_1 = R_S\,(S^t, A^t)\Delta t_R$

$m_2 = R_S\,(S^t + 1/2\,m_1,\ A^t + 1/2\,l_1)\Delta t_R$

$m_3 = R_S\,(S^t + 1/2\,m_2,\ A^t + 1/2\,l_2)\Delta t_R$

$m_4 = R_S\,(S^t + m_3,\ A^t + l_3)\Delta t_R$

and

$$l_1 = R_A (S^t, A^t)\Delta t_R$$

$$l_2 = R_A (S^t + 1/2\, m_1, A^t + 1/2\, l_1)\Delta t_R$$

$$l_3 = R_A (S^t + 1/2\, m_2, A^t + 1/2\, l_2)\Delta t_R$$

$$l_4 = R_A (S^t + m_3, A^t + l_3)\Delta t_R$$

where $S^t$ and $A^t$ are the initial conditions for the integration, $S^{t+\Delta tR}$ and $A^{t+\Delta tR}$ are the integrated concentration values at $t+\Delta t_R$, and $\Delta t_R$ is the time step of reaction and is defined as $\Delta t$/the number of Runge–Kutta steps. In the simplified example above, the biomass concentration $M_T$ is assumed constant and thus equation (3.14) is not integrated. $S^t$ and $A^t$ represent intermediate concentrations from the advection and dispersion step. In the code, of course, we solve equations (3.12)–(3.14) simultaneously, so the biomass is coupled with the electron donor and electron acceptor reaction equations. The above procedure is applied for the chosen number of Runge–Kutta steps.

The efficiency of operator splitting for this problem is possible because the nonlinearity and coupling are restricted to a system of ODEs instead of PDEs. The ease with which various types of biodegradations kinetics or adsorption kinetics can be added is illustrated by equations (3.12)–(3.14). The right hand side is completely general and could be a simple Monod expression, or a more complex nonequilibrium adsorption kinetic model. This flexibility is important to attain the goals of this thesis.

A potential criticism of using Runge–Kutta for the solution of the system of reaction equations is that the same amount of work is involved at every node, even though nothing is happening in places in the domain where the plume has not reached. One possible approach to overcoming this possible inefficiency is to stop applying the Runge–Kutta integration when the substrate or biomass concentration is zero. Another interesting concept is to provide analytical solutions for simpler kinetics, i.e. zero– or first–order in S. Neither of these ideas was implemented in this thesis.

## 3.3. Implementation of Different Biodegradation Models

There are numerous different biodegradation kinetic models that could be incorporated into the operator splitting model. Several of the most well known biodegradation models were discussed in some detail in Chapter 2. One of the goals of this dissertation is to compare alternative biodegradation kinetic models when they are implemented into a solute-transport algorithm that describe biodegradation processes in groundwater. Two models will be examined in detail, namely, the Monod and biofilm models. A brief description of the incorporation of each model into the operator splitting algorithm is outlined in the following paragraphs.

### 3.3.1 Implementation of Monod Kinetic Models

As an example, we can assume that the biological reaction is described by the multiplicative Monod equation. The form of the reaction terms are shown below

$$R_S = M_T q_m \left(\frac{S}{K_s + S}\right)\left(\frac{A}{K_A + A}\right) \tag{3.15}$$

$$R_A = \gamma M_T q_m \left(\frac{S}{K_s + S}\right)\left(\frac{A}{K_A + A}\right) = \gamma R_S \tag{3.16}$$

$$R_M = Y M_T q_m \left(\frac{S}{K_s + S}\right)\left(\frac{A}{K_A + A}\right) - bM_T + bM_{To} \tag{3.17}$$

where $M_T$ is the total microbial mass concentration, $q_m$ is the maximum rate of substrate utilization, $K_s$ and $K_A$ are the half velocity concentrations for the electron donor and acceptor, Y is the cell yield coefficient, S and A are the aqueous-phase concentrations of the electron donor and acceptor, $\gamma$ is the stoichiometric coefficient, b is the cell decay coefficient, and $M_{To}$ is the initial biomass concentration. The term $bM_{To}$ was included by Chiang et al. (1989) to avoid excessive cell decay of the background cell concentration for continuous source problems. The addition of the term $bM_{To}$ implies that the background bacteria remain the same unless the new growth occurs as the result of substrate addition. Basically, the background bacteria are assumed to remain at constant concentration because they are utilizing exocelluar substrates that occur naturally.

There are several variations of Monod kinetics, that basically involve small modifications for the $R_S$, $R_A$, and $R_M$ expressions given in (3.15)-(3.17). These variations could be the case of minimum-rate Monod kinetics, where either the electron donor or electron acceptor controls the kinetics at every time and at every location throughout the simulation, or minimum-rate kinetics, where either the electron donor or electron acceptor limits the kinetics depending on the substrate concentration and the value of their half-velocity kinetic constants. These three Monod kinetic options, multiplicative Monod, single-Monod, and minimum-rate Monod, are available for the dual-substrate transport coupled with biomass growth. The exact form of the kinetic equations for each of these cases is deferred until Chapter 5, where they are examined in great detail and their differences are assessed by implementing them into our numerical framework.

### 3.3.2 Implementation of Biofilm Kinetics

In addition to the Monod submodels described above, the more mechanistically based biofilm model was implemented. The biofilm model is presented for the case of a single rate-limiting electron donor. As described in Chapter 2, the biofilm model assumes that bacteria uniformly cover the solid grains as a film of thickness $L_f$ and density $X_f$. Therefore, the biomass concentration, $M_T$, in this case equals $aX_fL_f$, where a is the specific surface area of the solid grains. The reaction equations for the electron donor, acceptor and biomass take the form:

$$R_s = aJ(S, L_f) \tag{3.18}$$

$$R_A = \gamma aJ(S, L_f) = \gamma R_S \tag{3.19}$$

$$\frac{\partial(aX_fL_f)}{\partial t} = R_M \tag{3.20}$$

$$\text{where} \quad R_M = Y\ J(S, L_f) - bX_fL_f + bX_fL_{f0}$$

where $J(S, L_f)$ = the flux of substrate into the biofilm, $\gamma$ = stoichiometric coefficient, $L_f$ = biofilm thickness, Y = yield coefficient, b = total decay, $X_f$ = biofilm density, and $L_{f0}$ = the initial background biofilm thickness. The above equation assumes the organic

compound is rate-limiting throughout the whole simulation. The flux of substrate into the biofilm is determined using the submodel of Rittmann and McCarty (1981). This submodel is highly nonlinear and involves an iterative Newton-Raphson procedure.

The pseudo-analytical solution of Rittmann and McCarty (1981), which was built upon the work of Atkinson and How (1974), is utilized to estimate the flux of rate-limiting substrate into the biofilm. To start the simulation an initial biofilm thickness must be calculated, but the distribution of biomass will change in accordance to the new growth of the system governed by equation (3.20). The details of the pseudo-analytical solution are presented in the original paper; however a short summary of the procedure can be found in the Appendix at the end of the thesis.

## 3.4 Comparison Between Numerical and Analytical Solution

Several representative numerical problems were developed for the numerical testing of the operator splitting model. These numerical tests are outlined in the three following sections.

### 3.4.1 Operator Splitting Compared to Analytical Solution in One-Dimension

The operator splitting model was compared to an exact analytical solution of a solute undergoing first-order decay. Only the single transport equation (3.1) is considered with the multiplicative Monod equation (3.15) reduces to this form where $\lambda = M_T q_m / K_S$ if $K_s >> S$, $K_A << A$ and $M_T$ is constant, thus $R_S = \lambda S$. Figure 3.2 shows the boundary conditions and transport parameters used for the comparison. The molecular diffusion coefficient was assumed to be zero. To demonstrate the performance of operator splitting, a wide range of first-order rate constants varying over three orders of magnitude was chosen. The rate constants were chosen on the basis of several numerical tests. The lowest value gave a longitudinal profile close to the nonreactive curve, and the highest value represents a large amount of decay. The analytical solution was obtained from Edward Sudicky from the University of Waterloo and is called PATCH3D.

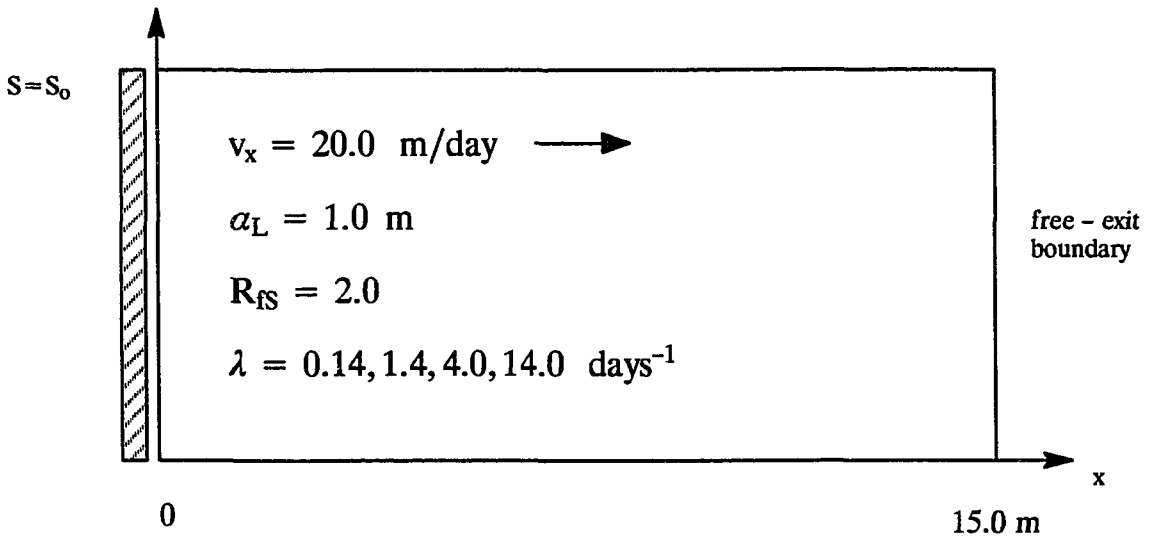


Figure 3.2 Boundary conditions and transport parameters for numerical and analytical comparison in one-dimension with several first-order kinetic constants.

In the example problem in Figure 3.2 also includes linear equilibrium adsorption of S with a linear equilibrium retardation factor $R_{fS}$. For this case, equation (3.1) is modified slightly and takes the form

$$\frac{\partial S}{\partial t} = -v_i' \frac{\partial S}{\partial x} + \frac{\partial}{\partial x_i} D_{ij}' \frac{\partial S}{\partial x_j} - R_S' \qquad (3.21)$$

where

$$R_S' = \left(\frac{M_T q_m'}{K_s}\right) S = \frac{\lambda S}{R_{fS}}$$

and $D_{ij}' = D_{ij}/R_{fS}$, and $q_m' = q_m/R_{fS}$.

Figure 3.3 compares longitudinal profiles from the numerical and analytical solutions for the different first-order rate constants at time 0.50 days. The PD nodal spacing was 0.5 m, and the time step was 0.025 days, which resulted in a Peclet number of 0.50, a Courant number of 0.50, and a $\rho_1$ value of 1.0. Ten Runge-Kutta steps were used to solve the reaction term of equation (3.1) with $R_s = \lambda S$. In this case, an analytical solution could have been used to solve $dS/dt = -\lambda S$; however, Runge-Kutta was chosen, since it will be the solution technique used in the general two-dimensional case with nonlinear reaction. The agreement between the two solutions is excellent and verifies that operator splitting

accurately simulates the processes of advection, dispersion, retardation, and first-order decay, even with large variations in the decay constant.

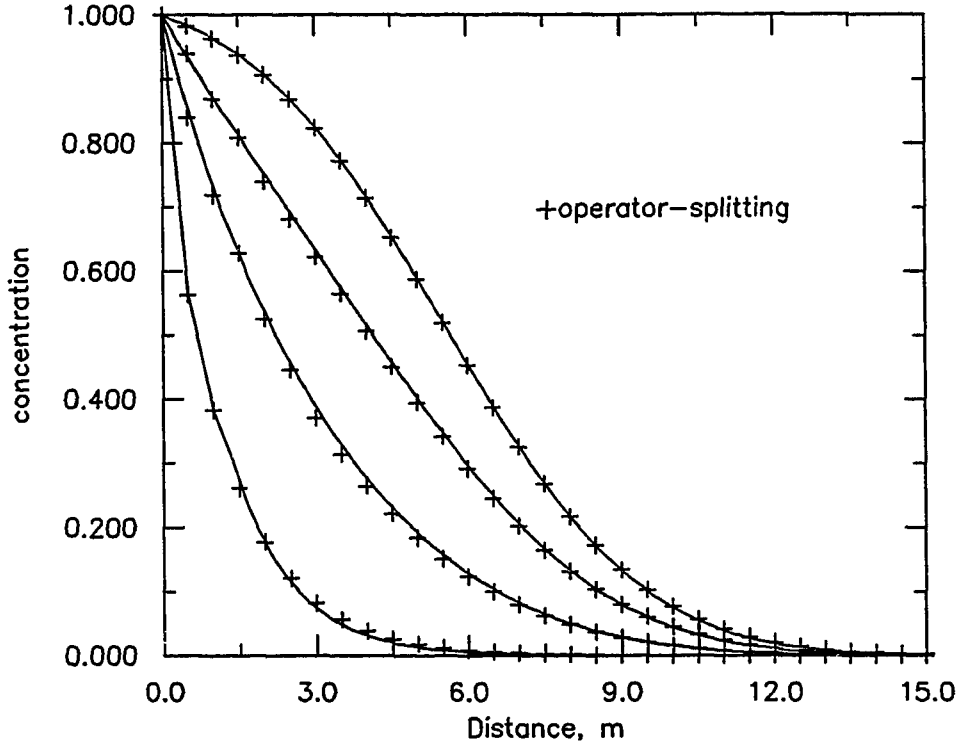


Figure 3.3 Comparison of analytical (solid lines) and numerical (symbols) solutions in one-dimension at time 0.50 days. The first-order rate constants (days$^{-1}$) for each curve (going from left to right) are; 14.0, 4.0, 1.4, and 0.14.

### 3.4.2 Operator Splitting Compared to Analytical Solution in Two Dimensions

The comparison in two dimensions was performed with one first-order loss constant, and longitudinal and transverse profiles at selected times were compared. Figure 3.4 shows the location of the continuous source (first-type boundary), boundary conditions, and transport parameters used for the two-dimensional comparison. The molecular diffusion coefficient was assumed to be zero. A realistic ratio of longitudinal to transverse dispersivity (120) was used. Once again, only the transport equation for the organic (S) with first-order loss needed to be solved (i.e., the same as for the one-dimensional comparison). The two-dimensional non-reactive solute transport equation was solved

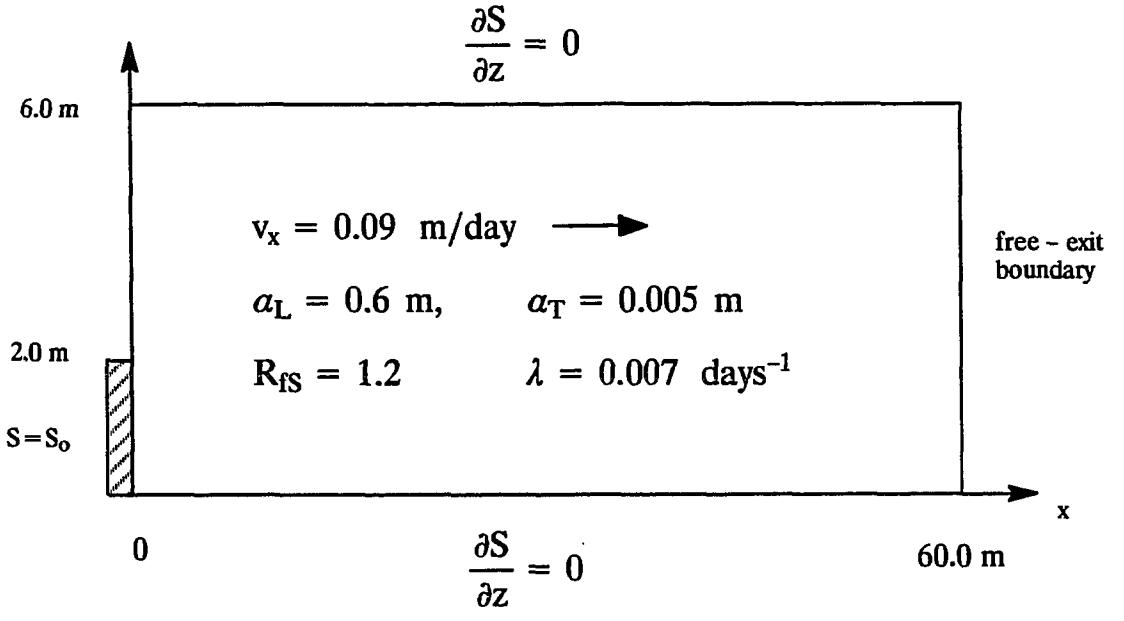


Figure 3.4. Boundary and transport parameters for numerical and analytic comparison in two-dimensions with one first-order kinetic constant.

using PD, and then the first-order biological decay equation was solved using the Runge-Kutta method; ten Runge-Kutta steps were used. The PD longitudinal and transverse grid spacing were 0.50 m and 0.125 m, respectively, and a time step of 10 days was used. These parameters resulted in a Peclet number of 0.83, a Courant number of 1.5, and values of $\rho_1$ and $\rho_2$ of 0.55 and 0.24, respectively, which gives a value of $\rho_1/\rho_2$ equal to 2.30.

Figure 3.5 compares longitudinal profiles for the analytical (PATCH3D) and numerical solutions at four selected times. Once again, the operator splitting solution compares very well to the analytical solution in all cases. Figure 3.6 compares the transverse profiles of the numerical and analytical solutions at three selected times. The results are satisfactory and show that operator splitting is able to resolve the reaction terms accurately in the transverse direction.

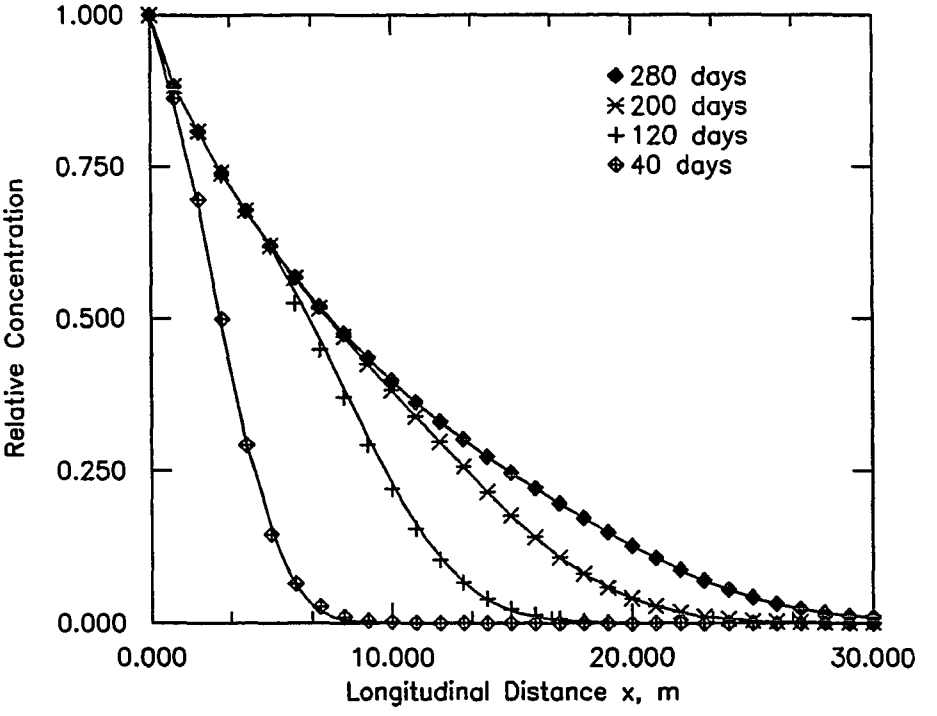


Figure 3.5. Comparison of the analytical (lines) and numerical (symbols) longitudinal profiles at z = 0 m for the two-dimensional case.

### 3.4.3 General Performance of Operator Splitting for Nonlinear Reaction

We must solve coupled nonlinear reactions for which no analytical solutions are available; nonetheless, thus we want to be able to test the code's accuracy. One way of doing this is to compare the developed code to a different numerical code. To determine the performance of operator splitting, several criteria need to be considered. Recall that the advection-dispersion time step required to solve equation (3.4) is divided into many smaller time steps to solve for the reaction equation; a fourth-order Runge-Kutta method is used to solve equation (3.5). The basis of comparison for the operator splitting model is the model of MacQuarrie et al. (1990). MacQuarrie et al. (1990) applied PD to the two-dimensional solute-transport equation with a dual-Monod expression as the biodegradation utilization rate. The nonlinearity of the transport equations is handled by employing an iterative scheme that converges at a linear rate. Convergence is achieved

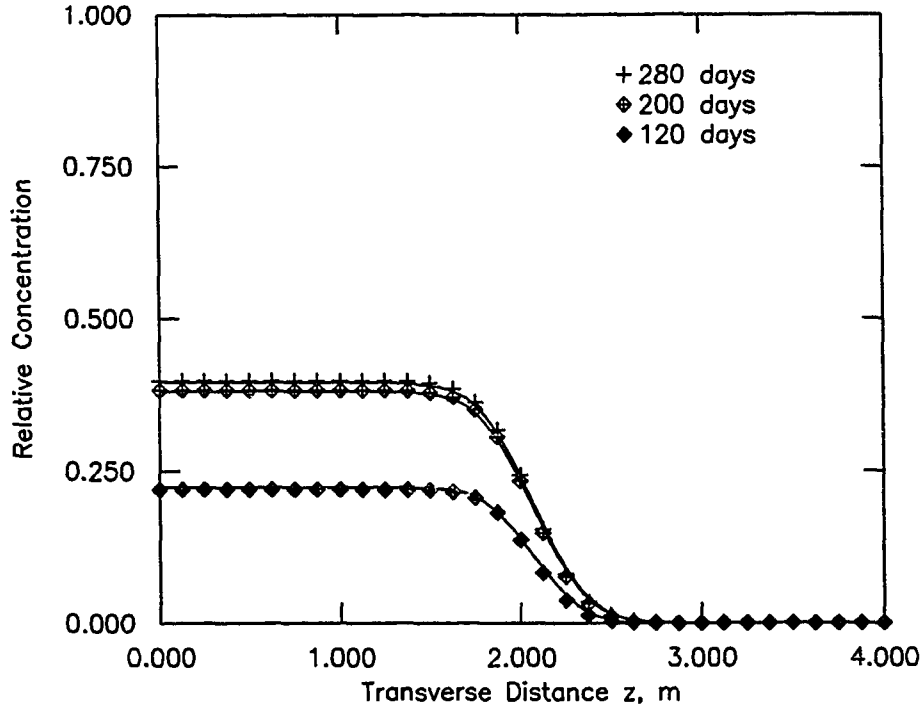


Figure 3.6 Comparison of analytical (lines) and numerical (symbols) for the transverse profiles at x = 10 m for the two-dimensional case.

when the change in organic concentration at every node is less than a specified tolerance. The tolerance is actually a concentration value in micrograms per liter, defined as $\delta S_{max} < \eta$, where $\delta S_{max} = \max |(S_j)_{i+1} - (S_j)_i|$, $\zeta$ is the concentration tolerance, j = node, and i = iteration level. This code was obtained from Edward Sudicky from the University of Waterloo (one of the coauthors of MacQuarrie et al. 1990) and used to test the results of operator splitting.

The first criterion, efficiency, was examined by comparing the operator splitting execution time as a function of the number of Runge–Kutta steps to the execution time for the standard PD . The second criteria considered was accuracy, and the operator splitting technique was again compared to PD. Each of the criteria for performance is discussed in detail in the next few paragraphs.

The standard PD execution time refers to execution time of the model of MacQuarrie et al. (1990), who applied PD to solve equations (3.1) to (3.3) with multiplicative Monod

reaction kinetics (3.15–3.17). The timings of OS compared to the standard PD are the only way to get an idea of the efficiency between the two techniques when all three governing equations are solved simultaneously. The timings were done on an Apollo workstation Series DN–3500. The OS technique is noniterative, making the execution time a linear function of the number of Runge–Kutta steps taken. The standard PD code involves iteration, and the execution time is a function of the desired error tolerance. To demonstrate the efficiency of the operator splitting technique, timings were done with an example problem that involved a continuous partial line source along the inflow boundary of a domain with one–dimensional flow identical to Figure 3.4. The problem consisted of 231 computational nodes, and the simulation was carried out for 10 days with a time step of 0.5 day and with grid Courant and Peclet numbers of 0.5 and 1.0, respectively. Figure 3.7 shows the execution time in cpu seconds for operator splitting and the standard PD code as a function of the number of Runge–Kutta steps and tolerances, respectively. The standard PD at the highest tolerance and the noniterative solution of operator splitting with no Runge–Kutta steps took nearly the same time. This is essentially the case of solving three nonreactive transport equations (for S, A, and $M_T$) with PD.

The next performance criterion is accuracy. Accuracy is a very difficult property to measure, since no analytical solutions are available for the three coupled, nonlinear transport equations. The only approach that can be taken is to give the standard PD code a very strict tolerance and use the solution as a basis for comparison. Another alternative would be to use only one noncoupled solute transport equation with either first– or zero–order kinetics, for which an analytical solution is available.

Two problems arise when considering the use of the standard PD code as a basis for comparison. The first concerns which tolerance is needed to approximate the true solution, and the second is a basis to compare the results of the operator splitting technique. To best address these issues, the second problem should be considered first. A standard measure of error is necessary to compare the solution at each of the 231 nodes in

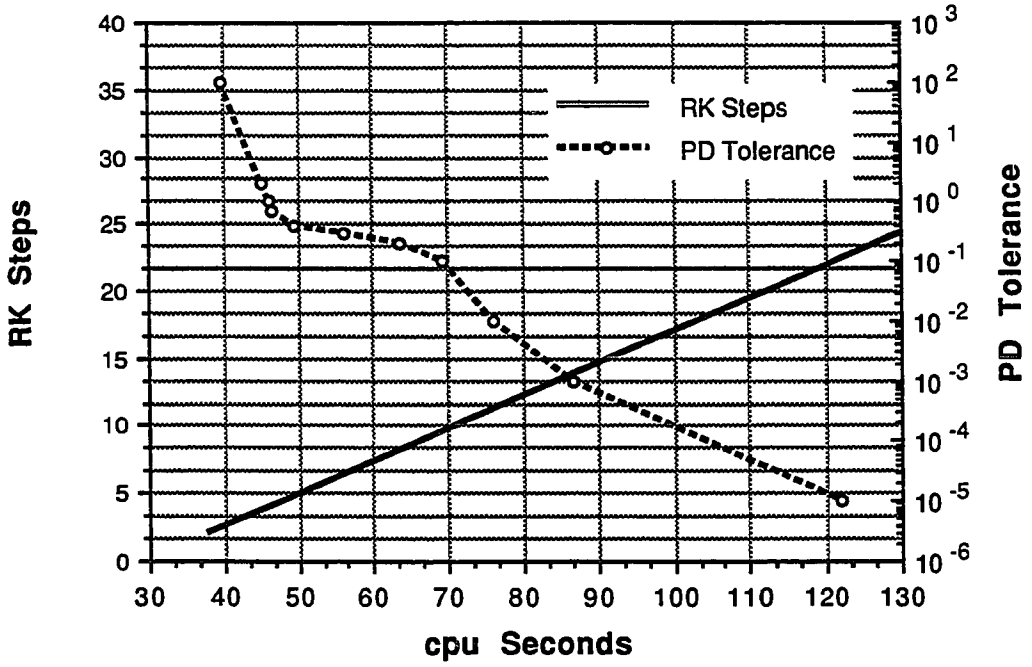


Figure 3.7. Comparison of execution times for the PD and OS code solutions of the example problem.

the model problem. The relative sum of the squares is a standard means by which an analytical and numerical solution can be compared and will serve as an indicator of the goodness of numerical solution, i.e., operator splitting in this case. The form of the equation that yields the total relative sum of the squares for the computational grid at a particular time in the simulation is

$$RSS = \sum_{i=1}^{N} \left( \frac{S_{ai} - S_{Ni}}{S_{ai}} \right)^2 \qquad (3.22)$$

where $S_{ai}$ is the value of the "analytical" solution at grid point i, $S_{Ni}$ is the value of the numerical solution at grid point i, and N is the total number of grid points in the computational domain. The relative sum as squares was chosen as opposed to the absolute sum of squares to give each of the concentration values the same weight.

The next problem to consider is what tolerance should be used for the standard PD to best approximate the true (i.e., "analytical") solution. The approach was to choose a very small tolerance (eight orders of magnitude smaller than the injection concentration, e.g., $10^{-5}$ μg/L for the organic compound) and examine the relative sum of squares (RSS) of larger tolerances compared to the solution at the very small tolerance. As the tolerances decreased from $10^{2}$ to $10^{-5}$, so did the RSS. With tolerances of $10^{-5}$ and $10^{-6}$, the RSS was approximately $10^{-7}$, an extremely small value. Therefore, the solution of the standard PD code at the small tolerance level of $10^{-5}$ was used as a basis for comparison.

Figure 3.8 is a plot of the number of Runge–Kutta steps used in the operator splitting routine versus the RSS, defined by (3.22), where $S_a$ represents the standard PD solution at the smallest error tolerance. All results are for our model problem at 10 days into the simulation. It is quite evident that the RSS decreases dramatically as the number of Runge–Kutta steps increases and converges to an extremely small RSS. Ideally the RSS should converge to zero if operator splitting was to converge to the result obtained from the standard PD. The error, although extremely small, is most probably attributable to the standard PD not being the exact solution of the system of transport equation.

Preliminary tests were performed to determine the possibility of using an alternative differential equation solution technique with adaptive step–size control. The Adam's method was considered, in which the solution is obtained by replacing the derivative with a polynomial interpolated to compute derivative values followed by integrating the polynomial (Shampine and Gordon, 1975). One of the many available canned subroutines using Adam's method was selected. The subroutine calls for relative and absolute error tolerances to define the tolerance of the solution algorithm. The method was programmed to solve the reaction equations and then combined with PD to complete the operator–split solution. Some encouraging results were found at first, in one case, the technique reached the same accuracy as the fourth–order Runge–Kutta for a given number of Runge–Kutta steps in 47 seconds as opposed to 110 seconds. It was discovered

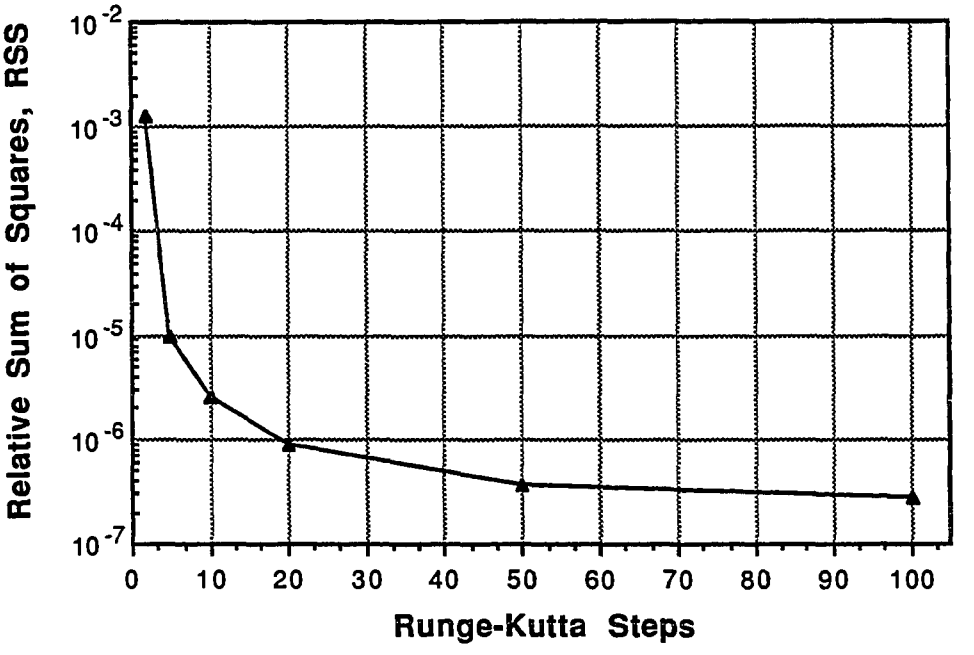


Figure 3.8. The relative sum of squares defined by equation (3.22) versus the number of Runge–Kutta steps used in the OS solution of the example problem.

later that the additional speed was attributed to the step–size control far from the source. Far from the source, the Adams method used only one step which the substrate concentration was zero, while the Runge–Kutta still computed the same number of steps at every node in the domain. It is likely that the Runge–Kutta method could achieve the same accuracy in greatly reduced time if the integration were stopped when the substrate concentration is zero far from the source. Therefore, because of the ambiguity of the relative and absolute error tolerances used in the Adam's method, as well as its complexity, use of the fourth–order Runge–Kutta solution technique was continued for the reaction equations. If greater efficiency is needed, the Runge–Kutta integration need not be performed when the substrate or biomass concentration is zero or approximately zero.

## 3.5 Summary

The objective of this chapter was to develop and test a versatile two–dimensional groundwater transport model that is capable of handling different types of biodegradation kinetic models. Operator splitting was chosen due to the ease of implementation of different biodegradation kinetic models, and the flexibility resulting from solving the reactive and nonreactive equations separately using appropriate numerical methods. The nonreactive transport equation was solved using the principle direction finite element method and the reaction equations were solved using a fourth–order Runge–Kutta algorithm. The model accuracy was verified by comparing its results with analytical solutions for a one and two–dimensional transport model with linear kinetics. The developed two–dimensional transport model with nonlinear biodegradation kinetics was shown to have greater efficiency at intermediate levels of accuracy when compared to an iterative finite element approach.

# 4. EFFECT OF THE TYPE OF BIODEGRADATION KINETIC MODEL UPON GROUNDWATER TRANSPORT

## 4.1 Introduction

Proper modeling of reactive solute transport requires that the biodegradation rate term is the simplest one that accurately represents the kinetics. Chapter 2 described the following three main alternatives for groundwater modeling: Monod, microcolony, and biofilm models. The Monod model is the simplest option, because it assumes that all of the biomass is exposed to the bulk concentration, S. Microcolony and biofilm models are more complicated to formulate and solve, because they include mass transfer resistance to bring the substrate from the bulk liquid to the attached bacteria. Both models use Fick's first law to describe how external mass transport reduces the substrate concentration at the outer surface of the microcolony or biofilm. However, the biofilm model includes mass transport resistance within the biofilm, while the microcolony model assumes that the substrate concentration throughout the microcolony is uniform and equal to the concentration at the microcolony/fluid interface.

The fundamental question for model development is this: Are the added complexities of the microcolony and biofilm models necessary to have an accurate representation of biological reactions in *in situ* bioreclamation? If external and internal mass-transport resistances are not important for the environments of *in situ* bioreclamation, the simple Monod model can be employed, thereby reducing model complexity and computational intensity. Therefore, the objectives of this chapter are as follows:

1. Use dimensionless analysis to formulate quantitative criteria that determine when the Monod and biofilm models give significantly different results.
2. Perform numerical simulations using both the Monod and biofilm biodegradation models (i.e., the simplest and most complicated cases) for realistic scenarios of *in situ*

bioreclamation. In particular, ascertain whether or not the biofilm model provides significant changes in the predictions, in comparison with the simpler Monod model.

## 4.2 Critical Presentation of Monod and Biofilm Equations

The primary objective of this chapter is to address the major differences between the Monod and biofilm models when combined with solute transport processes in groundwater. To define clearly the differences between kinetic models, the equations expressing each kinetic type for a single rate limiting substrate are compared critically. Limiting cases when the Monod and biofilm models collapse to the same form are presented.

The Monod reaction term for a single limiting organic compound is given simply as

$$R_s = M_T q_m \left(\frac{S}{K_s + S}\right) \tag{4.1}$$

However, the implementation of biofilm kinetics is more involved due to the consideration of simultaneous reaction and diffusion within the biofilm and external mass transport. A brief description of the equations which make up the biofilm model is given here; further details are provided by Rittmann and McCarty (1980). Simultaneous reaction and molecular diffusion within the biofilm at steady state are represented by the following equation:

$$D_f \frac{\partial^2 S_f}{\partial z^2} = q_m \frac{X_f S_f}{K_S + S_f} \qquad 0 \le z \le L_f \tag{4.2}$$

where $D_f$ is the molecular diffusion coefficient in the biofilm (typically $0.8D_m$, where $D_m$ is the molecular diffusion coefficient of the substrate in the water), $S_f$ is the substrate concentration within the biofilm, and z is the distance within the biofilm, i.e., within $L_f$. Although the biofilm thickness is assumed to change with time, the concentration profile within the biofilm is assumed to be at steady-state, because the time scales of diffusion and reaction are much shorter than the time scales of biofilm growth or decay (Kissel et al., 1984).

In addition to these processes, external mass transport is assumed to take place across the diffusion layer, L, which represents the amount of mass transfer resistance from the bulk fluid to the surface of the biofilm. The rate of mass-transport across the external diffusion layer is defined by Fick's first law as

$$J = D_m \frac{S - S_S}{L} \tag{4.3}$$

where J is the flux of substrate per unit area of the biofilm surface, $D_m$ is the molecular diffusion coefficient of the substrate, S is the bulk substrate concentration, and $S_s$ is the substrate concentration at the interface between the diffusion layer and biofilm. L is usually estimated from empirical equations available in the chemical engineering literature; they express the mass transfer coefficient, $k_m = (D_m/L)$, as a function of system parameters, e.g. the Reynold's number, Re, and the Schmidt Number, Sc. The actual diffusion layer thickness is found dividing the molecular diffusion coefficient by the mass transfer coefficient.

Appropriate boundary conditions for equations (4.2) and (4.3) are zero flux at the interface where the biofilm adheres to the solid substratum,

$$\frac{\partial S_f}{\partial z} = 0 \quad @ \quad z=0 \tag{4.4}$$

and continuity of substrate concentration at the interface between the biofilm and the liquid,

$$S_f = S_s \quad @ \quad z=L_f \tag{4.5}$$

$S_s$ is generally less than S, the bulk substrate concentration, because of external mass transport.

Rittmann and McCarty (1981) found a pseudo-analytical solution of (4.2) through (4.5). It expresses J as a function of S, $L_f$, and the other appropriate physical and biological kinetic parameters; the detailed procedure was presented in Chapter 3. The pseudo-analytical solution was built on the work of Atkinson and How (1974), who defined J as

$$J = \eta q_m X_f L_f \frac{S_s}{S_s + K_S} \qquad (4.6)$$

where $\eta$ is a parameter which expresses the ratio of the actual flux, J, to the flux for a biofilm with no internal diffusion. The numerical procedure to find $\eta$, as well as the influence of external mass transport, also was presented in Chapter 3. The solution is highly nonlinear and involves an iterative Newton–Raphson procedure when the biofilm is not fully penetrated. The flux, J, is obtained in a dimensionless domain with the key variables being $\tau = (2D_f K_S / q_m X_f)^{1/2}$ (a characteristic length scale), $L_f^* = L_f/\tau$ (the dimensionless biofilm thickness), and $L^* = L/\tau$ (the dimensionless diffusion layer thickness).

The biofilm kinetic expression given in equation (4.6) collapses to the Monod equation (4.1) when external mass transport resistance is neglected (i.e., $S = S_S$), internal mass transfer resistance is negligible (i.e., $\eta = 1$), and $M_T = aX_f L_f$. The key to assessing the differences between the Monod and biofilm models is to find whether conditions existing in groundwater give $\eta$ not equal to unity or S not equal to $S_S$. Several dimensionless parameters developed in the next section are the keys to assessing whether or not external and internal mass transfer resistances included in the biofilm model are truly important.

## 4.3 Presentation of Dimensionless Parameters

The purpose of this section is to present and discuss three dimensionless parameters to aid in discerning the difference between the Monod and biofilm models for conditions of *in situ* bioremediation. These parameters allow assessment of the relative importance of internal diffusion to biological reaction and external mass transport to biological reaction for the biofilm model and a comparison of the total mass biodegraded to the total mass of advected substrate for both the Monod and biofilm models. Two parameters have already been presented in the biofilm literature. They are $L_f^*$ and $L^*$, which have already been defined.

Within the biofilm, the "competing" processes of internal diffusion and biological reaction occur in parallel. The previously defined $L_f^*$ is the key dimensionless parameter that indicates the relative importance of internal diffusion and biological reaction. Suidan et al. (1987) demonstrated through a graphical procedure that when $L_f^* > 3.0$, transient biofilms are deemed deep (the concentration goes to zero within the biofilm), and when $L_f^* < 0.20$, the biofilms are fully penetrated (no substrate gradient within the biofilm). In other words, the effects of internal diffusion within the biofilm can be completely neglected when $L_f^* < 0.20$, and become most important when $L_f^* > 2.0$ (Suidan et al., 1987). In the intermediate range, the importance of internal diffusion is intermediate and is of the same order as the biological reaction rate. Thus, the Monod model is possible when $L_f^*$ is less than 0.20.

External transport occurs "in series" with the processes of internal diffusion and biological reaction. Heath et al. (1990) state that when $L^*$ is $< 0.01$ for a steady-state biofilm, the effect of external mass transport can be considered negligible, but the importance of external mass transport increases as $L^*$ increases above this value. Suidan et al. (1987) refined this broad generalization by showing the effect of external mass transport is a function of the degree of substrate penetration and whether the Monod kinetics are zero or first order. In short, fully penetrated first–order biofilms were found to be most affected by external mass transport, whereas zero–order deep biofilms were not affected at all. Since the $L^*$ value is not a fixed criteria for external mass transport resistance, a more complete analysis of external mass transport incorporating the effect of the degree of saturation ($S/K_S$) is necessary.

Here we analyze the case most strongly affected by external mass transport, namely, the fully penetrated biofilm. Mass balance requires the flux across the external mass transport diffusion layer to be equal to the mass degradation rate within the fully penetrated biofilm. Thus,

$$J = \frac{D_m}{L}(S - S_f) = \eta q_m X_f L_f \frac{S_f}{K_S + S_f} \tag{4.7}$$

Assuming the biofilm is fully penetrated, the value of $\eta$ is set equal to unity. The above equation with the fully penetrated assumption can be nondimensionalized by letting $\beta = S_f/S$ and $\kappa = K_S/S$ and can be written as

$$\frac{SD_m}{Lq_m X_f L_f}(1-\beta) = \frac{\beta}{\kappa + \beta} \tag{4.8}$$

The term on the left hand side is a new dimensionless group, which is defined as

$$D_{a(mt)} = \frac{LL_f X_f q_m}{SD_m} \tag{4.9}$$

or, using the previously introduced dimensionless groups, as

$$D_{a(mt)} = 2L^* L_f^* D_f^* \frac{K_S}{S} = 2L^* L_f^* D_f^* \frac{1}{S^*} \tag{4.10}$$

The newly defined Damkohler number, $Da_{(mt)}$, is a convenient dimensionless parameter that can be used to estimate the effect of external mass transport in fully penetrated biofilms. It represents the ratio of the maximum possible reaction rate ($q_m X_f L_f$) to the maximum possible rate of external mass transport ($D_m S/L$). Substituting the definition of the Damkohler number into equation (4.8) yields

$$\frac{1}{D_{a(mt)}}(1-\beta) = \frac{\beta}{\kappa + \beta} \tag{4.11}$$

This final form of the equation is similar to equation (4.5) from Bailey and Ollis (1986, pp. 205) and can be solved analytically to examine the effect of $Da_{(mt)}$. The analytical solution of equation (4.11) takes the form

$$S_f^* = -\frac{\xi}{2} + \frac{\sqrt{\xi^2 + 4\kappa}}{2} = \frac{\xi}{2}\left[\sqrt{1 + \frac{4\kappa}{\xi^2}} - 1\right] \tag{4.12}$$

where $\xi = Da_{(mt)} + \kappa - 1$. The analytical solution can be simplified under two extreme conditions, namely, when $Da_{(mt)}$ approaches zero or infinity. In the first case, when $Da_{(mt)}$ approaches zero, equation (4.12) reduces to $S_f^* = S^*$. An extremely small $Da_{(mt)}$ is a direct result of low external mass transport resistance (i.e., small $L^*$ or high S) or very slow biological reaction. The second case is when $Da_{(mt)}$ approaches infinity, and equation (4.12) reduces to $S_f^* = 0$. $Da_{(mt)}$ gets large when the external mass transport resistance becomes dominant (i.e., large $L^*$ or small S) or when the biological reaction is very fast. Another important consideration is to recognize that $Da_{(mt)}$ is also a function of $L_f^*$ and, as a result, $Da_{(mt)}$ can change significantly with biomass growth. This is because, as stated earlier, $Da_{(mt)}$ represents a ratio of the maximum possible biodegradation rate to the maximum possible external mass transfer rate. Therefore, as the biomass accumulation increases (i.e., $L_f$ increases), the maximum possible biodegradation rate ($q_m X_f L_f$) also increases. Since the biological reaction rate is increased, it is more likely that external mass transport is the rate-limiting step. Also as $L_f^*$ increases, the likelihood of significant internal mass transport resistance increases (i.e., if $L_f^* > 0.2$); in the analysis here, I assume that the biofilm is fully penetrated, which means that $L_f^*$ must be less than or equal to 0.2.

The dimensionless parameters discussed so far ($L_f^*$, $L^*$, and $Da_{(mt)}$) give insight into the interaction of processes occurring at the "REV" scale in a natural system. However, the total flux of the bulk fluid substrate into and out of the REV will be controlled by advection and dispersion; hence these processes greatly affect the amount of biological growth in the subsurface. This can be addressed by the examination of another dimensionless parameter, $Da_{MAC}$, which is equal to the mass degraded in a single discrete finite element of the domain over one time step divided by the mass advected into the element over one time step. That is, the total mass degraded = $R_S \cdot \Delta x \cdot A_c \cdot \Delta t$, where $A_c$ is the cross sectional area, and the total mass advected = $\epsilon v S_{in} \cdot A_c \cdot \Delta t$, where $S_{in}$ is the substrate concentration upgradient of the element. $Da_{MAC}$ takes the form

$$Da_{MAC} = \Delta x q_m M_T (S_{in}/(K_S + S_{in})/(\epsilon v S_{in}) \qquad (4.13)$$

This quantity takes a form similar to the Damköhler number commonly used in the field of biochemical engineering to evaluate the importance of biological reaction in relation to other important physical properties (Boucher and Alves, 1959). Equation (4.13) assumes the reaction rate of the substrate, $R_S$, remain constant over the first grid block. Very large values of $Da_{MAC}$ imply that the system is "reaction–controlled", and, hence, most of the substrate mass is degraded over the first grid block adjacent to the source. In this case, the issue of choosing among the biological kinetic submodels becomes moot because the numerical discretization is too coarse to resolve the small–scale biological processes. In other words, any kinetic model can be chosen when $Da_{MAC}$ is very large because the grid spacing is too coarse to resolve profiles of biomass and substrate. In this case, the biological reaction appears to be nearly instantaneous for the given resolution, and a simple instantaneous model, such as that of Borden and Bedient (1986), may by appropriate. A detailed explanation of the relationship between a large $Da_{MAC}$ and the grid spacing, $\Delta x$, will be given towards the end of the chapter.

Now that the dimensionless parameters have been developed, they can be used to aid in drawing some general conclusions regarding the differences between Monod and biofilm kinetics under bioremediation conditions. First, we know that if $L_f^*$ is high (i.e. $> 2.0$), internal diffusion within the biofilm will be significant and if $Da_{(mt)}$ is large ($> > 1$), external mass transfer resistance will be significant. Under these circumstances, the Monod model, as it is depicted in this dissertation, is not valid. Moreover, we require a relatively low $Da_{MAC}$ in order to resolve the biomass and substrate profiles. These parameters will be used to analyze the results of numerical experiments in order to corroborate the conclusions drawn from the following section which examines the influence of realistic ranges of groundwater parameters upon the submodels of interest.

## 4.4 Realistic Parameter Ranges for Groundwater Environments

The preceding development demonstrated that the differences between the Monod and biofilm models became significant for large $L_f^*$ and $Da_{(mt)}$. So, the key issue is whether

realistic parameter ranges for groundwater environments will give high values of the dimensionless parameters. Compared to traditional fixed bed bioreactors designed for wastewater treatment, the subsurface environment is characterized by small grain sizes, i.e. high specific surface area, and low flow velocities . As a result of this, a few general conclusions regarding the differences between the Monod and biofilm models can be drawn.

The substrate flux or loading equals $\epsilon v S_{in}$, where $S_{in}$ is the influent substrate concentration. In general, then, we expect low substrate loadings and subsequent biological growth for groundwater, due to the low water velocities. Also, because $M_T = aX_f L_f$, the higher surface areas for groundwater systems results in thinner biofilms than for traditional bioreactors. Hence, we expect small values of $L_f$ (and hence $L_f^*$), suggesting that internal mass transport limitation may be negligible in groundwater systems. Although relatively little information is available regarding external mass transport in natural porous material, the small $L_f^*$ will tend to give small $Da_{(mt)}$, suggesting that external mass transport also may be negligible in groundwater systems. Furthermore, the low substrate loadings can give a large $Da_{MAC}$, resulting in the need for a small grid spacing to resolve the biological processes.

Now that some general conclusions regarding the possible differences of Monod and biofilm models have been made, it is interesting to examine recent laboratory and field studies designed to study bioremediation conditions. These studies will be analyzed in order to determine the validity of the aforementioned generalizations.

The importance of internal diffusion is illustrated by the Moffett field experiment, conducted by a group of researchers at Stanford University. The Moffett results support the conclusion that biofilm models may not be necessary in natural groundwater environments. Semprini and McCarty (1989) used double-Monod kinetic expressions and incorporated them into one-dimensional transport equations describing the pulse injection of oxygen and methane. The developed model was used to describe the results of

the field experiments. In order to calculate an $L_f^*$ from their modeling parameters, certain biofilm parameters were estimated. All the relevant parameters needed to calculate $L_f^*$ are provided in Table 4.1. The $X_f$ value, estimated based on the work of Odencrantz et al. (1990), was 15.0 mg/cm$^3$, and the $D_f$ value of 1.0 cm$^2$/day was estimated using the Wilke–Chang correlation (Bird et al., 1962). The representative particle diameter was estimated as the $d_{50}$ particle diameter from a particle size distribution of the porous media at the Moffet field site. The kinetic parameters, $q_m$ and K, are for the electron donor, methane. The value of the greatest biofilm thickness was calculated from the maximum reported biomass concentration and was $8.65 \times 10^{-6}$ cm or 0.0865 μm, which translates to an approximate maximum dimensionless biofilm thickness of the Moffett field experiment of $1.06 \times 10^{-3}$. This value, being approximately two orders of magnitude lower than the 0.2 cutoff for fully penetrated biofilms, supports use of the Monod model.

Table 4.1. Parameters used to Determine the Maximum $L_f^*$ at Moffet Field

| Reported Parameters+ | Assumed Values |
|---|---|
| $q_m$ = 2.0 g/g–day | $d_p$ = 2.75 mm |
| $K_{Methane}$ = 1.0 mg/L | $X_f$ = 15.0 mg/L |
| $M_T$ = 5.75 mg/L | $D_f$ = 1.0 cm$^2$/day |
| $\epsilon$ = 0.33 | |

+ from Semprini and McCarty (1990)

Taylor and Jaffe (1990) reported the results of laboratory experiments which were designed to mimic biological growth in the subsurface. Two columns were operated with slightly different flow velocities. The larger velocity column, i.e., 27.2 m/day interstitial velocity, carried a methanol concentration of 7.2 mg/L. This relatively high organic loading to the column led to a large biomass buildup, much larger than for more typical groundwater settings. The measured maximum biofilm thickness at the upstream end of the column was approximately 150 μm at 84 days into the column operation, which corresponded to steady–state conditions. The kinetic parameters, $q_m$ and K, were found from batch tests to be 7.7 mg methanol (mg bacteria day)$^{-1}$ and 0.799 mg/L, respectively.

The $D_f$ value was reported to be 0.83 $cm^2$/day, and the $X_f$ value was assumed to be 3.0 $mg/cm^3$. A $L_f^*$ value of 1.40 was calculated, which included their assumption of 70% active biomass; this $L_f^*$ falls within the range of shallow biofilms by the criteria of Suidan et al. (1987). However, Taylor and Jaffe (1990) assumed an $\eta$ value of one in their subsequent modeling runs, totally ignoring the effect of internal diffusion and were able to successfully able to model their experimental results. They ignored internal mass transport resistance after finding an initial effectiveness factor of slightly less than one at the injection port at steady-state. The bottom line is that internal diffusion had only a small effect within the first grid block .

In the next section, numerical simulations are conducted in order to corroborate the conclusions based upon analysis of the dimensionless parameters. The numerical experiments were designed to provide a rigorous test of the conclusions using realistic bioremediation physical and biological parameters.

## 4.5 Numerical Simulations Comparing Biofilm and Monod Kinetics For Single Substrate Limitation

The previous analysis showed that differences between the Monod and biofilm degradation models are dependent upon the dimensionless parameters $L_f^*$, $Da_{(mt)}$, and $Da_{MAC}$. In order to corroborate the above conclusions, I performed simulations of solute transport for a range of typical groundwater scenarios and examined the magnitudes of the resultant difference between the Monod and biofilm models. The numerical results will help demonstrate what values of the dimensionless parameters are needed to create a significant difference between model simulations. First, a base case of typical two-dimensional groundwater transport and biodegradation parameters is presented. Second, a similar transport problem, but with an exaggerated amount of external mass transport is conducted to illustrate what conditions are required to make external mass transport important. A third transport simulation aimed at illustrating the effect of

exaggerated internal diffusion resistance demonstrates the conditions required to make $\eta$ less than one.

### 4.5.1 Base Case

The base represents a typical situation for *in situ* bioremediation. A two-dimensional transport problem demonstrates biomass development and the biodegradation of an electron donor when the electron acceptor is in excess concentration (single substrate limitation). One-dimensional flow in a cross-section of a coarse sand aquifer is considered. Figure 4.1 shows the two-dimensional domain, physical and kinetic parameters, and numerical discretization criteria used in the analysis. A series of numerical experiments demonstrates the implication of using the biofilm versus Monod model.

All parameter values were selected to be typical of groundwater environments. The values are typical in that they fall within the ranges for sand and gravel aquifers reported in the groundwater modeling literature. The particle diameter was chosen to be 1.0 mm (classified as coarse sand by the USGS, Todd, 1980), which corresponds to a specific surface area of 111 $cm^{-1}$. The flow velocity of 1.0 m/day was chosen because it is on the high end of velocities found in *in situ* remediation schemes (Staps, 1989). The longitudinal dispersivity of 0.03 cm was selected based upon the work of Klotz and Moser (1974), who conducted numerous laboratory experiments to measure hydrodynamic dispersion coefficients. The transverse dispersivity was calculated from an assumed value of $\alpha_L/\alpha_T$ of 20, which is in the range commonly found in nature (Sudicky, 1983). The kinetic parameters shown in Figure 4.1 were taken from the work of Odencrantz et al. (1990). The kinetic parameters are for acetate when it completely limited the kinetics in a denitrifying column. The only parameter which differs from that published in the original report is the maximum specific rate of substrate utilization ($q_m$), which had an average value of 2.14 mg acetate as Soluble Organic Carbon (SOC)/mg cell-day. The value of $q_m$ listed in Figure 4.1 was taken to be five times lower than this value, 0.42 mg SOC/mg cell-day, to

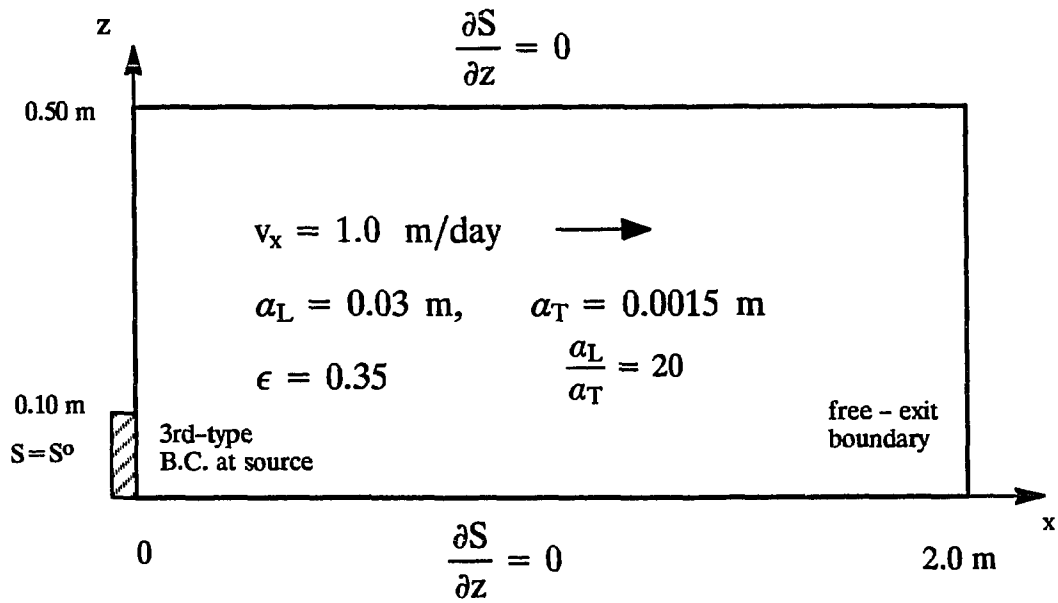


## Kinetic Parameters

### Monod

$q_m$ = 0.420 mg SOC/mg cell-day
K = 0.218 mg/L
Y = 0.678 mg cells/mg SOC
b = 0.07 day $^{-1}$

### Biofilm

$X_f$ = 15.0 mg cells/cm$^3$
$D_m$ = 1.07 cm$^2$/day
$D_f$ = 0.856 cm$^2$/day
$d_p$ = 0.10 cm
L = 0.0176cm
$q_m$, K, Y, and b same as Monod.

## PDFEM and Operator-Splitting Parameters

$\Delta x$ = 0.027m
$\Delta z$ = 0.020m
$\Delta t$ = 0.011 day

Peclet # = 0.89
Courant # = 0.375
$\varrho_1$ and $\varrho_2$ = 0.423 - .040
Runge - Kutta Steps = 50

Figure 4.1. Domain and parameters used for the single substrate limitation experiments.

represent the lower growth rates found in nature (Hirsch, et al., 1979) and to account for the lower temperatures found in natural groundwater.

The initial biomass concentration is one of the most important parameters to estimate. Numerous reports (Blackwill, 1989; Colwell, 1989; Harvey et al. 1984; Jensen, 1989; Van Beelen, et al., 1989; Wilson et al., 1983) of the total number of bacteria found in natural groundwater environments give a range from $10^5 - 10^7$ cells/gram of dry soil, with the actual values depending upon the conditions at a particular field location. The total number of cells includes active and dormant bacteria, as well as numerous different species. Staps (1989) found in a field study of hydrocarbon degradation that approximately one percent of the total cell count was metabolically active. A cell concentration of $10^6$ cells/gram of dry soil was chosen to represent the intermediate numbers of total cells found in nature. All of the cells were assumed to be metabolically active and of the same bacterial species whose growth kinetics are defined. The concentrations expressed in terms of mg cells/L (assuming a particle density of the sand of 2.3 g sand/cm$^3$) is 0.427 mg cells/L of voids, respectively {The actual concentration is calculated from ($10^6$ cells/gram of dry soil)(2.3 g sand/cm$^3$ sand)($10^{-13}$ gram dry/cell)((1−$\epsilon$)/($\epsilon$))($10^3$ cm$^3$/L)($10^3$ mg/g)=0.427 mg dry cells/L of voids}. Another assumption in calculating the cell concentration is that the weight of the cells is $10^{-13}$ gram dry weight/cell (Mallette, 1969; Bouwer and McCarty, 1984; and Neidhardt et al. 1990 ). The relatively low cell weight is attributed to small bacterial sizes (dwarf cells) found to be abundant in oligotrophic environments, such as groundwater.

Given the parameters values discussed above, it is possible to estimate values of the dimensionless parameters. The initial $\tau$ value is 7.697 x $10^{-3}$ cm (recall that $\tau=(2D_fK/q_mX_f)^{1/2}$). The initial biofilm thickness can be determined from the total background cell concentration and the equality $M_T=aX_fL_f$ presented previously. The initial biofilm thickness is 0.0025 $\mu$m and, when divided by the $\tau$ value, yields a dimensionless thickness of $3.32x10^{-5}$. Because the initial $L_f^*$ value is much less than 0.20,

the initial biofilm is fully penetrated. The small initial biofilm thickness is much less than the typical size of bacterial cells found in nature, i.e., 0.5–1.0 μm, and could be thought as equivalent to having microcolonies sparsely dotting the surfaces of the sand particles. Thus, the assumption of uniform coverage of the soil particle probably is not valid on the microscopic scale (μm), but it is a reasonable approximation for the macroscale (cm). The diffusion layer thickness, L, was determined from the correlation of Jennings reported by Namkung et al. (1983) and is 0.0176 cm, which corresponds to a dimensionless diffusion layer thickness of 2.3 ($L^* = L/\tau$). According to Heath et al. (1990), this represents the potential for a substantial amount of external mass transport limitation for a steady–state biofilm; however, the initial $Da_{(mt)}$ value of $2.65 \times 10^{-6}$ suggests the relative importance of external mass transport is initially very low. The initial conditions give small values of $L_f^*$ and $Da_{(mt)}$, suggesting that the Monod model is sufficient. However, both $L_f^*$ and $Da_{(mt)}$ will increase as a result of biomass growth. The initial $Da_{MAC}$ of the base case has a value of $1.30 \times 10^{-3}$ and will increase as a result of biomass growth.

The initial conditions have no rate–limiting organic in the domain, and the microbial concentration is uniform at $10^6$ cells/g of dry soil. The rate–limiting organic compound is input at the rate of 350 mg S/day distributed evenly over the 0.1 m injection line, i.e. a third–type boundary condition with the injection concentration equal to 10.0 mg S/L (see Figure 4.1).

Simulation results can be examined in several different ways. The curves of total organic and biomass in the domain as a function of time provide a concise, integrated view of the system. These basic forms of graphic presentation provide general knowledge of the overall behavior of the system for a given set of physical and kinetic parameters. It is appropriate to show snapshots of the organic plume and the biomass distribution; however, it is not practical to show them at every time step. The contour plots are useful in determining the spatial distribution of the plume and biomass and will be utilized at

certain points in this thesis only when necessary. For example, they will be used to assess the effect of transverse dispersion in this and later chapters.

The following two figures demonstrate graphically the results of the base case simulations using biofilm and Monod kinetics. Figure 4.2 is a plot of the total amount of rate–limiting substrate in the domain as a function of time. The total amount of substrate in the system at a given time was calculated by integrating over all the nodes in the numerical domain by use of the trapezoidal integration rule. Because the Monod and biofilm kinetic results give the same mass curve, only one line can be detected, i.e., the lines lie exactly on top of one another. The rising limb from zero to three days is linear at a slope approximately equal to 350 mg S/day. The biodegradation rate starts to increase dramatically around day three due to the new growth of biomass. From day 3 until the end of the simulation, the amount of organic substrate in the system gradually decreases, despite the continued input of 350 mg/day. Thus, biodegradation, once begun, removes nearly all the input organic and that previously input.

Figure 4.3 shows the total amount of biomass in the system. The rapid growth from day five to 20 slows thereafter until the end of the simulation. The simulation was forced to stop when the fractional change in the total amount of biomass in the system over one time step was less than $\Omega$, the stopping criteria, which was set at 0.001%. This occurred at day 27.9. The $\eta$ values were identically equal to one (a fully penetrated biofilm) at all nodes at all times (data not shown). The maximum biomass concentration, which was at the source, and at steady–state was 151.2 mg/L. This yields a maximum $L_f^*$ of 0.012, which corresponds to an actual thickness of 0.91 μm and is an order of magnitude less than the upper limit for a fully penetrated biofilm. The value of $Da_{(mt)}$ at the source at steady–state was $8.83 \times 10^{-4}$ and increased down gradient of the source to a maximum value of approximately 8.7. The $Da_{MAC}$ at the source at steady–state was 0.47. The $Da_{MAC}$ value was calculated using the maximum biomass concentration, 151.2 mg/L, as the $M_T$ in equation (4.13).

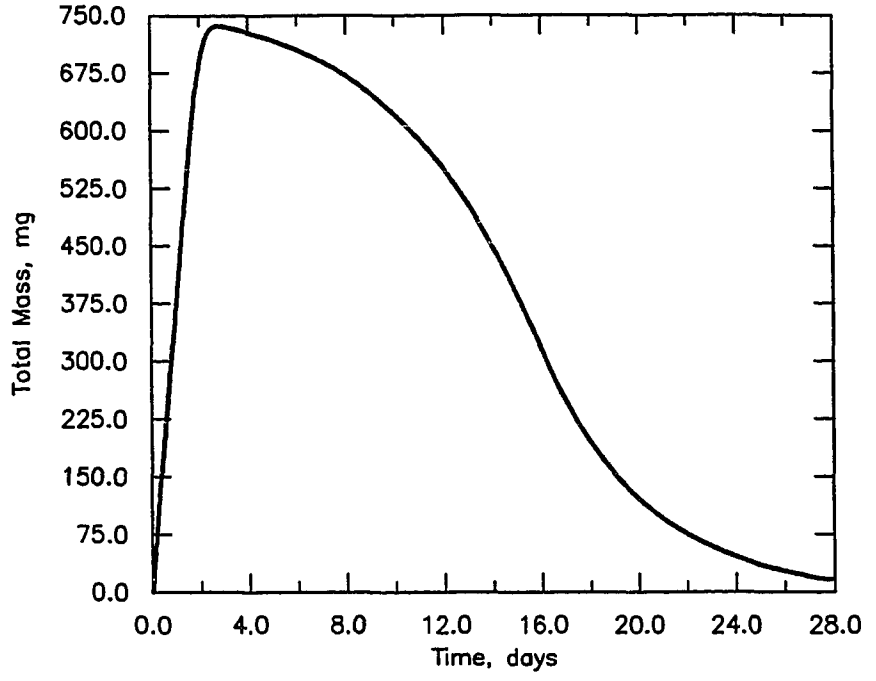


Figure 4.2 Total organic mass in the system for both Monod and biofilm kinetics for the base case simulation.

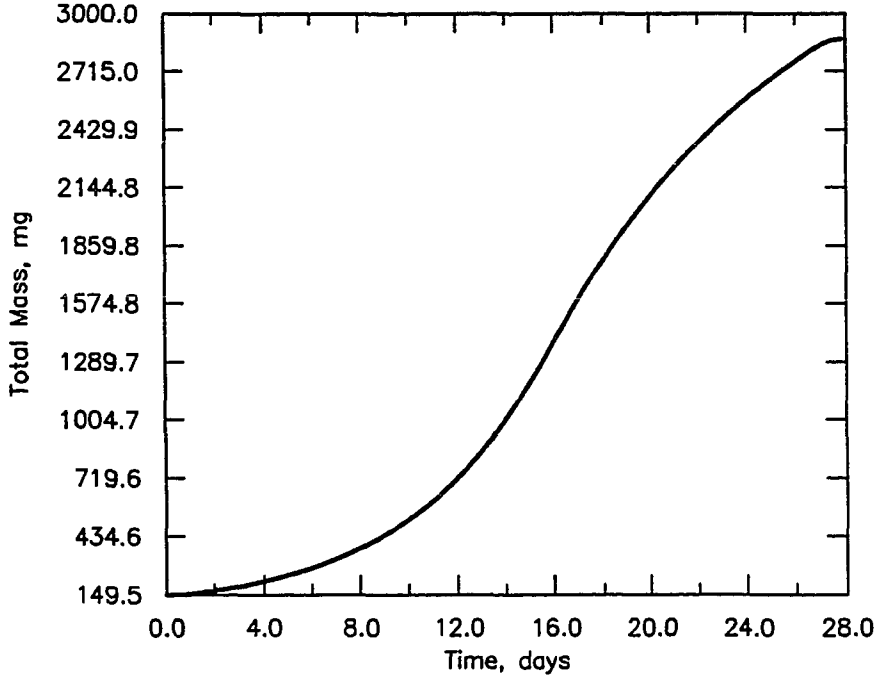


Figure 4.3 Total biomass in the system for both Monod and biofilm kinetics for the base case simulation.

The spatial distribution of biomass and organic compound can be examined in some detail with the use of contour plots showing approximate locations of lines of equal biomass and organic concentration. Snapshots at 13.2 days and 26.4 days provide the most useful information. These times are halfway to the steady-state and at steady-state, respectively. Figure 4.4 shows contour plots of organic and biomass at 13.2 days into the run. A substantial amount of transverse dispersion of the organic allowed noticeable biomass growth in the transverse direction above the plane on top of the injection. The greatest amount of biomass developed close to the source. By day 13.2, the isoconcentration lines of the organic were retracting back towards the source, due to biomass growth as a result of the organic accumulation and the buildup of enough biomass to consume a measurable amount of substrate.

Figure 4.5 shows the spatial distributions of organic compound and biomass close to steady-state at 26.4 days (i.e., the actual steady-state was at 27.91 days). There is a dramatic buildup of biomass near the source. Also, the transverse spreading has virtually ceased as a result of the buildup of biomass close to the source.

### 4.5.2 Exaggerated External Mass Transport

To illustrate the effect of external mass transport processes, the diffusion layer thickness was increased significantly to a dimensionless diffusion layer thickness of 100, as opposed to 2.3 used in the previous section. However, to simulate a dimensionless diffusion layer thickness of 100.0, the actual thickness of the layer must be 0.769 cm. This is unrealistically large when compared to the particle diameter of 0.1 cm, but the idea is to show the behavior of the biofilm model when subjected to such a large amount of external mass transport resistance. The initial $Da_{(mt)}$ of this run increases from $2.65 \times 10^{-6}$ in the base case to $1.15 \times 10^{-4}$ here. The initial $L_f^*$ and $Da_{MAC}$ are the same as in the base case, i.e. $3.32 \times 10^{-5}$ and $1.30 \times 10^{-3}$, respectively. It is obvious from the following result that this large amount of external mass transport resistance has a substantial effect on the kinetics.

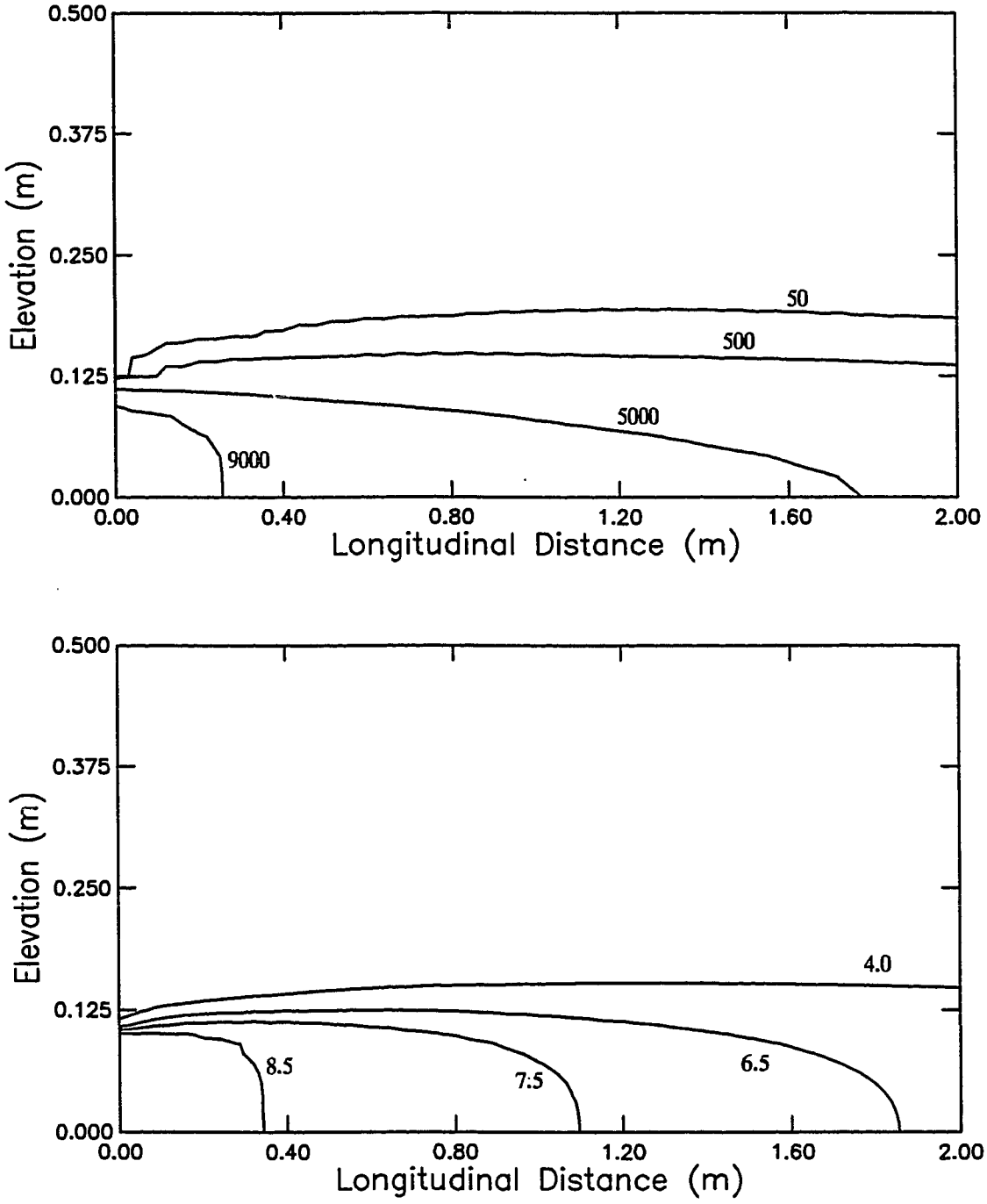


Figure 4.4 Contour plots of organic compound (top) and biomass (bottom) at 13.2 days into the simulation. The organic concentration is expressed in μg/L and the biomass concentration in mg/L.

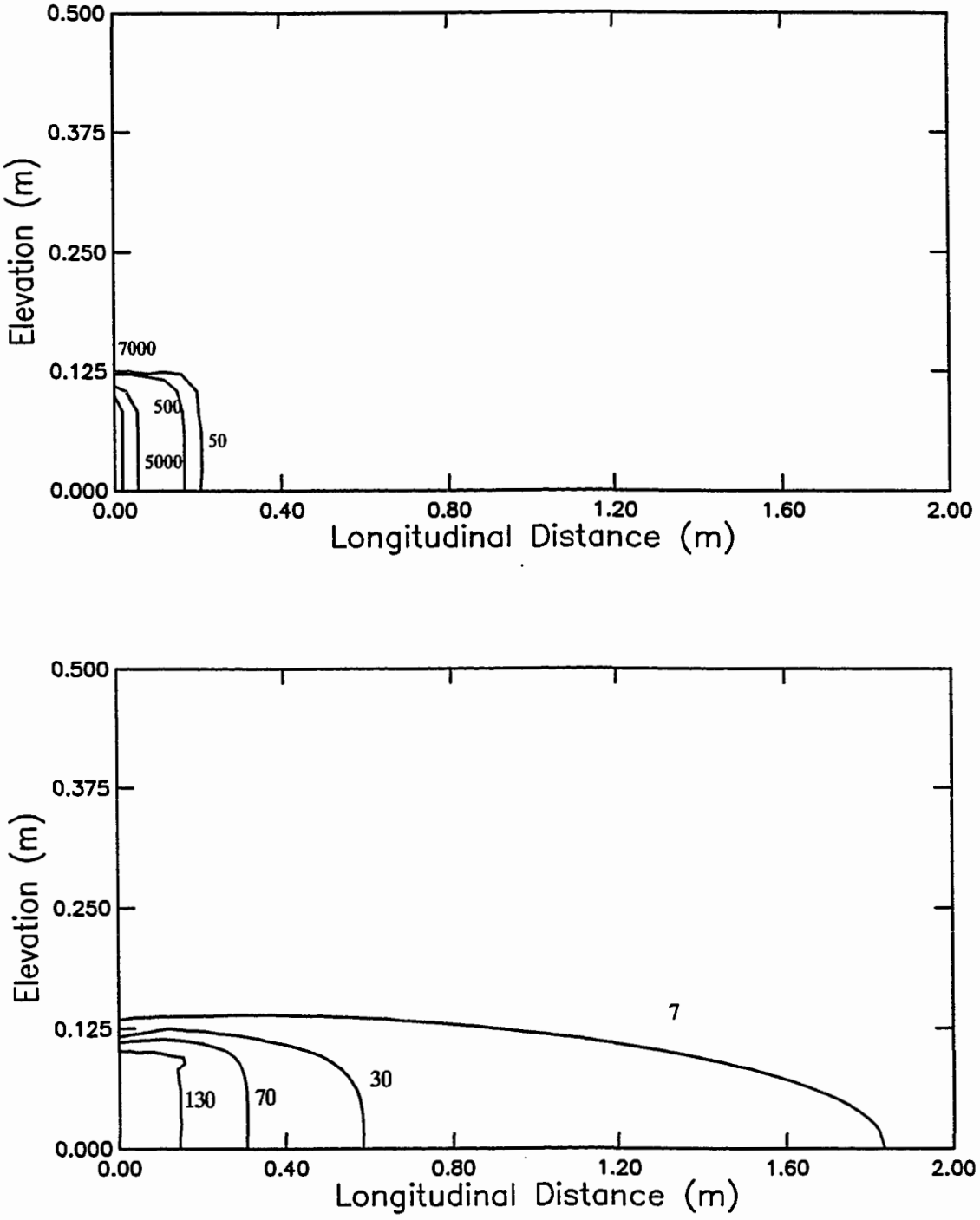


Figure 4.5 Contour plots of organic compound (top) and biomass (bottom) at 26.4 days into the simulation. The organic concentration is expressed in μg/L and the biomass concentration in mg/L.

There has been much controversy in defining an actual value of the diffusion layer (Nicoud and Schweich, 1989). The controversy arises because numerous correlations available from the chemical engineering literature provide varying estimates of the diffusion layer thickness for the same hydrodynamic conditions. Most of the correlations are given as a power function of the Reynolds number ($vd_p/\nu$) and Schmidt number ($\nu/D_m$) and have four empirically determined constants. Nicoud and Schweich (p. 1079, 1989) sum up the problem nicely as follows: "Contradictory results show that no reliable estimate of the external mass transfer coefficient is available for low liquid velocities, and a lot of work remains to be done to predict reliable mass transfer coefficients in beds packed with particles smaller than 1 mm at a particle Reynolds number smaller than 1." Since the particle Reynolds number is 0.0116 for the example presented in the previous section, the controversy implies a large degree of uncertainty with any diffusion layer thickness calculated from any of the available empirical models.

Figure 4.6 displays longitudinal profiles of the organic compound at 26.4 days along the bottom of the domain ($z=0$) shown in Figure 4.1. There is a substantial difference in the curves starting from 0.20 m from the source. Approximately 96.4% of the rate-limiting substrate had been removed 0.20 m from the source. The effect of the increased external mass transport resistance is noticed downstream of this point due to the increased rate of external mass transport relative to the rate of substrate utilization. The steady-state of this run with the larger diffusion layer thickness was reached at 27.88 days as opposed to 27.91 for the base case. The total organic mass of the base case was less by by 3.56% at 26.88 days and 0.044% at 13.44 days when compared to the total organic mass in the system for this section, i.e. the biofilm model large external mass transfer resistance.

To examine the effect of external mass transport in more detail, the newly developed $Da_{(mt)}$ is applied to the profile given in Figure 4.6. The $Da_{(mt)}$ is calculated at three locations: at the source, 0.50 m from the source, and 1.0 m from the source. Table 4.2 shows the $Da_{(mt)}$ at the three different locations as well as the $L_f^*$ and S values. $Da_{(mt)}$

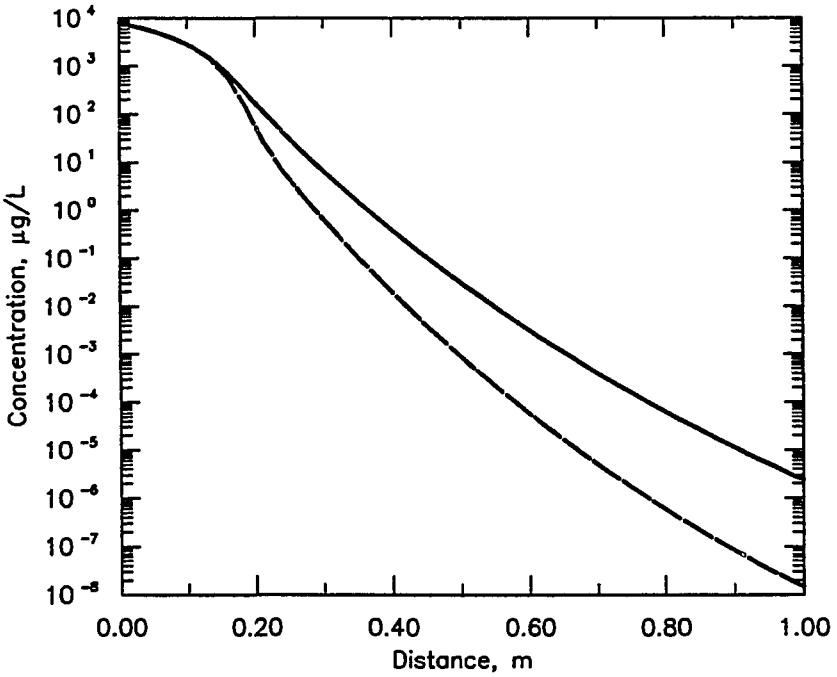


Figure 4.6 Longitudinal profile of the organic compound at time 26.4 days. Dashed line is Monod and solid line is biofilm with $L^* = 100.0$.

changes throughout the domain, as opposed to the previously used parameter, $L^*$, which would be equal to 100 everywhere at every time. The S values are the values taken from the profile in Figure 4.6. At the source, $Da_{(mt)} << 1$, which verifies that the extreme case of the analytical solution of low $Da_{(mt)}$ is correct, i.e., there is no effect of external mass transport. At 0.50 m from the source, the $Da_{(mt)}$ is much greater than 1, which is an example of the other extreme of the analytical solution when $Da_{(mt)} >> 1$, i.e., the effect of external mass transport resistance serves to lower $S_f$ toward zero. The final location at x= 1.0 m reinforces the extreme of high $Da_{(mt)}$ in that the differences between Monod and biofilm increases as $Da_{(mt)}$ increases. In general, Figure 4.6 shows that the influence of external diffusion upon the profiles increases downgradient of the source, which is consistent with the $Da_{(mt)}$ values listed in Table 4.2. The values for $Da_{(mt)}$ at the three locations downstream of the source (0 m, 0.5 m, and 1.0 m) at day 26.4 for the base case run were $8.83 \times 10^{-4}$, $7.8 \times 10^{-2}$, and $4.3 \times 10^{-1}$, respectively. All of these values of the $Da_{(mt)}$

are below unity and support using the dimensionless number, because there were no differences in the longitudinal profiles of Monod and biofilm cases in the previous section.

Table 4.2 $Da_{(mt)}$ Values at Three Locations Along the Longitudinal Profile of Figure 4.6 for the Biofilm Curve.

| | x=0 | x=0.50m | x=1.0m |
|---|---|---|---|
| Approximate S (μg/L) | 5,000. | 0.0141 | $8.83 \times 10^{-7}$ |
| $L_f'$ | 0.011 | $2.63 \times 10^{-3}$ | $1.08 \times 10^{-3}$ |
| $Da_{(mt)}$ | $3.84 \times 10^{-2}$ | 649.8 | $4.50 \times 10^{6}$ |

In summary, the effect of external mass transport resistance had a substantial effect when it was increased to a high value. The effect increased dramatically with decreasing concentration, because the substrate concentration driving the rate of external mass transport became very small. The use of the $Da_{(mt)}$ number should prove to be a useful tool to determine when the effect of external mass transport may be significant, however, its *apriori* usage is limited, because the substrate profile needed to determine S (and $L_f$) can only be determine by use of the numerical model.

4.5.3 Exaggerated Internal Diffusion

The effect of exaggerated internal diffusion can be illustrated by considering an extreme variant of the base case problem. Several test cases were examined by increasing the loading rate, $vS_o$, the maximum specific rate of utilization, $q_m$, and lowering the actual amount of internal diffusion, $D_f$. The loading rate increased the growth and removal potential, and $q_m$ and $D_f$ had a direct effect in increasing the initial dimensionless biofilm thickness. Other approaches to yielding larger biofilm thickness include increased particle diameter, i.e. lower a, increased background concentration of bacteria, and variation of other kinetic parameters. These would defeat the purpose of our attempt at isolating the effect of internal diffusion by losing sight of the contributions offered by each of the processes. In order to have a sufficient loading and subsequent utilization develop a

thick biofilm, an atypical group of groundwater parameters was needed. The key parameter variations are shown in Table 4.3. In summary, the velocity was increased by an order of magnitude, the influent organic substrate concentration increased by a factor of five, $q_m$ increased by a factor of twenty, and $D_f$ was decreased by a factor of 1.6.

Table 4.3 Physical, Kinetic, and Numerical Parameters for Exaggerated Internal Diffusion Example

| New Physical and Kinetic Parameters | Changes in Numerical Parameters | |
|---|---|---|
| $v = 10.0$ m/day | Pe = 0.89 | $\rho_2 = 0.825$ |
| $S^o = 50.0$ mg/L | Co = 0.41 | $\rho_1 = 0.464$ |
| $q_m = 8.4$ mg SOC/mg $NO_3^-$-N-day | $\Delta x = 0.026$m | $\rho_1/\rho_2 = 0.563$ |
| $D_f = 0.5D_m = 0.535$ cm$^2$/day | $\Delta z = 0.020$m | RK Steps = 50 |
| | $\Delta t = 0.0011$day | |

The results of the exaggerated internal mass transport simulation are shown in two different ways. First, the mass curve of the total amount of organic mass in the system is shown to illustrate the response of the system under the different conditions, and, second, a plot of the $\eta$ values along the length of the longitudinal axis at steady-state is shown to illustrate the impact of extreme internal diffusion. The new kinetic parameters yield a new initial dimensionless biofilm thickness of $2.84 \times 10^{-2}$, as opposed to $7.697 \times 10^{-3}$ in the base case. The initial $Da_{MAC}$ was $5.33 \times 10^{-4}$ for this simulation, which is approximately two and a half times smaller than the value of $1.33 \times 10^{-3}$ for the base case. The value of $Da_{MAC}$ is lower because the loading rate is larger in comparison to the initial reaction rate than in the base case.

Figure 4.7 shows the total mass of organic for the biofilm and Monod runs with the new parameters in Table 4.3. Even for this case of exaggerated internal diffusion, the Monod and biofilm models give the same mass curve. There was a rise to a maximum of 3520 mg at 0.27 days. After that, the biomass grew at a rapid rate and was able to consume the organic already in the system, as well as that being injected. The overall kinetic response was extremely fast compared to the base case as a result of the larger loading and

$q_m$. The steady state of the system occurred at 1.661 days for the Monod kinetic case and 1.660 days for the biofilm kinetic case.

The maximum biofilm thickness close to steady-state (at t= 1.65 days) at the source was 24.2 μm. The corresponding $L_f^*$ is 85.0, by the criteria of Suidan et al. (1986) a deep biofilm. This is not surprising because of the extremely high loading and $q_m$. The removal over the first $\Delta x$ at steady-state was approximately 99.990%, implying most of the substrate was utilized in the first 2.66 cm. This is reflected in the $Da_{MAC}$ value, which is 5.03. The actual value of concentration at 2.66 cm into the domain for the Monod and biofilm models was 2.32 μg/L and 5.31 μg/L, respectively. This corresponds to a 43.7% lower concentration for the biofilm model. The effect of this is negligible, however, because of the extreme removal; there is no detectable difference from the mass curves of Figure 4.7 because the total mass in the system is extremely low. In a final graphical illustration of the differences in the models, Figure 4.8 shows values of the effectiveness factor, $\eta$, along the bottom of the grid from the source to 0.50 m at steady-state. The minimum $\eta$ value, 0.3994, occurs at the source and implies the actual flux at the source is approximately only 40% the maximum fully penetrated flux. The $\eta$ values rapidly approach and reach one at 0.25 m. The impact of the $Da_{MAC}$ is discussed below.

The results of the previous section demonstrate the impact of a substantial amount of internal diffusional resistance within biofilms as a result of high loading and degradation rates. Because of the high loading and utilization rate, an enormous amount of biomass accumulated in the system. The film thickness reached a maximum of 24.2 μm, corresponding to a deep biofilm. Nearly all the substrate was removed in the first 2.66 cm of the system at steady-state, i.e., 99.99%. The actual difference in the total amount of organic mass in the system for the Monod and biofilm model simulations was virtually undetectable compared to the enormous degradation that took place in the system. Therefore, the importance of internal diffusion was negligible in terms of the total organic

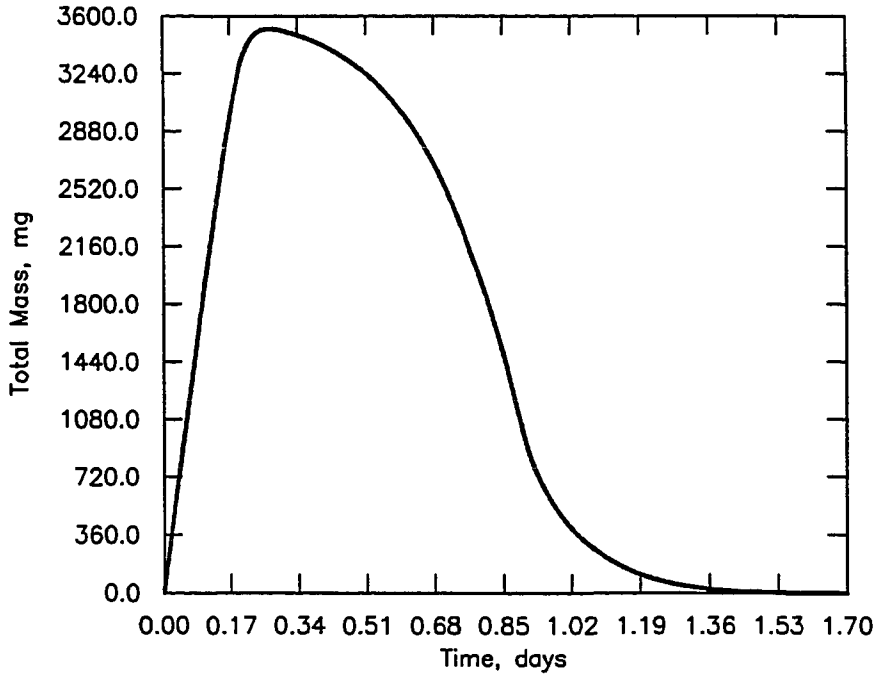


Figure 4.7 Total mass of organic in the system for simulation of exaggerated internal mass transport for Monod and biofilm kinetics.

removal in the system, even for this set of extreme groundwater physical and biological parameters.

Before closing this section, the $Da_{MAC}$ values will be discussed in further detail. Table 4.4 shows the initial and steady-state $Da_{MAC}$ values for the simulation of this section and the base case simulation. The initial $Da_{MAC}$ values are comparable in that both are much less than unity. At steady-state, both $Da_{MAC}$ values at the source increase significantly from biomass growth. The steady-state value at the source is 0.44 for the base case, and it is 5.03 for the case of higher loading. It is important to keep in mind the total amount of growth that has occurred at the source. Table 4.4 shows that there were 2.5 orders of magnitude new growth for the base case and nearly 4 orders of magnitude new growth for the case of exaggerated internal diffusion. Although the absolute values of the $Da_{MAC}$ make sense in that the largely loaded and faster kinetics case's absolute value was greater, there was also nearly 1.5 orders of magnitude more biomass growth. Therefore, care

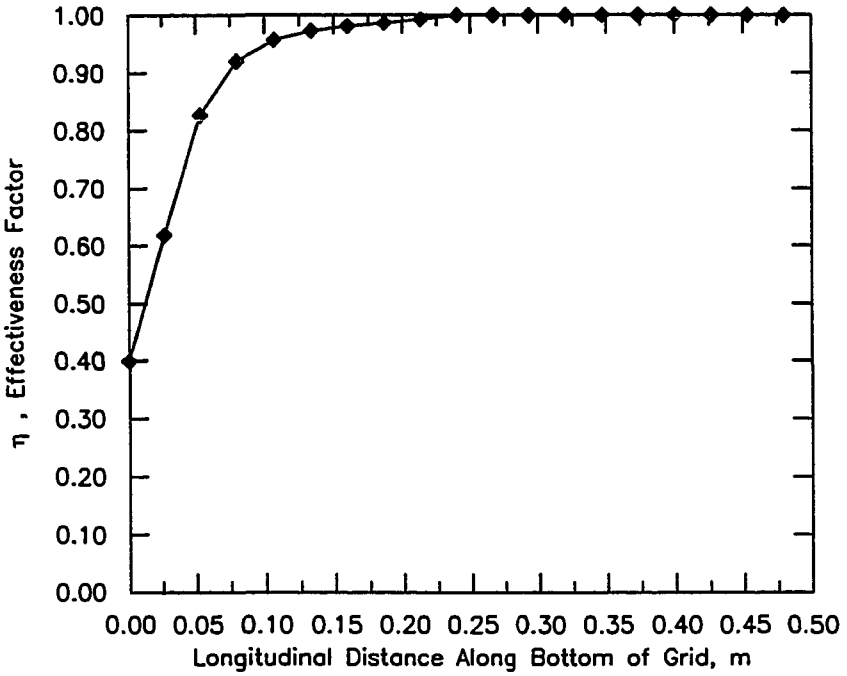


Figure 4.8 Effectiveness factor along the bottom of the grid at 1.65 days for the biofilm simulation.

should be taken when trying to infer too much from the $Da_{MAC}$. Its primary function is to compare biodegradation kinetics relative to the loading rate.

Table 4.4 $Da_{mac}$ and Related Values at Steady-state for the Base Case and Exaggerated Internal Diffusion Simulations.

| | Initial $Da_{MAC}$ | S.S. $Da_{MAC}$ | Ratio | log Ratio |
|---|---|---|---|---|
| Base Case | $1.30 \times 10^{-3}$ | 0.47 | 361.5 | 2.56 |
| This Section | $5.33 \times 10^{-4}$ | 5.03 | 9433 | 3.97 |

The prime use of $Da_{MAC}$ is to weigh the longitudinal grid-spacing with respect to the resolution of the biomass distribution and the biological reaction kinetics. For example, the simulation with the larger loading had a steady-state $Da_{MAC}$ at the source of 5.03, and 99.99% of the substrate was lost in the first $\Delta x$ (0.026m). If the interest in the problem was the biomass distribution or substrate concentration profile in the first 0.26m of the system,

the grid–spacing was not adequate to resolve the profile in this region. The steady–state $Da_{MAC}$ of 5.03 is a measure of this poor resolution and could be used to determine a different grid–spacing to resolve the gradients close to the source. For example, if a new $\Delta x$ of 0.0026m were used, the final $Da_{MAC}$ at the source would be 0.503 and the profile in the first 0.026m would be resolved by a factor of ten. For now, the improved resolution with decreasing grid size is left as a hypothesis; however, coupling of spatial scale ($\Delta x$) and biological resolution is obvious. Depending on the spatial scale of the problem, the handling of the biological kinetics changes substantially. When the domain to be modeled is very large, the use of the instantaneous biological kinetic model of Borden and Bedient (1986) may be appropriate because $Da_{MAC}$ must be large because of the large $\Delta x$. A large $Da_{MAC}$ implies that the biomass present in a grid cell of length $\Delta x$ has the ability of totally degrading the influent substrate. In other words, the advecting substrate will be degraded completely over a time scale less than the the time required to advect a distance of $\Delta x$. When *in situ* bioremediation is applied, the scale of the problem is reduced substantially because the nutrient injection and subsequent biomass growth is a more localized phenomena, tending to lower the grid–spacing requirement. If the instantaneous reaction is not desired, $Da_{MAC}$ must be kept small, and the most practical way to do so is to decrease the grid–spacing.

## 4.6 Summary, Conclusions, and Discussion

This chapter examined the differences between the Monod and biofilm models when applied to a realistic set of physical and biological parameters in a two–dimensional transport problem. Dimensionless parameters were developed and then discussed in terms of their values for realistic groundwater conditions. General conclusions were developed that suggested the difference between the Monod and biofilm models would be low in conditions appropriate for *in situ* bioreclamation. Numerical experiments were then conducted to corroborate the conclusions based upon the dimensionless parameters.

The results showed that the models gave identical results when the biomass attained a defined steady–state as a result of a continuous injection of a rate–limiting substrate for a base case simulation. An additional numerical experiment examined the effect of increasing the amount of external mass transport by increasing the thickness of the diffusion layer to an extreme to illustrate its impact. This large amount of external mass transport had a substantial impact on the difference between the models, and a newly developed dimensionless parameter, $Da_{(mt)}$, was applied to determine when external mass transport is important. External mass transport was shown to be important when the newly developed $Da_{(mt)}$ was substantially greater than one. The last numerical experiment performed in the chapter was a simulation of a system with a large loading and faster biodegradation kinetics to illustrate an exaggerated amount of internal diffusion resistance. While this simulation resulted in a thick biofilm with a significant amount of internal diffusion, the removal was so intense that the difference between the Monod and biofilm models were virtually insignificant in terms of the total organic removal. However, the true distinctions between the models were blurred because the grid spacing was too large. The final point was the use of a dimensionless parameter, $Da_{MAC}$, to weigh the longitudinal grid–spacing versus the resolution of the biomass distribution and substrate utilization. To prevent ensure proper resolution of the biological reaction, $Da_{MAC}$, must be kept less than about 1.0. However, based upon analysis of realistic groundwater parameters, the potential for a large difference between the Monod and biofilm models was shown to be low.

Because external mass transport and internal diffusion processes, specific to the biofilm model, may not be insignificant in every bioremediation field site, use of the dimensionless numbers presented in this chapter provides general guidelines regarding whether or not these processes are important. These dimensionless numbers include $Da_{MAC}$, $Da_{(mt)}$, and $L_f^*$. The dimensionless parameters, $L_f^*$ and $Da_{(mt)}$ can be used to determine the relative importance of internal diffusion and external mass transport,

respectively. In addition, $Da_{MAC}$ can be used to assess the maximum reaction rate to the loading rate at various times throughout the simulation and can be used to estimate whether the grid spacing is adequate to resolve the important biological phenomena. One important weakness with the use of the dimensionless numbers is that they depend upon the solution of the mathematical model and thus cannot provide any definite *apriori* determination as to if the biofilm and Monod models will differ or as to what the long term performance of the system. This problem is inherent in the nonlinear nature of the system.

The internal diffusional component of the biofilm model often can be neglected safely when modeling biodegradation processes in groundwater. External mass transport resistance is an extremely uncertain parameter and can become increasingly important for extremely low Reynolds number, i.e., natural groundwater conditions. Therefore, the general statement that external mass transport resistance can be ignored contains considerably more uncertainty than for internal diffusion.

# 5. COMPARISON OF MULTIPLICATIVE AND MINIMUM-RATE MONOD KINETICS IN A TWO-DIMENSIONAL TRANSPORT PROBLEM

## 5.1 Introduction

The biofilm and Monod models were examined in the previous chapter. For most practical purposes we found that the added sophistication of the biofilm model is not warranted, and the Monod model can be used to describe the rate of biodegradation. A second issue for biodegradation modeling in groundwater is whether minimum-rate or multiplicative Monod kinetics give significantly different results when the electron donor and electron acceptor are present at sub-saturating values. Dual-limitation occurs when there are simultaneously low to intermediate concentrations of the electron donor and electron acceptor, which is the case in most field scale bioremediation scenarios. Kindred and Celia (1989) and Odencrantz et al. (1990) used the minimum rate approach, in which only one substrate can control the biomass growth of the system, while MacQuarrie et al. (1990) and Borden and Bedient (1986) presented applications of the dual-substrate kinetic approach, in which the electron donor and electron acceptor contribute to controlling the overall biomass growth in the system. However, to date, there has been no detailed investigation of the differences between the two kinetic approaches.

A thorough modeling evaluation is necessary, because the nonlinear and coupled nature of the transport problem may camouflage any differences between the minimum-rate- and multiplicative Monod models. The objective of this chapter is not to prove whether dual or single substrate limitation is correct, but rather to examine conditions for which the models yield significantly different results under transport conditions appropriate for *in situ* bioremediation. Accordingly, this chapter focuses upon the following two specific questions:

1. What are the nature and magnitude of the effects of the multiplicative versus minimum-rate kinetics upon substrate degradation and biomass growth?

2. What are the key variables that control these differences? In other words, what conditions are necessary to cause a major difference between the two kinetic models?

The first part of this chapter deals with simplifying the algebraic forms of the minimum–rate and multiplicative kinetic expressions, which leads to hypotheses about the impact of each kinetic model upon the transport simulations. Then, the latter part of the chapter contains a series of computer simulations to corroborate and refine the hypotheses.

## 5.2 Critical Presentation of the Monod Equations

The multiplicative Monod model has been applied to biodegradation in groundwater by Borden and Bedient (1986) and MacQuarrie et al. (1990). The distinguishing feature of the multiplicative Monod model (M) is that both substrates play a role in determining the actual reaction rate for each individual substrate. The reaction rates for the electron donor and electron acceptor, as well as for the biomass, are given by the following equations.

$$R_S = M_T q_{mS}\left(\frac{S}{K_s + S}\right)\left(\frac{A}{K_A + A}\right) \tag{5.1}$$

$$R_A = \gamma M_T q_{mS}\left(\frac{S}{K_s + S}\right)\left(\frac{A}{K_A + A}\right) = \gamma R_S \tag{5.2}$$

$$R_M = Y_S M_T q_{mS}\left(\frac{S}{K_s + S}\right)\left(\frac{A}{K_A + A}\right) - bM_T + bM_{To} \tag{5.3}$$

where $Y_S$ is the yield coefficient for the electron donor and the other parameters and variables have been defined previously. In general, the multiplicative rates give a low reaction rate when $A < K_A$ and $S < K_S$.

The second approach is to assume that only one substrate limits the reaction, i.e. there is no dual–limitation, and the rate of the nonlimiting substrate is determined from the limiting reaction rate and an appropriate stoichiometric coefficient. This biodegradation approach is referred to as the minimum–rate Monod (MR) and was applied to

groundwater by Kindred and Celia (1989) and Odencrantz et al. (1990). If the organic compound is assumed to limit the reaction, the appropriate kinetic equations are

$$R_S = M_T q_{mS}\left(\frac{S}{K_s + S}\right) \tag{5.4}$$

$$R_A = \gamma M_T q_{mS}\left(\frac{S}{K_s + S}\right) = \gamma R_S \tag{5.5}$$

$$R_M = Y_S M_T q_{mS}\left(\frac{S}{K_s + S}\right) - bM_T + bM_{To} \tag{5.6}$$

The other possibility is if the electron acceptor limits the kinetics. This is expressed similarly by the following three equations:

$$R_A = M_T q_{mA}\left(\frac{A}{K_A + A}\right) \tag{5.7}$$

$$R_s = \frac{1}{\gamma} M_T q_{mA}\left(\frac{A}{K_A + A}\right) = \frac{1}{\gamma} R_A \tag{5.8}$$

$$R_M = Y_A M_T q_{mA}\left(\frac{A}{K_A + A}\right) - bM_T + bM_{To} \tag{5.9}$$

where $q_{mA}$ is the maximum specific rate of substrate utilization of the electron acceptor, and $Y_A$ is the yield coefficient for the electron acceptor when it is the rate-limiting substrate.

The key question now is to determine when the electron donor or electron acceptor limits the reaction rate for the case of minimum-rate limitation application. Williamson and McCarty (1976) and Rittmann and Dovantzis (1983) presented a relationship for determining which substrate limits the kinetics for the single-substrate limitation model. These investigators found that if the inequality

$$\frac{S_A}{S_S} < \frac{K_A}{K_S} \tag{5.10}$$

is true, then the electron acceptor is the minimum-rate (rate-limiting) substrate, and equations (5.7)-(5.9) are used to describe the fully penetrated kinetic case. When the

inequality (5.10) is false, the electron donor is the minimum-rate (rate-limiting) substrate, and equations (5.4)-(5.6) are used to describe the kinetics.

It should be noted that it is possible for true single substrate limitation to occur in the field. That is, either the electron acceptor or the electron donor could be in excess concentration so only one or the other compound would limit the kinetics. For example, when $S >> K_S$ and $A << K_A$, the electron acceptor limits the kinetics, and when $S >> K_S$ and $A << K_A$, the electron donor limits the kinetics. Under theses circumstances, the M and MR models are identical. However, in many practical scenarios, dual limitation applies, since the electron donor and electron acceptor are present at comparable levels.

Differences between the two models can be seen easily when a few simplifications are made to the two rate equations. Before these simplified equations are presented, it is important to make a clarification. First, consider the balanced stoichiometric equation for the biological reaction of electron donor and electron acceptor to produce cells and other products (adapted from Rittmann and Dovantzis, 1983):

$$\alpha_1 S + \alpha_2 A \rightarrow \alpha_c(\text{cells}) + \alpha_p(\text{products})$$

where $\alpha_1$, $\alpha_2$, $\alpha_c$, and $\alpha_p$ are all stoichiometric coefficients of the electron donor, electron acceptor, biomass, and other products. The rate of reaction is assumed to be balanced in that the rate of substrate utilization of the reactants and production of products have consistent stoichiometric coefficients (Rittmann and Dovantzis, 1983). This is represented by

$$\frac{q_{mS}}{q_{mA}} = \frac{a_1}{a_2} = \gamma^{-1}$$

This equation implies that the expressions $q_{mS} = (1/\gamma) q_{mA}$ or $q_{mA} = \gamma q_{mS}$ can be used interchangeably and thus will be throughout the remainder of this chapter.

The MR (minimum-rate) and M (multiplicative) kinetic relationships can be simplified to zero-order, as shown in Table 5.1. The M and both MR reaction rates reduce to exactly the same form in the zero-order range, i.e., when $S >> K_S$ and $A >> K_A$. Thus,

for a situation where the kinetics are known to be zero-order *apriori* and remain zero-order throughout, it makes no difference which kinetic expression is chosen.

Table 5.1 Kinetic Expressions for Zero-Order Kinetics ($S >> K_S$ and $A >> K_A$) for Both Multiplicative and Minimum-Rate

| |
|---|
| $R_S = M_T q_{mS} = \frac{1}{\gamma} M_T q_{mA}$ |
| $R_A = \gamma q_{mS} M_T = M_T q_{mA}$ |
| * $R_G = Y_S M_T q_{mS} = Y_A M_T q_{mA}$ |

* $R_G$ is the total biomass growth rate, the first term in $R_M$.

The selected kinetic formulation does make a difference when the reaction equations are simplified to first-order, i.e., $S << K_S$ and $A << K_A$. Table 5.2 shows the simplified kinetic equations for the multiplicative and minimum-rate expressions with electron donor and electron acceptor limitation. The simplified multiplicative equation predicts far lower reaction and growth rates than that of the minimum-rate due to multiplication by the product of the two terms ($S/K_S$) and ($A/K_A$), each of which is much smaller than unity. The K values are large with respect to the substrate concentration in order to be first-order, which makes the overall M first-order rate exceedingly small. Also, when either the electron donor or electron acceptor limits the rate for the MR case, the kinetic expressions are quite different compared to the M kinetic expressions. The only thing that is certain is that the MR reaction rate will be much higher, because there is only one K in the denominator and one substrate concentration in the numerator, as opposed to two in M. Therefore, the extreme in the differences will occur when first-order kinetics occurs for both substrates. In general, the reaction rate of M could be several orders of magnitude lower than MR if both substrates are in the first-order range.

As an example of quantification of the differences for an intermediate case, consider the form of the reaction equations when $S = K_S$ and $A = K_A$. Table 5.3 shows the form of the reduced reaction equations when the kinetics are in the middle of the hyperbolic

Table 5.2. Kinetic Expressions for First-Order Kinetics ($S << K_S$ and $A << K_A$)

| Multiplicative | Minimum-Rate (S) | Minimum-Rate (A) |
|---|---|---|
| $R_S = \frac{M_T q_{mS}}{K_S K_A} SA$ | $R_S = \frac{M_T q_{mS}}{K_S} S$ | $R_S = \frac{M_T q_{mA}}{\gamma K_A} A$ |
| $R_A = \frac{\gamma M_T q_{mS}}{K_S K_A} SA$ | $R_A = \frac{\gamma M_T q_{mS}}{K_S} S$ | $R_A = \frac{M_T q_{mA}}{K_A} A$ |
| $R_G = \frac{Y_S M_T q_{mS}}{K_S K_A} SA$ | $R_{GS} = \frac{Y_S M_T q_{mS}}{K_S} S$ | $R_{GA} = \frac{Y_A M_T q_{mA}}{K_A} A$ |

regime for the assumed case that $\mu_S = \mu_A$. The rates of substrate utilization of the electron donor and electron acceptor, as well as the growth rate of the bacteria for multiplicative kinetics, are exactly one-half those of the minimum-rate rates. The effects of this kind can have a substantial difference and are demonstrated for transport modeling in the following sections.

Table 5.3. Kinetic Expressions in the Middle of the Hyperbolic Range ($S = K_S$ and $A = K_A$)

| Multiplicative | Minimum-Rate (Both S and A) |
|---|---|
| $R_S = M_T q_{mS}(\frac{1}{4})$ | $R_S = M_T q_{mS}(\frac{1}{2})$ |
| $R_A = \gamma M_T q_{mS}(\frac{1}{4})$ | $R_A = \gamma M_T q_{mS}(\frac{1}{2})$ |
| $R_G = Y_S M_T q_{mS}(\frac{1}{4})$ | $R_G = Y_S M_T q_{mS}(\frac{1}{2})$ |

In summary, the following conclusions can be made regarding the differences between the M and MR expressions. The MR and M models will differ the most when the electron donor and electron acceptor are in the first-order range simultaneously. The difference between the M and MR kinetic expressions will be somewhat less when electron donor and electron acceptor concentration are comparable to their half-velocity constants. The MR and M expressions will be identical when either true single substrate limitation

occurs, i.e. the electron acceptor or electron donor is in excess, or when both the electron donor or electron acceptor are in excess simultaneously and are thus both in the zero-order range. In the next sections, these conclusions will be verified by conducting computer simulations for a variety of cases.

## 5.3 Comparative Example in a Two-Dimensional Homogeneous Domain

Both kinetic approaches were applied to a problem similar to the one presented in Chapter 4. The case has denitrification occurring in a domain having uniform concentration of acetate throughout and clean water with nitrate at 10.0 ppm injected into the domain via a 0.10m injection well to stimulate the organisms that degrade the acetate. Acetate is also injected at 5.0 mg/L uniformly across the upstream end of the domain (0.50m), which allows a constant source of electron donor for biomass development at the injection well. Figure 5.1 is a diagram showing the domain and the concentrations of electron donor and electron acceptor used in the example problem. The velocity has been lowered by an order of magnitude in this example in comparison to that used in the previous chapter to increase the importance of biodegradation relative to advection.

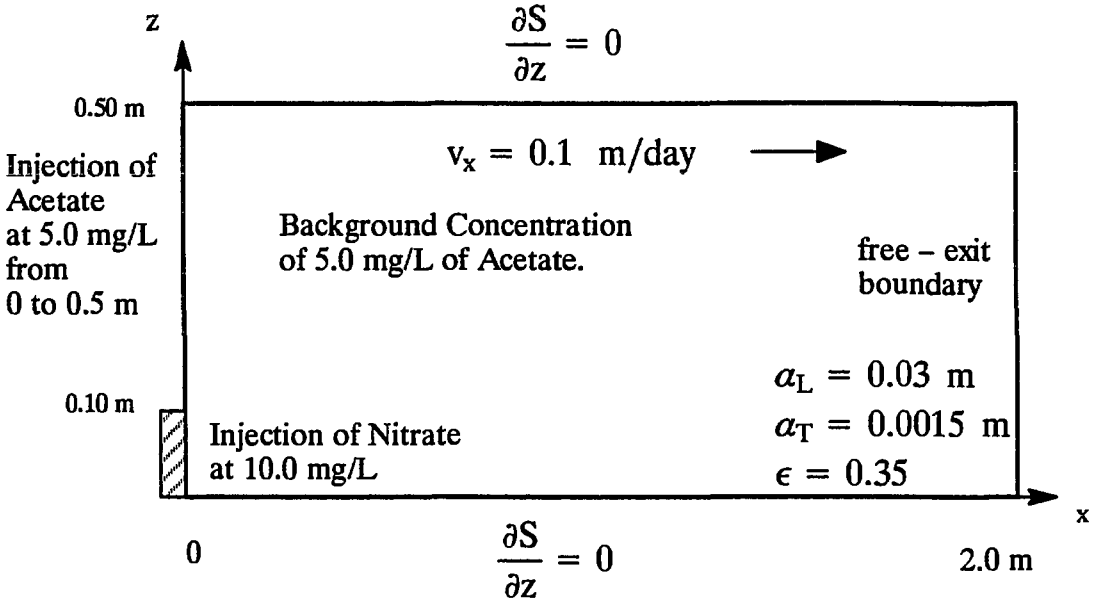


Figure 5.1. Domain and parameters used for the minimum-rate and multiplicative experiments.

The domain and parameters shown in Figure 5.1 were selected for comparing MR and M for three reasons. First, the continuous injection and background concentration of acetate allowed for a constant source of 'contamination' that would typify a groundwater remediation scheme. Second, the electron acceptor was injected only from 0–0.1 m in the lower right–hand corner of the domain to allow transverse spreading of the electron acceptor into the electron donor plume. Third, the combined effect of the first and second effects allowed two distinct regions of substrate limitation. In general, if the kinetics are fast enough, the electron donor will limit the reaction close to the source, and the electron acceptor will limit the kinetics as it spreads transversely into the electron donor plume. It is of paramount importance that there are two distinct regions where both substrates limit the kinetics in order to fairly illustrate the range of differences between MR and M.

The acetate kinetic parameters and the background biomass concentration are the same as those in the previous chapter and are shown in Table 5.4. Some additional parameters appear for the electron acceptor, nitrate. Nitrate has a $K_A$ value of 0.146 mg/L and a maximum specific utilization rate, $q_{mA}$, of 0.29 mg $NO_3^-$–N mg $cell^{-1}$ $day^{-1}$. The grid spacing and Runge–Kutta steps are also shown in Table 5.4; the advective and dispersive time step was changed to 0.10 days to preserve the order of the Courant number used in the base case numerical simulation of Chapter 4. The initial $Da_{MAC}$ for the electron donor and electron acceptor are 0.027 and 0.00941, respectively. The $Da_{MAC}$ is approximately an order of magnitude greater here than in the base case of Chapter 4, implying the initial reaction rate is ten times greater compared to the loading rate. The parameters shown in Table 5.4 were used in simulations with both M and MR. The simulations were run to an approximate steady–state, which was defined by less than a 0.01% ($\Omega$) change in the total amount of biomass in the domain.

The following series of figures shows the results of the comparison of the two different kinetic expressions implemented into the example problem defined above, which we denote as Case 1. As we discussed with the simplification of the kinetic equations in the

Table 5.4 Numerical and Monod Kinetic Parameters: Case 1

| Electron Donor | Electron Acceptor |
|---|---|
| $q_{mS}$ = 0.42 mg SOC/mg cell-day | $q_{mA}$ = 0.29 mg $NO_3^-$-N/mg cell-day |
| $K_S$ = 0.218 mg/L | $K_A$ = 0.146 mg/L |
| $Y_S$ = 0.678 mg cells/mg SOC | $Y_A$ = 0.983 mg cells/mg SOC |
| $D_m$ = 1.07 $cm^2$/day | $D_m$ = 1.07 $cm^2$/day |

$\gamma$ = 0.69 mg $NO_3^-$-N/mg SOC, $d_p$ = 1mm
$M_{To}$ = $10^6$ cells/gram = 0.427 mg cells/L of voids

PD and Operator Splitting Parameters

| | |
|---|---|
| $\Delta x$ = 0.026m | Pe = 0.858, Co = 0.375 |
| $\Delta z$ = 0.020m | $\rho_1$ = 0.437 |
| $\Delta t$ = 0.10day | $\rho_2$ = 0.776, $\rho_1/\rho_2$ = 0.563 |
| Runge-Kutta Steps = 50 | |

previous section, there should be no great difference between the simulations, since the electron acceptor and electron donor are zero-order, i.e. no significant effects stemming from the hyperbolic range. Figure 5.2 shows the total amount of acetate in the system throughout the simulation. Although the two curves are quite close, larger times show slightly more mass in the M system. Figure 5.2 also shows that the total mass of electron acceptor in the system increases from zero to approximately 375 mg at steady-state. However, the greatest difference in the curves is when the accumulation of $NO_3^-$ levels off, before steepening again near 14 days. The difference in the curves is due to the rapid consumption of nitrate, due to the rapid growth of biomass, at which time the electron acceptor kinetics were slightly hyperbolic. Figure 5.2 finally shows the total biomass in the system versus time for both the kinetic expressions as well. As in the mass curve of the electron donor, the difference between the MR and M curves is slight. The $Da_{MAC}$ at steady-state for the electron donor and electron acceptor are 2.27 and 0.776, respectively, which indicate there is a substantial amount of reaction due to the increased biomass concentration compared to the loading rate.

The following three contour plots show snapshots of acetate, nitrate, and biomass at 21.0 days, slightly after the steady-state of 20.6 days for the multiplicative run and 20.3

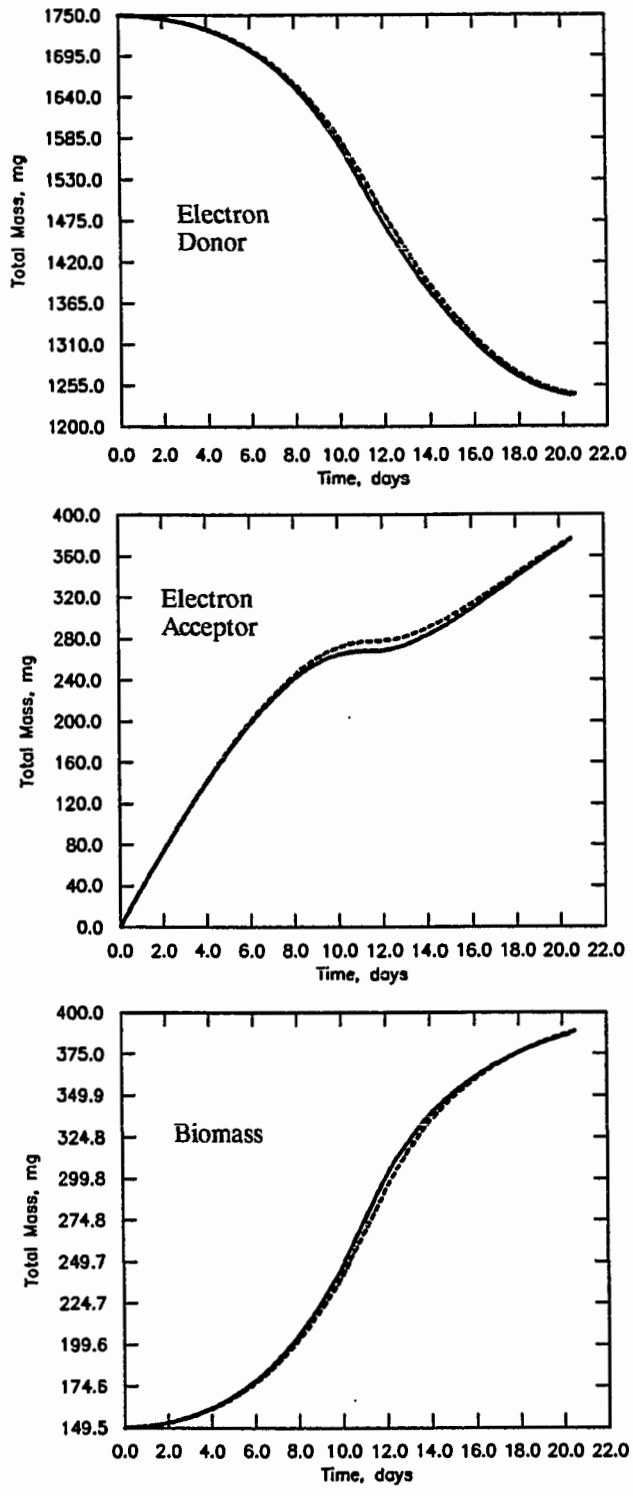


Figure 5.2 Case 1 mass curves for the electron donor, electron acceptor, and biomass. (Dashed line = Multiplicative, Solid line = Minimum-Rate)

days for the minimum–rate run. The contour plots are for the results of the M kinetic case for Case 1, because the difference between the M and MR simulations were small. Figure 5.3 shows the spatial distribution of the acetate removal at time 21.0 days into the simulation. The contour line of 4950 ppb demonstrates that a large amount of transverse dispersion took place in the simulation. The rapid depletion of electron donor close to the source is a result of the large amount of biomass that has accumulated there at steady–state. It is clear that the electron donor completely limits the kinetics close to the source because of its large removal when compared to the electron acceptor. The nitrate plume is shown in Figure 5.4. An important observation is that the electron acceptor is not the rate–limiting substrate close to the source, but is the rate–limiting substrate in the transverse direction as it penetrates the acetate plume. The protruding finger shape of the 1 ppb contour is a result of the biomass build up in a region just above the source due to the transverse spreading of the electron donor and acceptor. It is clear that the electron acceptor limits the kinetics as it spreads into the electron donor plume. In comparing the two snapshots, it is also clear that $S_A < (K_A/K_S)S_S = 0.67S_S$ in the transverse direction above $z = 0.10$ m, which confirms that the electron acceptor is rate limiting in this region. The electron acceptor is rate limiting in the transverse direction above $z = 0.10$ m, because there is not enough of it to oxidize the large continual mass of electron donor. The above inequality is false close to the source in the longitudinal direction, and the electron donor limits the kinetics, because there is excess electron acceptor available in the longitudinal direction below $z = 0.10$ m. There is virtually no overlap in the regions of limitation, i.e., there are two distinct regions of substrate limitation. Therefore, I am confident that both M and MR are compared fairly because there was complete electron donor and electron acceptor limitation at different regions in the domain.

The final contour plot is a snapshot of the biomass distribution shown in Figure 5.5. Again, the finger–shaped protrusion is evident just above the source due to the transverse spreading of the electron donor and acceptor. The biomass concentration decreases

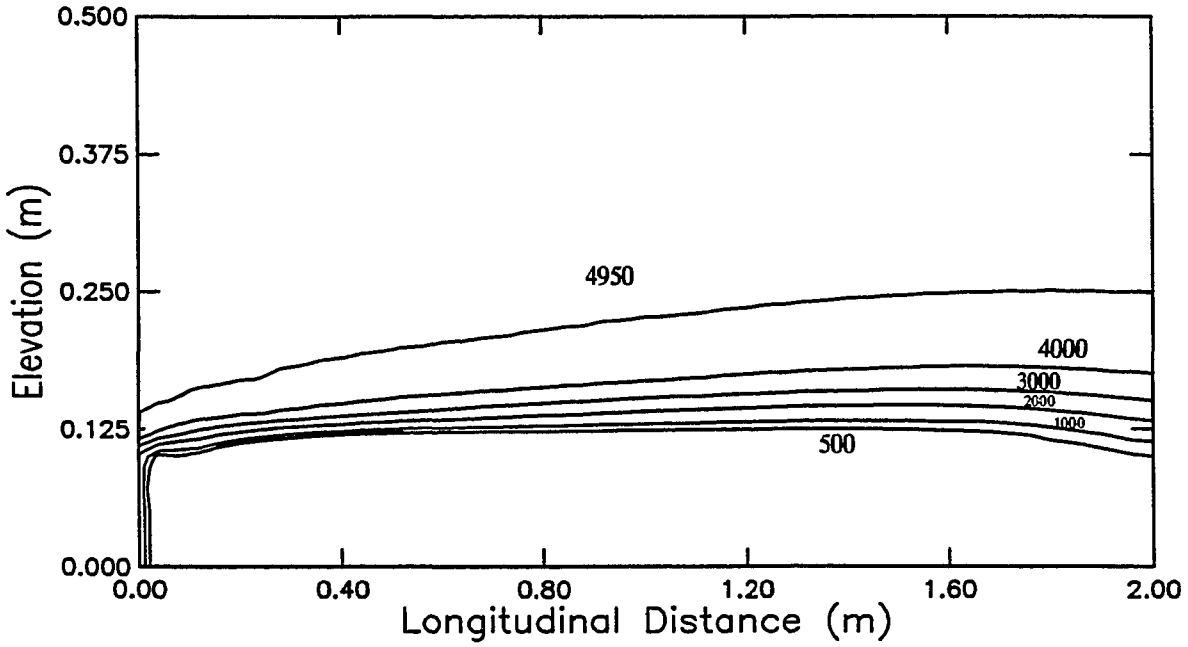


Figure 5.3 Acetate distribution of the multiplicative run at 21.0 days. Units are in μg/L.

rapidly downstream of the source and is large in its longitudinal extent. The maximum biomass concentration at the source at steady-state was 35.21 mg/L, which corresponds to 82.4 times the background concentration of 0.427 mg/L. This would correspond to an $L_f^*$ of $2.74 \times 10^{-3}$, if the same biofilm parameters, (a, $X_f$, and $D_f$), from Chapter 4 are assumed and hence the biofilm would be fully penetrated, with no external mass transport resistance. The $Da_{MAC}$ for the electron donor at the source at steady-state is 2.20, which falls between the two steady-state $Da_{MAC}$ values at the source reported in Chapter for the base case and the case of exaggerated external mass transport, i.e., 0.44 and 5.05, respectively. The biomass concentration for the simulation of this section increased by $10^{1.92}$, as opposed to $10^{2.52}$ and $10^{3.98}$ for the two cases reported in Chapter 4. Thus, when the $Da_{MAC}$ is on the order of unity, the biodegradation kinetics have become fast enough to utilize a significant amount of the incoming electron donor in the $\Delta x$ closest to the source.

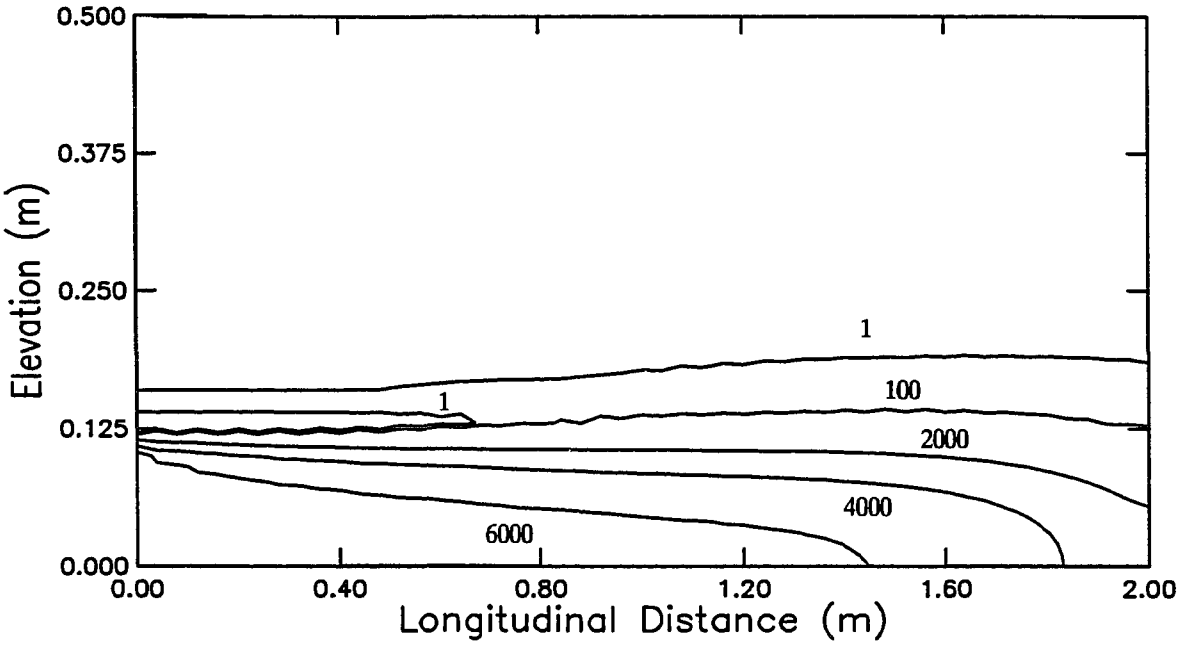


Figure 5.4 Nitrate distribution of the multiplicative run at 21.0 days. Units are in μg/L.

The main conclusion we can draw from the above simulations is that there is little difference between M and MR when the kinetics are mostly in the zero-order range. The electron acceptor limited the reaction rate at the bottom edge of the electron donor plume and the electron donor limited the reaction rate close to the source. Both the half saturation constants were small, relative to both the injection and background concentrations of both substrates, which meant that close to zero-order kinetics were predominant. Thus, as shown by the simplified reaction equations in Table 5.1, the difference in kinetic rates was small due to the approximate zero-order kinetics, which was demonstrated from the mass curve. The regions of hyperbolic and first-order reaction are examined in the next section.

## 5.4 Effects of Kinetic Parameter Variation

As previously shown in Tables 5.1 through 5.3, the differences between the multiplicative and minimum-rate Monod models depends upon the relative magnitude of

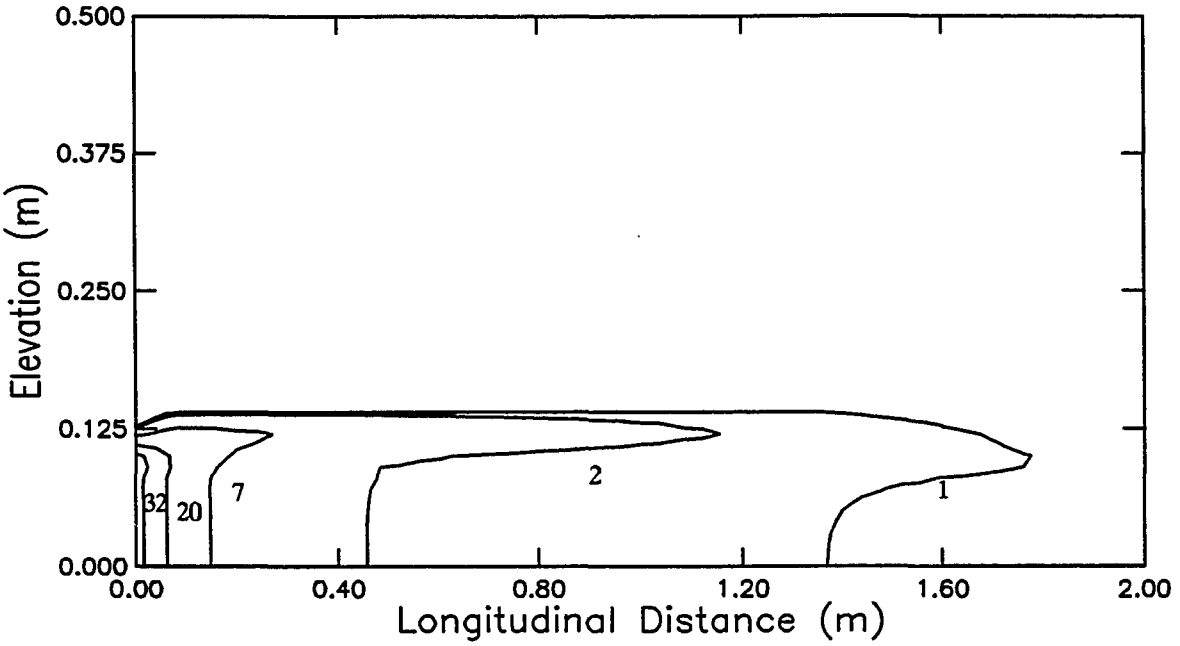


Figure 5.5. Biomass distribution of the multiplicative run at 21.0 days. Units are in mg/L.

the concentration and half-velocity constants. To more forcefully illustrate the effect of dual-limitation, the half-saturation constants of the electron donor and acceptor were varied in different ways. The K values for the test cases are reported in Table 5.5; the simulation discussed in the previous section is listed as Case 1. Also listed in Table 5.5 are the approximate kinetic relationships when the changed K values are compared to the injection and background concentration of the substrates. The purpose of varying the K values of the electron acceptor and electron donor was to establish different initial kinetic regimes to conduct numerical simulations to very the conclusions from above. Each change in initial kinetic regime is explained below.

For Case 2, the $K_S$ value of the electron donor was increased by an order of magnitude while the $K_A$ of the electron acceptor remained the same as Case 1. This variation serves to have the kinetics of the electron donor near the hyperbolic range. In Case 3, the electron acceptor's $K_A$ value was increased by an order of magnitude so that both

Table 5.5 Test Cases For Demonstrating the Effects of $K_S$ and $K_A$ Changes

| | $K_S$ | ~ Regime[1] | $K_A$ | ~ Regime[2] |
|---|---|---|---|---|
| Case 1 | 0.218 mg/L | $0^{th}$ | 0.146 mg/L | $0^{th}$ |
| Case 2 | 2.18 mg/L | $H^+$ | 0.146 mg/L | $0^{th}$ |
| Case 3 | 2.18 mg/L | H | 1.46 mg/L | H |
| Case 4 | 21.8 mg/L | $1^{st}$ | 0.146 mg/L | $0^{th}$ |
| Case 5 | 21.8 mg/L | $1^{st}$ | 14.6 mg/L | $1^{st}$ |

$^+$ H = Hyperbolic Range
1 = Based Upon Back S = 5.0 mg SOC/L
2 = Based Upon A = 10.0 mg $NO_3^-$–N/L

substrates' kinetics are in the H range. The $K_S$ value of Case 4 represents one of the extremes, first-order kinetics. The $K_A$ is the same as in Cases 1 and 3, giving zero–order for A.

Finally, Case 5 represents the extreme case, in which the kinetic expressions of the electron donor and electron acceptor are both in the first-order range. When both substrates are in the first-order region, the M and MR models should have the greatest difference. Therefore, the Case 5 M simulation is expected to show significantly less removal than any of the previous four M cases and significantly less removal than the Case 5 MR.

The results of the $K_S$ and $K_A$ variation comparisons will be conducted by examining the total mass curves of electron donor, electron acceptor, and biomass for Cases 1–5. Numerical experimentation showed that the mass curves were an excellent means by which M and MR kinetic responses could be measured, as well as illustrating the overall

transient changes in the system. The same transport problem for the Case 1 was solved with the only changes being $K_S$ and $K_A$, as noted in Table 5.5. The steady-state ($\Omega$) was again defined as a 0.01% change in the total amount of biomass in the system.

The results of the simulation for Case 2 are shown in the form of mass curves in Figure 5.6. Compared to Case 1, differences between the two curves are more noticeable, but the differences are still quite small. The differences are greatest in the period of rapid biomass growth.

There is a dramatic change in the overall kinetic behavior of the system for Case 3, shown in the series of plots in Figure 5.7. As a result of both the K values being near the hyperbolic range of the kinetic expressions, the reaction rate for M is extremely reduced when compared to the MR results. The difference between the mass curves increases throughout the simulation and is still significant at steady-state. In terms of the total mass of organic remaining in the system at steady-state, there is a 35.79 mg difference, which corresponds to a 7.78% difference. This significant difference is not surprising since the reduced form of the equations showed a substantial difference in the reaction rate in this region.

The results of the simulation with the kinetics of Case 4 are shown in Figure 5.8. Again the MR and M results differ dramatically. In addition, because of the large $K_S$, the kinetics of the electron donor are first-order, which yields a lower overall rate. Steady-state occurs at almost 90 days, almost double the time as the previous three cases. At steady-state, there was only approximately 6% removal of the total amount of organic in the system compared to an average of approximately 28% of the previous cases.

Figure 5.9 is a plot of the mass curves for Case 5. The mass curves of the electron donor and biomass show the most extreme difference between M and MR, as well as a significant reduction in the reaction rate compared to the previous four cases. There was approximately 4.80% total organic removal at steady-state (87.0 days) for MR and 0.83% removal at steady-state (43.0 days) for the M simulation. This illustrates the dramatic

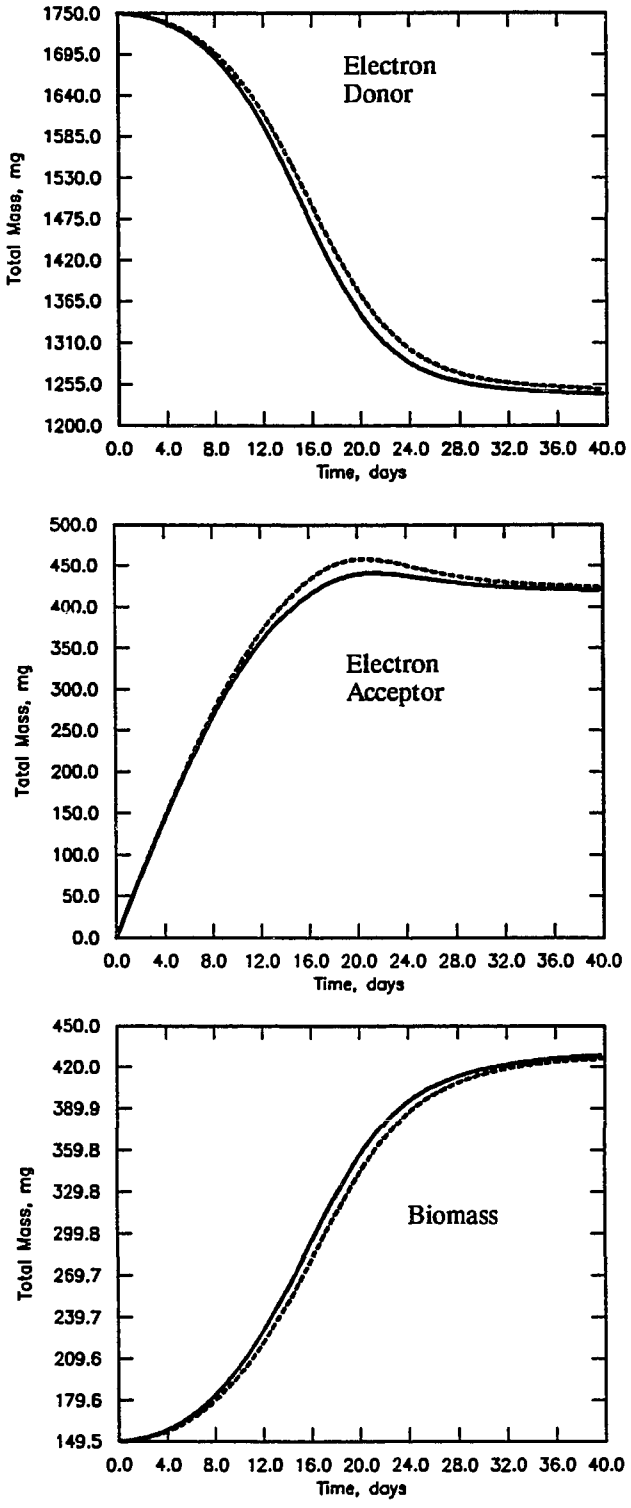


Figure 5.6 Case 2 mass curves for the electron donor, electron acceptor, and biomass.(Dashed line = Multiplicative, Solid line = Minimum-Rate)

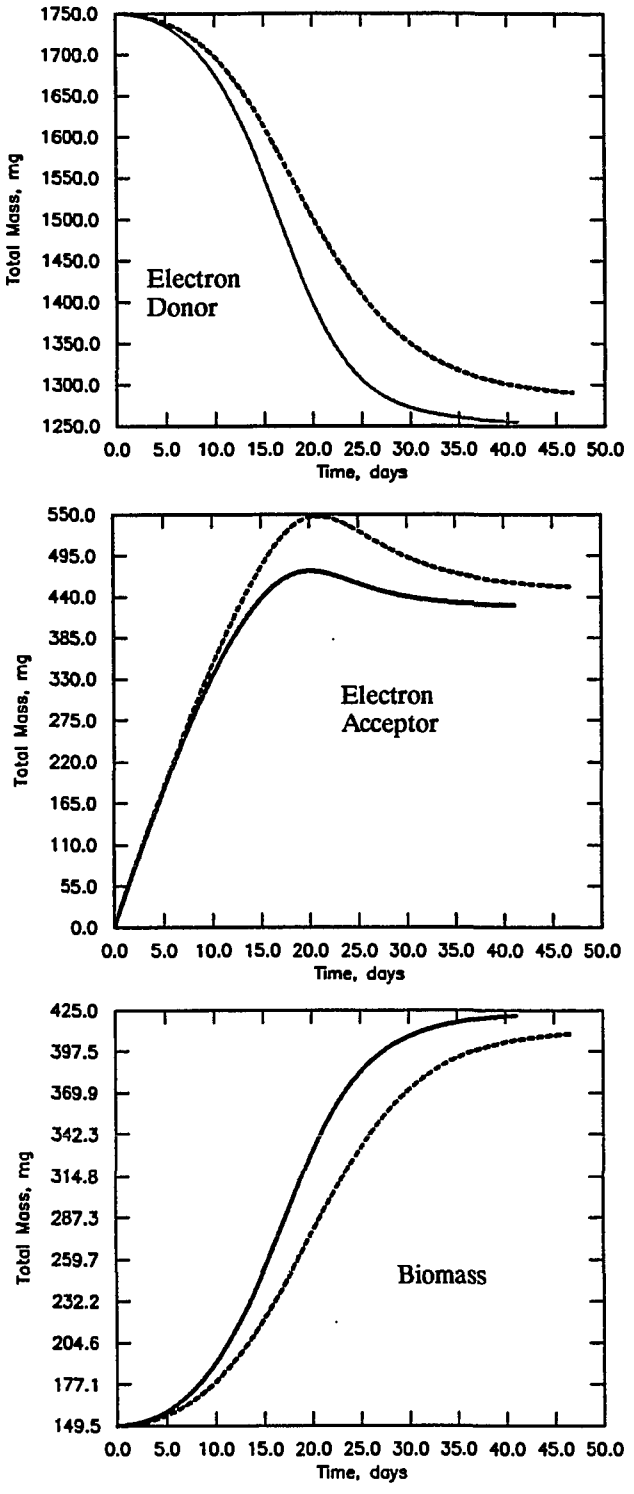


Figure 5.7 Case 3 mass curves for the electron donor, electron acceptor, and biomass. (Dashed line = Multiplicative, Solid line = Minimum-Rate)

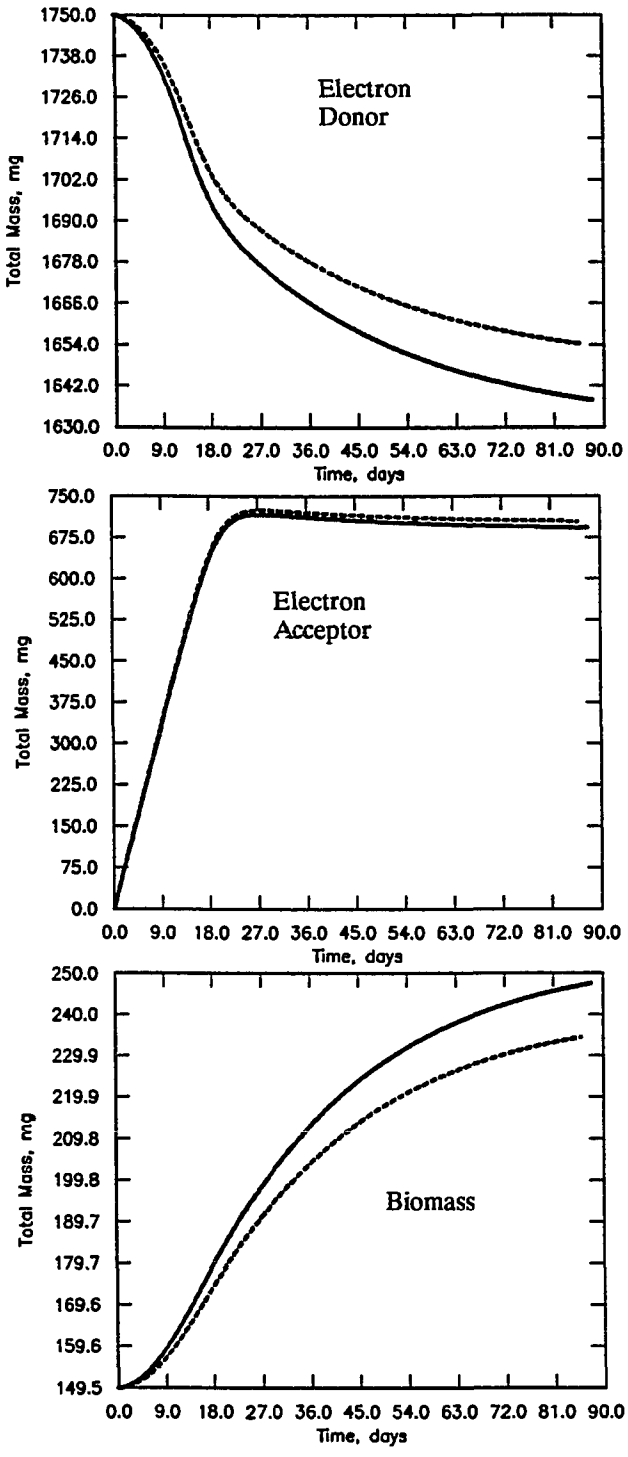


Figure 5.8 Case 4 mass curves for the electron donor, electron acceptor, and biomass. (Dashed line = Multiplicative, Solid line = Minimum-Rate)

difference anticipated from the simplifications of MR and M for first-order kinetics in Table 5.2. When the organic removals of Case 5 are compared to the removal of Case 4, there was approximately 75% of the removal for MR and only 15% of the removal of M for Case 5. The reduced overall reaction rate is also reflected by the time to reach steady-state. The growth came to a maximum at 40.3 days for M and 87.0 days for MR; it took more than twice as long for MR to reach steady-state because of its lower reaction rate. There was far less organic removal as a result of the lowest overall reaction rate of both the electron donor and electron acceptor. As a result, the overall utilization of the electron acceptor is small, as shown in Figure 5.9. Further discussion of the significance of Case 5 is presented in the following paragraphs.

The results of the numerical simulations with the different kinetics are summarized in Table 5.6. The time to reach steady-state and corresponding total removal of electron donor at steady-state are listed for all five cases. The total removal is defined as the amount of electron-donor in the domain at the defined steady state compared to the initial amount of electron donor in the domain. For Case 1, there is little difference in the results because both M and MR were in the zero-order range. Case 2 took longer to reach steady-state, though the time to reach this point for MR and M were fairly close with the removal of MR being slightly greater than M. A dramatic difference in terms of the total organic mass removal difference was shown in Case 3. There was substantially more removal at steady-state for the MR run compared to the M run, due to both MR and M being in the hyperbolic range initially. It took the M run 5.6 days longer to reach steady-state than the MR run. Case 4 had an even more dramatic overall kinetic effect, having nearly five times lower total removal than in the previous three cases. As explained previously, this was a result of the low first-order rate constant for the reaction rate of the electron donor. It also took more than twice as long to reach steady-state than in the previous three cases. At steady-state, there was approximately a 1% difference in the total amount of organic removal, where the MR run had the greater removal. The most

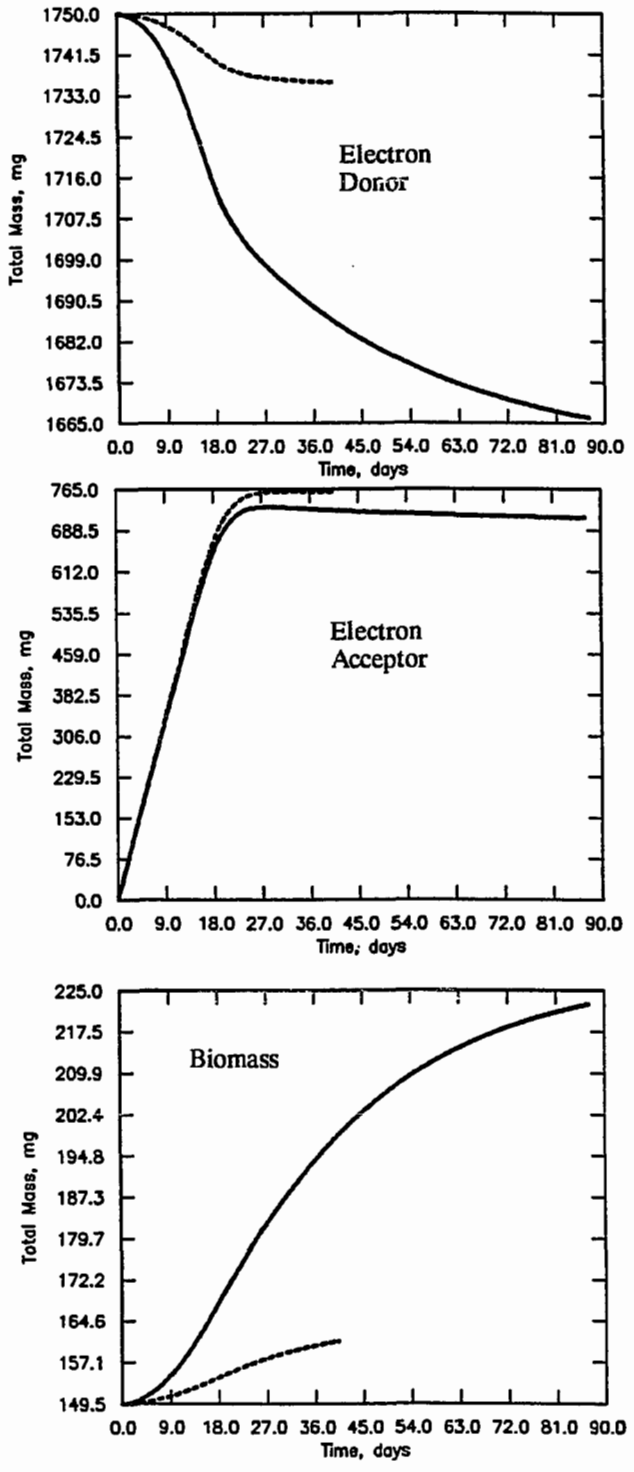


Figure 5.9 Case 5 mass curves for the electron donor, electron acceptor, and biomass. (Dashed line = Multiplicative, Solid line = Minimum-Rate)

extreme difference was in Case 5, where both the reaction rates were close to first–order. The most significant results of MR and M both being in the first order were the extremely low removal they gave and the large difference between them. The MR run had approximately six times lower removal than Cases 1–3 and M approximately 35 times lower than Cases 1–3. When compared to each other, the MR case gave 5.8 times the removal of M. That far exceeds the differences in any of the previous case, even its closet competitor, Case 4, where MR gave only 1.17 times the removal of M.

Table 5.6 Percent Total Organic Removal at Steady–State for Cases 1–5.

| | MR Organic Removal* | Steady–State (days) | M Organic Removal* | Steady–State (days) |
|---|---|---|---|---|
| Case 1 | 29.02 | 20.3 | 29.01 | 20.6 |
| Case 2 | 29.00 | 39.7 | 28.63 | 39.8 |
| Case 3 | 28.31 | 41.1 | 26.27 | 46.7 |
| Case 4 | 6.41 | 87.8 | 5.48 | 86.0 |
| Case 5 | 4.80 | 87.0 | 0.83 | 40.3 |

* M = Multiplicative kinetics; MR = Minimum–Rate Kinetics

## 5.5 Summary and Conclusions

The main goal of this chapter was to examine the implications of using minimum–rate versus multiplicative Monod kinetics in a system of coupled electron acceptor and electron donor transport and biomass growth. The first task was a critical evaluation of these different kinetic descriptions, which involved reducing the kinetics to zero– and first–order. Although the zero–order kinetic expressions reduced to the same mathematical form, the first–order reduction showed a large difference between MR and M. When the concentration of electron donor and electron acceptor was set equal to their

corresponding $K_S$ and $K_A$ values, the substrate utilization rate and biomass growth rate for M was exactly one–half that for MR.

Based upon analysis of the reduced kinetic expressions, five different two–dimensional numerical experiments were designed to examine regions where M and MR differed. The experimental cases were generated by varying $K_S$ and $K_A$ relative to the background and injection concentrations of electron donor and electron acceptor. The results of the experiments can be summarized with the following conclusions.

1. When the K values are low enough that concentrations are in the zero–order range through most of the domain, MR and M kinetic expressions have a negligible difference.
2. The absolute difference between the MR and M expressions was significant when both K values were on the order of the concentration of the electron donor and electron acceptor. A maximum difference, in terms of the total organic mass removed, was 30% during an accelerated growth period of the transport simulation described within.
3. When both substrates were in the first–order regime, the difference between the M and MR was the greatest. At steady–state, the MR kinetics gave approximately 5.8 times more removal of the electron donor than did M. Both the removals were significantly smaller than the other cases. Thus, M and MR differ most significantly when both substrates are in the first–order range, with the differences quantified by the results of the numerical simulations.
4. When one substrate was in the first–order regime and the other was in the zero–order regime, the difference between M and MR was moderate.
5. The numerical experiments that were conducted corroborate the conclusions that were determined from the simplifications of the kinetic expressions of M and MR.

# 6. INVESTIGATION OF COUPLED TRANSPORT PROCESSES AND BIODEGRADATION KINETICS IN STRATIFIED POROUS MEDIA

## 6.1 Introduction

Hetereogeneity at the field scale plays a major role in determining the pathways of groundwater flow and contaminant transport. By controlling the mixing between water containing different amounts of electron donor and electron acceptor, field scale hetereogeneity may have a major influence on biodegradation. Although numerous types and scales of hetereogeneity can exist, stratification is a simple type that is of practical importance because it is commonly encountered at field sites.

The overall objective of this chapter is to examine the influence of stratification upon coupled transport and biodegradation processes. Based upon field results, Patrick and Barker (1988) speculated that varying layers of hydraulic conductivity play an important role in biodegradation, because the layering controls mixing of the electron acceptor within the contaminant plume. As discussed in Chapter 2, the only reported modeling study of combined transport and biodegradation processes in a stratified system is by Chiang et al. (1989). The stratified system of their study was extremely complicated, which made identification of the controlling processes difficult.

To simplify the problem so that the interaction between stratification and biodegradation can be discerned, Monod kinetics are used here, because the results of Chapter 4 showed that the difference between Monod and biofilm kinetics is small for most groundwater situations. The following two specific objectives are considered in this chapter:

1. Contrast single-substrate removal and biomass development for a two-layer stratified system with an "equivalent" homogeneous system.
2. Examine the interaction among stratification, longitudinal and transverse dispersion,

and initial biomass concentration on electron donor and electron acceptor transport and biomass development for the case of multiplicative Monod biodegradation kinetics.

## 6.2 Single Substrate Limitation in Two Layers with Comparison to a Homogeneous System

The domain shown in Figure 6.1 is used to examine the effect of stratified layers when only one substrate limits the kinetics. The rate–limiting substrate is the electron donor, acetate, used in the previous two chapters. The biological kinetic parameters are those used in the example problem of Chapter 4 and are listed again in Figure 6.1. The velocity is 1.0 m/day in the top layer, as used in the numerical experiments of Chapter 4, and 0.1 m/day in the lower layer, as used in the numerical experiments of Chapter 5. These horizontal velocities are typical of those found in layered sandy aquifers under natural gradient conditions (Sudicky, 1983). The velocity contrast between the two layers is 10; this difference is large enough to emphasize the important phenomena involved in a stratified system, while being realistic for field situations. The influent substrate concentration is 1.0 mg/L across the influent boundary. This corresponds to a loading rate of 87.5 mg S/day for the top layer and 8.75 mg S/day for the bottom layer, which amounts to a total loading to the system of 96.25 mg S/day. Single–substrate limitation is assumed to follow a single–Monod kinetic expression.

The grid spacings in the longitudinal and transverse direction and the time–step for transport are also shown in Figure 6.1. These discretization parameters were selected to satisfy the more stringent PD criteria in the higher velocity layer (top); the same longitudinal and transverse grid is implemented throughout the entire domain. The resulting Peclet and Courant numbers for the lower layer are also shown in Figure 6.1. The spacing parameters $\rho_1$ and $\rho_2$ for the lower layer have small values compared to those of the top layer; however, they still satisfy the PD accuracy and convergence criteria. The aspect ratio, defined as $\rho_1/\rho_2$, should be equal to one to obtain the optimum theoretical accuracy of the PD scheme. Nevertheless, Frind (1982) demonstrated that the decoupled

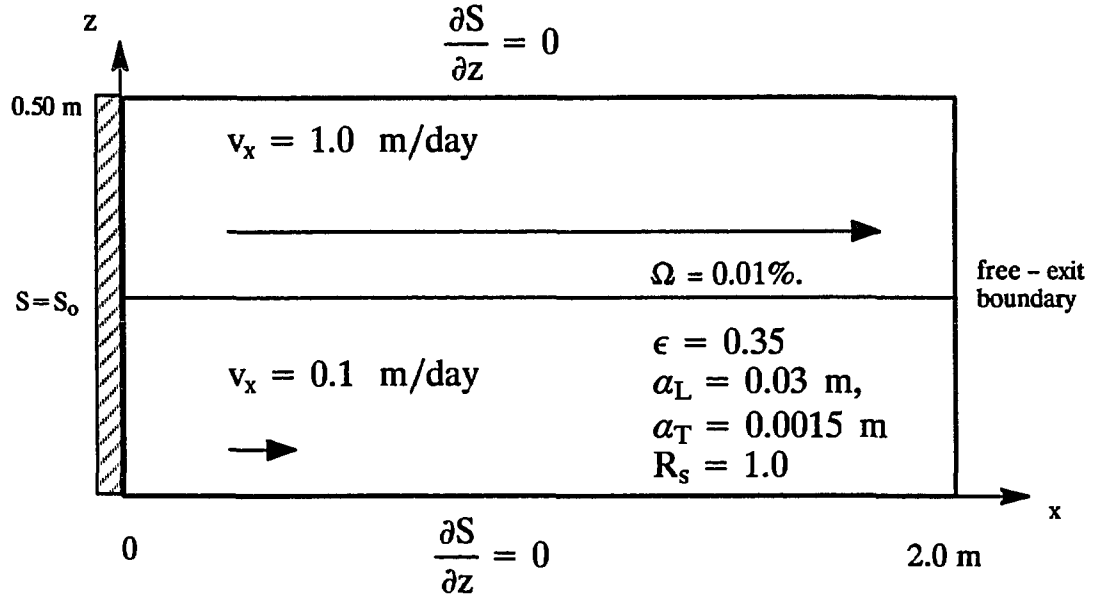


Biological Parameters

$q_m$=0.42 mg SOC/mg cell-day
$K_S$=0.218 mg/L

Y=0.678 mg cells/mg SOC
b=0.07 day$^{-1}$
$M_{To}$=10$^6$cells/g=0.427 mg/L

| Top Layer | Constant | Bottom layer |
|---|---|---|
| Pe = 0.886 | $\Delta x$ = 0.027m | Pe = 0.858 |
| Co = 0.413 | $\Delta z$ = 0.01923m | Co = 0.04125 |
| $\rho_1$ = 0.466 | $\Delta t$ = 0.011 day | $\rho_1$ = 0.0481 |
| $\rho_2$ = 0.0478 | Total Nodes = 2052 | $\rho_2$ = 0.00764 |
| $\rho_1/\rho_2$=9.75 | Runge - Kutta Steps = 50 | $\rho_1/\rho_2$=6.29 |

Figure 6.1. Domain and physical, biological, and numerical parameters used in the stratified simulations.

nature of PD can handle problems with aspect ratios as high as 12.5 without severe loss of accuracy. The aspect ratio was 9.75 for the top layer and 6.29 for the bottom layer. To test the accuracy of the reaction computations, the number of Runge–Kutta steps was increased from the initial number of 50 to 75 with no resulting improvement in the accuracy of the results. The accuracy was determined by comparing the point–wise concentration values of organic compound and biomass at selected times throughout the

simulation. The comparison of numerical values at each computational node demonstrated an accuracy to at least five significant figures. Therefore, 50 Runge–Kutta steps were used for the simulations.

The higher mass loading in the more permeable layer of the stratified case will result in greater biomass development and electron donor removal than in the less permeable layer. Therefore, it is interesting to examine the removal that would occur in a hydraulically equivalent homogeneous system with a velocity of 0.55 m/day, which is the arithmetic average of the velocities in each layer. Thus the total mass flux into the homogeneous system is the same as the heterogeneous system. The simulation for the homogeneous system was conducted using the same biological parameters as in the previous case, but with a uniform velocity of 0.55 m/day. The simulation was computed using the same 2.0 m x 0.5 m domain as in the previous case, with the velocity in the vertical direction representing the depth–averaged value. The longitudinal grid–spacing remained the same, 0.026m, while the time step of transport was changed to 0.022 days. These values result in an updated Peclet number of 0.886 and a Courant number of 0.454.

In order to gain an understanding of the transient behavior involved in the stratified experiment, snapshots of the rate–limiting substrate at four selected times, 1.65, 4.95, 6.60, and 8.25 days, are shown. These snapshots are shown in Figure 6.2 to illustrate the response of the substrate plume to biomass development. The first snapshot shows the electron donor at 1.65 days and indicates a mainly nonreactive electron donor distribution with evidence of a small amount of biological reaction (i.e. the contour lines are approximately located at positions corresponding to nonreactive transport; for example the 500 ppb contour in the fast layer is located at 1.5 m, as opposed to 1.65 m for the case with no reaction). The penetration of substrate into the slow layer is evidence of transverse dispersion of the electron donor from the fast to the slow layer. The next snapshot, at 4.95 days, reveals significant retreat of the contour lines in the fast layer back toward the source as a result of increased biomass growth in this region. The 900 ppm contour line shifts

from 0.5 m at time 1.65 days to 0.36 m at 4.95 days in the fast layer. The same behavior is not evident in the slow layer at this point. In fact contours of the electron donor are moving further into the slow layer from 1.65 to 4.95 days, which is evidence of nonreactive or weakly reactive transport. The contour plot at 6.60 days indicates, by the comparatively large number of contour lines that have moved back towards the source, that the response of the faster velocity layer to biomass growth is much greater than in the slow layer. The loading rate is ten times higher in the upper layer, which allows for much faster growth of biomass and subsequent removal of substrate. There is still evidence of large transverse dispersion from the upper to the lower layer as indicated by the mass of electron donor that has migrated from the fast layer into the slow layer. In the final snapshot, at 8.25 days, all the contour lines in the slow layer, as well as those in the fast layer, have moved back toward the source.

When comparing the snapshot at 8.25 days to the earlier ones, we see that the substrate gradient in the transverse direction is reduced substantially near the interface of the two layers. This results in a reduction in the amount of transverse dispersion from the upper to the lower layer as a result of the increased amount of biomass in the top layer. The effect of the stratification is much more pronounced at the early times, when the plume behaves conservatively and before significant biomass growth has occurred. The substrate gradient close to the source has increased dramatically in the longitudinal direction as a result of the localized increase in biomass concentration. The reduced transverse gradient and increased longitudinal gradient are a result of the simultaneous retreat of the concentration profile in both layers. This retreat restricts the amount of substrate able to disperse transversely from the fast to the slow layer, causing a reduction in the inter-layer mass transfer. However, the retreat concentrates biological activity and creates the large longitudinal gradient.

A detailed comparison of the stratified and homogeneous results is considered by examining snapshots of substrate and biomass at 9.90 and 14.85 days. Figure 6.3 is

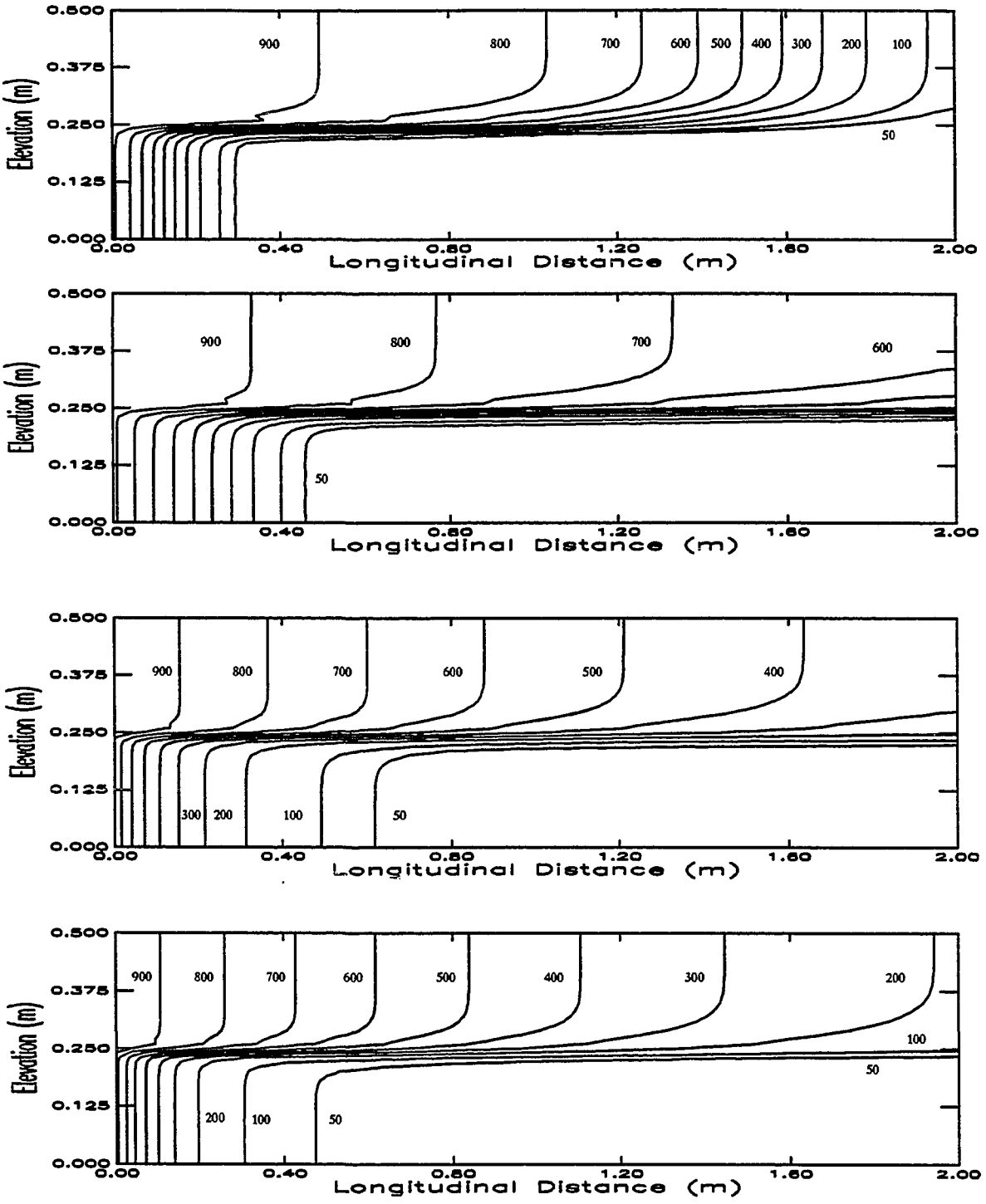


Figure 6.2. Time history of the substrate plume development. Snapshots of the plume at 1.65, 4.95, 6.60, and 8.25 days (top to bottom). The concentration values are in ppb.

composed of four contour plots of the substrate and biomass distributions at 9.90 days and is arranged so that the stratified and homogeneous results alternate. Using the same isoconcentration lines allows easy interpretation. For the stratified case, there is further retreat of the organic contour lines back toward the source when the snapshot is compared to the earlier one at day 8.25 in Figure 6.2. Continued reduction of transverse dispersion from the upper to the lower layers is also observed. Comparing the numerical average of isoconcentration lines locations in the fast and slow layers of the stratified case to homogeneous case demonstrates that lines of equal concentration for the homogeneous case lie exactly between those in the upper and lower layers of the stratified case. This was done by comparing the average of the position of each isoconcentration line in the fast and slow layers and with the position of the corresponding isoconcentration line in the homogeneous case. The biomass distributions of the stratified and homogeneous cases are shown as the last two snapshots in Figure 6.3. Similar trends are observed here as in the substrate distribution. Again, the numerical average of the longitudinal position of contour lines of the stratified case lie exactly between in the homogeneous case.

Figure 6.4 has the same series of plots as in Figure 6.3, except at 14.85 days as opposed to 9.90 days. A comparison of the substrate contours reveals that biological activity is much more intense near the source at 14.85 days than at 9.90 days. Removal of substrate near the source makes the amount of transverse dispersion much smaller as indicated by the smaller transverse gradient at the interface. In addition, the position of the homogeneous contours and the average of the upper and lower layer of the stratified system coincide. A similar behavior is found when the biomass distributions of the stratified and homogeneous cases are compared. The full retreat of the plume is observed when the snapshot of the stratified system's substrate distribution is compared with the snapshot at time 9.90 days in Figure 6.3. The steady-state of the homogeneous case was reached at 49.73 days for the convergence criteria ($\Omega$) of 0.01% used in the previous case, compared to 40.79 days in the stratified system. It took 8.49 days longer for the

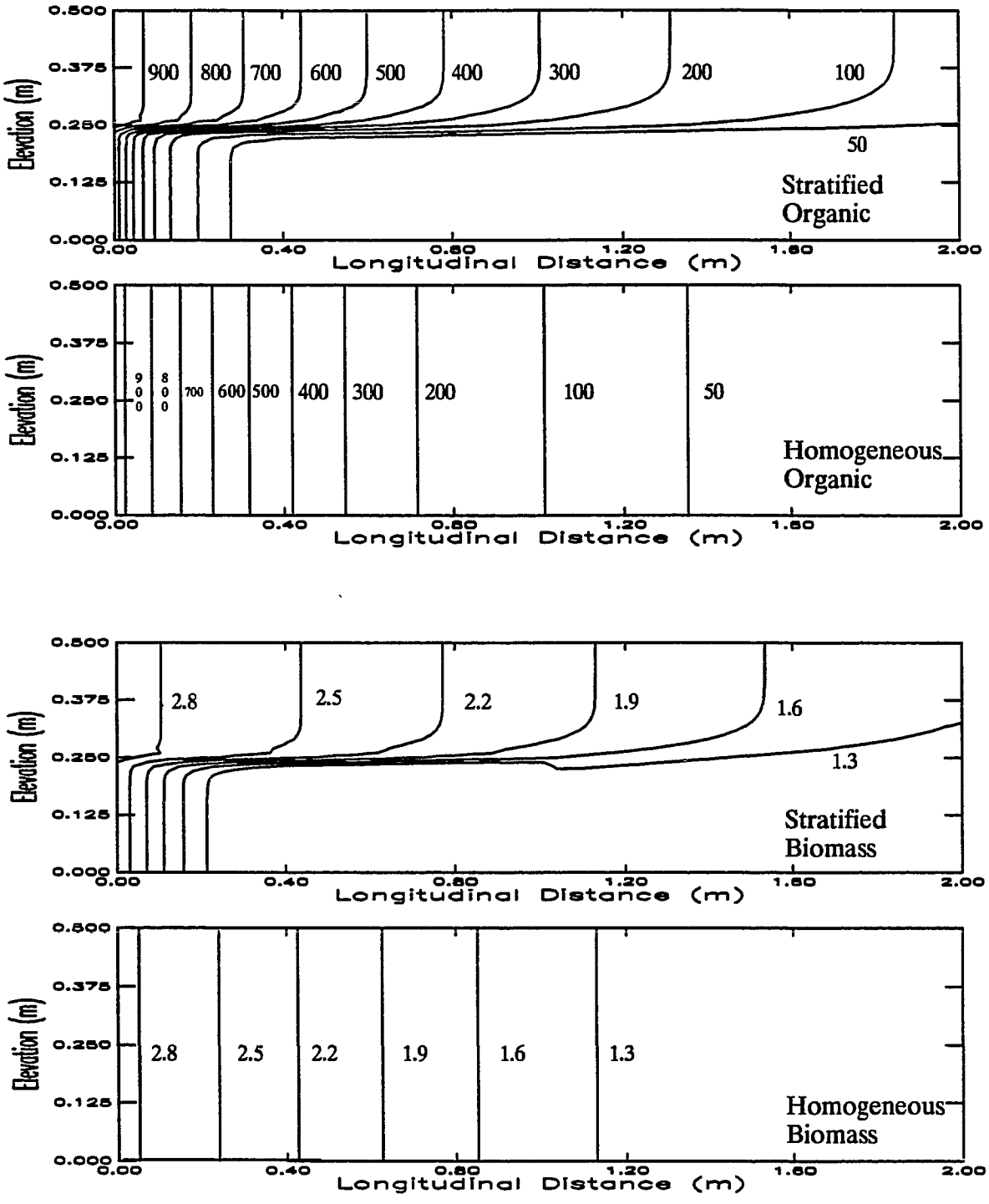


Figure 6.3. Contour plots of the organic compound (μg/L) and biomass (mg/L) at 9.90 days comparing the stratified and vertically averaged systems.

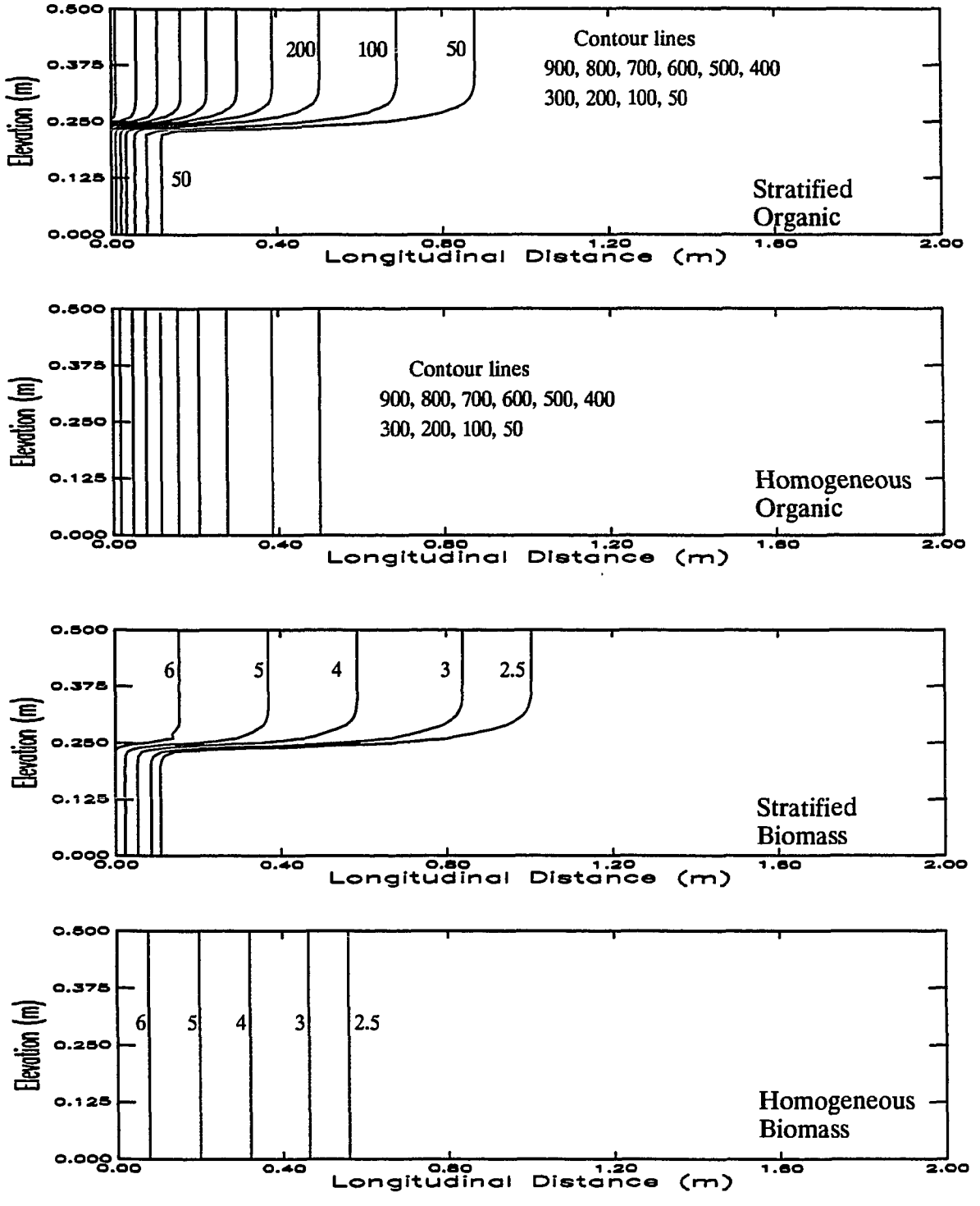


Figure 6.4. Contour plots of the organic compound (μg/L) and biomass (mg/L) at 14.85 days comparing the stratified and vertically averaged systems.

homogeneous run to reach steady–state than the stratified due to the smaller amount of biomass in the lower layer of the stratified system. Although not shown, figures comparing the stratified and homogeneous systems developed closer to the steady–state (40 days) revealed that the electron donor, as well as the biomass in the homogeneous system, equaled exactly the vertical average of the stratified system. Thus, the homogeneous system is effectively equivalent to the vertical average of the stratified system at the defined steady–state.

The comparison of the results of the homogeneous and stratified systems is now presented in the form of mass curves of the electron donor and biomass. The mass curves of organic and biomass represent general system behavior, while contour plots of the spatial distribution of both quantities and allows examination of details. The solid line in Figure 6.5 shows the total amount of organic in the stratified system throughout the simulation, and the dashed line is that of the equivalent homogeneous system. The biomass growth becomes sufficient to affect the total organic mass in the system at 3.81 days (maximum organic mass = 211.1 mg) for the homogeneous case, as opposed to 2.76 days (maximum organic mass = 157.1 mg) for the stratified case. From this peak until steady–state, there was a continual decrease of the total amount of organic in the system. The difference between the two curves from day three to ten is due mainly to the substrate mass in the faster moving layer that has left the system boundary of two meters. If the grid were longer, the curves would be be similar. Therefore, the total substrate mass curves cannot be critically compared during this time period. Figure 6.6 shows the total amount of biomass in the homogeneous and stratified systems throughout the simulation. The total biomass of the homogeneous case is always greater than the stratified case because of the small amount of biomass that develops in the bottom layer of the stratified system.

The key finding of the above comparison is that the effect of stratification appears to be greatest during rapid biomass growth. The biomass grows faster in the more permeable upper layer, causing more organic removal during this time. Such a phenomena could

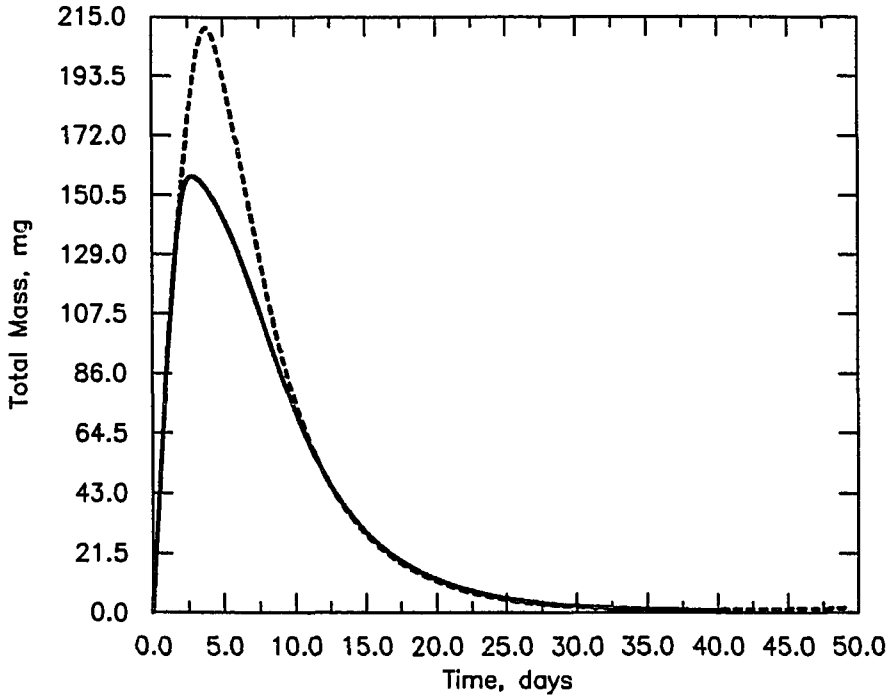


Figure 6.5. Total mass of organic in the stratified system (solid line) and the homogeneous system (dashed line).

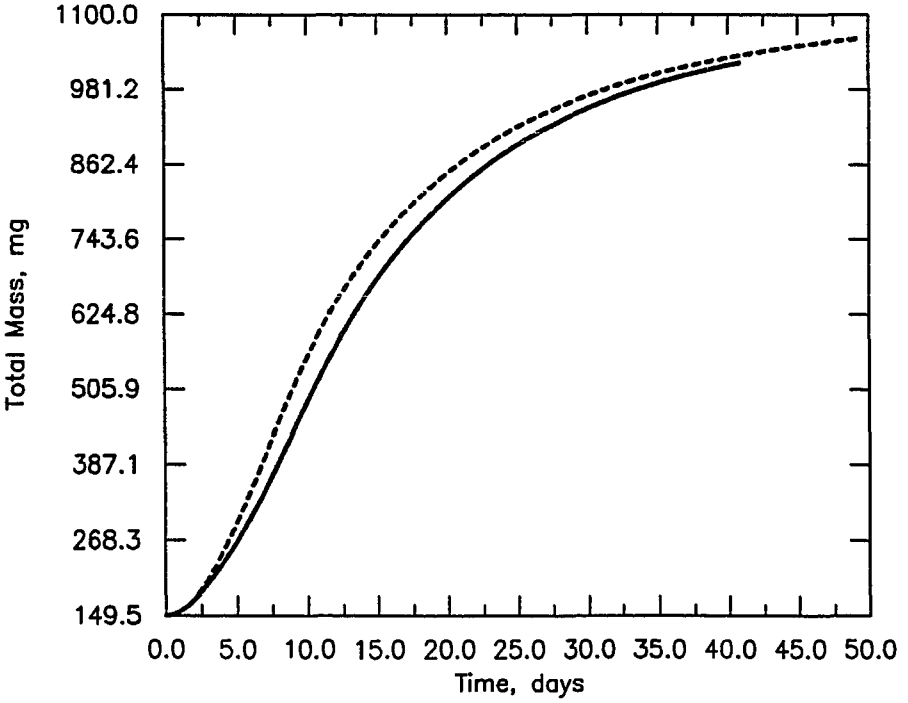


Figure 6.6. Total mass of biomass in the stratified system (solid line) and the homogeneous system (dashed line).

have an impact on the application of an bioremediation scheme. It may be necessary to use more injection wells for addition of rate–limiting substrate in the slow–moving layer to spread out the zone of biological activity. As both the systems approached steady–state, the effect of stratification became less in terms of the total removal of organic. Therefore, at steady–state, the stratified system can be modelled as an equivalent homogeneous system for all practical purposes. But for transient behavior, the effect of stratification can have a substantial effect.

## 6.3 Multiple Substrate Systems with Electron–Acceptor Injection

The general goal of this section to examine some of the controlling transport phenomena of electron donor and electron acceptor and subsequent biomass development under dual–substrate limitation in a stratified system. These phenomena include longitudinal and transverse dispersion, initial biomass concentration, and system boundary conditions. Some of these phenomena have been studied by various researchers as reported in the literature review of Chapter 2. Each phenomenon is discussed in detail in the following sections and related to the findings and inadequacies of previous research. Coupled electron donor, electron acceptor, and biomass systems are examined to quantify their interaction in a stratified regime as a function of the aforementioned variables.

### 6.3.1 Effects of Transverse and Longitudinal Dispersion

There have been no studies to date that focus upon the effect of dispersion upon biological transport in a stratified aquifer. Chiang et al. (1989) examined a bio–reactive transport problem with longitudinal and transverse dispersion in stratified porous media; however, they did not examine the relative impact of changes in either longitudinal or transverse dispersion. The specific goal of this section is to quantify the actual differences in the amount of biodegradation that occur as a result of changes in dispersion for a stratified porous media. Four different cases are analyzed and compared in a two–layer transport problem that is analogous to that shown in Figure 6.1. The velocity in the upper

layer is 1.0 m/day, and the velocity in the lower layer is 0.10 m/day. In the simulation to follow, both the electron donor and electron acceptor are assumed to have a molecular diffusion coefficient of 1.07 $cm^2$/day, the same as the assumption that was made in Chapter 5. In addition, the electron donor and electron acceptor have the same $\alpha_L$ and $\alpha_T$.

First, the transverse dispersion effects are examined by comparing a standard base case simulation with $\alpha_L/\alpha_T$ equal to 20 to two other runs where $\alpha_L/\alpha_T$ was equal to 5.0 and 100, respectively; in all runs a constant value of $\alpha_L$ equal to 0.030m is used. In the final case, the longitudinal dispersive process is examined by raising $\alpha_L$ to 0.30m, while using the base case value for $\alpha_T$ of 0.0015m, which yields an $\alpha_L/\alpha_T$ ratio of 200.0. Table 6.1 summarizes the $\alpha_L$ and $\alpha_T$ values used in the simulations and shows the ratio of transverse and longitudinal mechanical dispersion to molecular diffusion. The ratio of transverse dispersion to molecular diffusion ranges from a low of 0.28 to a high of 56.1; obviously, for the low range value, molecular diffusion dominates transverse mechanical dispersion. The ratio of longitudinal dispersion to molecular diffusion ranges from 28.0 to 2804; therefore, longitudinal mechanical dispersion always dominates molecular diffusion.

Table 6.1 Ratio of Mechanical Dispersion to Molecular Dispersion for the Four Test Cases

| Case | $\alpha_L$(m) | $\alpha_T$(m) | Layer | $\alpha_L v/D_m$ | $\alpha_T v/D_m$ |
|---|---|---|---|---|---|
| Base | 0.03 | 0.0015 | Top | 280.4 | 14.0 |
| | | | Bottom | 28.04 | 1.4 |
| $>\alpha_T$ | 0.03 | 0.006 | Top | 280.4 | 56.1 |
| | | | Bottom | 28.04 | 5.6 |
| $<\alpha_T$ | 0.03 | 0.0003 | Top | 280.4 | 2.8 |
| | | | Bottom | 28.04 | 0.28 |
| $>\alpha_L$ | 0.3 | 0.0015 | Top | 2804 | 14.0 |
| | | | Bottom | 280.4 | 1.4 |

The stratified system and biological parameters shown in Figure 6.7 are used as the basis of the comparison. The contamination scenario is a situation where a background

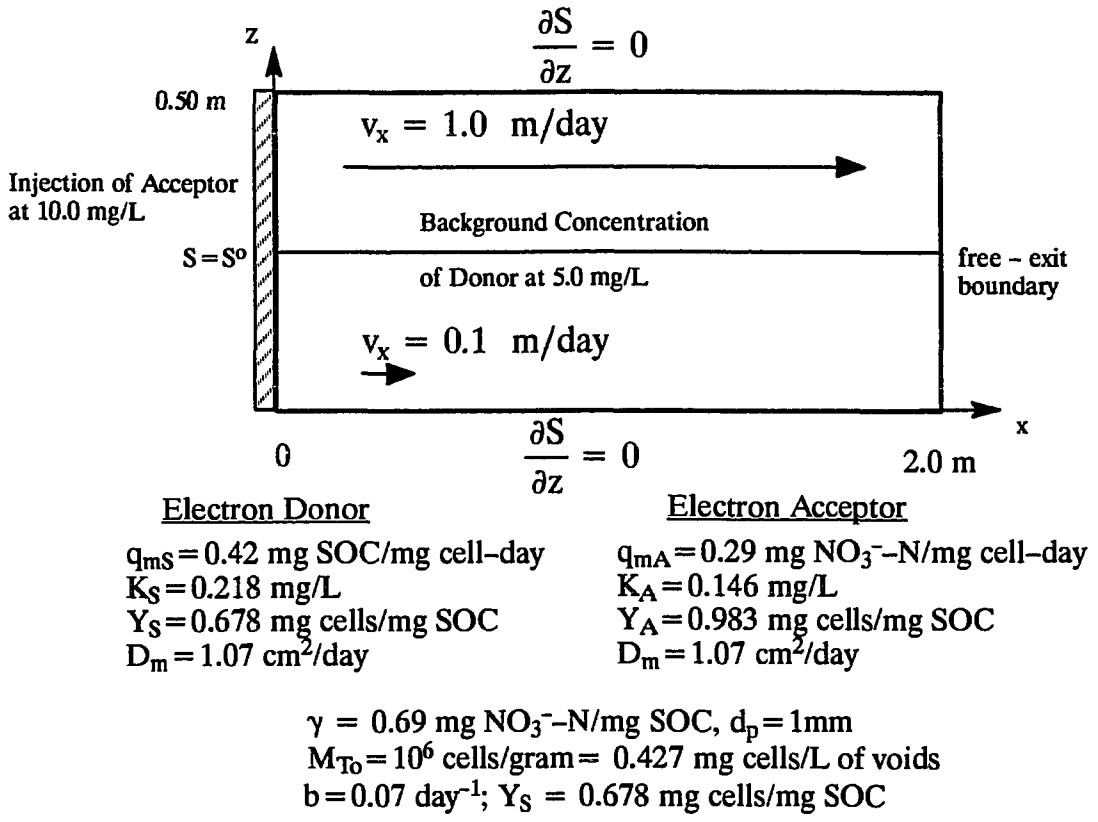


Figure 6.7. Electron donor and electron acceptor kinetic parameters and schematic diagram for the base case simulation.

concentration of electron donor is in the system initially and a continuous source of electron acceptor is supplied uniformly across the upstream boundary of the domain to stimulate the indigenous bacteria. It is assumed there is no supply of electron donor entering the system through the upstream face. As an example of a field scenario where these conditions may be applicable, consider the situation shown in Figure 6.8, where the exact plume location is known, and contamination has been discovered between two field observation wells (wells 2 and 3). Also, no electron donor is detected upstream of the monitoring well 2 at well 1. The objective is to remove the electron donor, in this case the contaminant. This will be accomplished by input of electron acceptor at the upstream well, well 2.

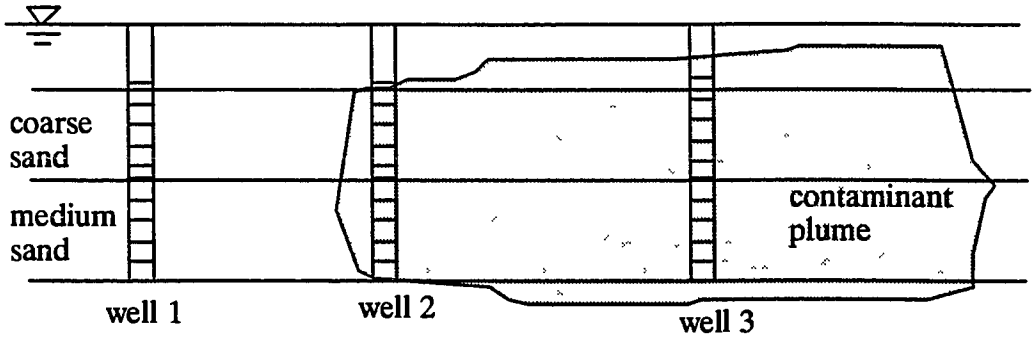


Figure 6.8 Hypothetical contaminant scenario for the numerical experiments of longitudinal and transverse dispersion with a background concentration of electron donor.

Table 6.2 is a summary of all the important PD criteria used for the simulations. The same grid spacing is used for the simulation with larger transverse dispersion because the PD criteria are still satisfied, as shown in Table 6.2. The case of smaller transverse dispersion is more complicated because the $\rho_1/\rho_2$ criterion is violated for the base case transverse grid spacing, i.e. $\rho_1/\rho_2$ is 38.49 in the upper layer. Recall that Frind (1982) found that values of $\rho_1/\rho_2$ up to 12.5 gave the same result as analytical solution in two–dimensions. As a result, the transverse grid spacing was lowered to 0.011 m to yield a more reasonable value of $\rho_1/\rho_2$ of 12.29 in the top layer. The final case of increased longitudinal dispersion yielded a totally new set of longitudinal and transverse grid spacings, as well as a new time step. For this case, the grid spacing and time step were relaxed significantly. The grid spacing in the longitudinal direction was increased 5.4 times and in the transverse direction 1.44 times. The time step was increased to 0.020 days. The combination of these values and their corresponding PD criteria values are summarized in Table 6.2.

The previous paragraphs describe the problem definition used to examine the effect of longitudinal and transverse dispersion. The results of the numerical experiments are presented in Figure 6.9, which shows the total amount of electron donor in the system from time zero to a defined stopping point. The stopping point was defined as less than a 0.001% change in the total biomass in the system. This was necessary because the biomass

Table 6.2 Comparison of Discretization Criteria for the Four Test Cases.

| Case | Layer | Δx(m) | Δz(m) | Δt(days) | Pe | Co | $\rho_1$ | $\rho_2$ | $\rho_1/\rho_2$ |
|---|---|---|---|---|---|---|---|---|---|
| Base | Top | .026 | 0.01923 | 0.011 | .886 | .413 | .466 | .0478 | 9.75 |
| | Bottom | | | | .858 | .0481 | .0481 | .00764 | 6.29 |
| $>\alpha_T$ | Top | .026 | 0.01923 | 0.011 | .886 | .413 | .466 | .1817 | 2.56 |
| | Bottom | | | | .858 | .0481 | .0481 | .0210 | 2.29 |
| $<\alpha_T$ | Top | .026 | 0.01087 | 0.011 | .886 | .413 | .466 | .0379 | 12.29 |
| | Bottom | | | | .858 | .0481 | .0481 | .0129 | 3.72 |
| $>\alpha_L$ | Top | .143 | 0.0277 | 0.020 | .476 | .140 | .294 | .0417 | 7.06 |
| | Bottom | | | | .475 | .014 | .0294 | .0066 | 4.41 |

will grow to a maximum, and then, as the electron donor eventually advects out of the system, will decay down to background levels. To interpret the simulations in terms of the amount of biodegradation that actually took place, the nonreactive curve also is plotted. Comparing the base case curve to the nonreactive curve shows that a significant amount of biodegradation took place. The two limbs on the nonreactive curve represent the flux of the electron donor out of the system and are at two distinctly different slopes. In the absence of dispersion and biodegradation, the theoretical slope should equal to $S_0 v\epsilon$, giving a value of 481.2 mg/day for the first limb and 43.75 mg/day for the second limb. The first limb is at a steeper slope because the majority of the mass lost out the boundary is from the faster moving upper layer. The second limb is at a much lower slope, representing the mass loss out of the slower velocity lower layer.

In all reactive cases, the organic compound in the fast layer advects out of the system with very little biodegradation, and the curves are nearly coincident for the first limb. On the other hand, there is a difference in the curves for the second limb, illustrating the increased and decreased transverse dispersive effects. The total mass is reduced due to biodegradation in the slow layer, and this biodegradation increases as more electron acceptor dispersed transversely from the fast to the slow layer. The curves clearly illustrate more removal as a result of greater transverse dispersion and less for decreased transverse

dispersion. The nonreactive curves will also change as a result of the changes in the amount of transverse dispersion. To avoid confusion, these curves are not shown, and the question of whether the changes in organic removal are physical or biological is addressed below when the curves of total biomass are presented. Figure 6.9 also shows that increasing longitudinal dispersion has a dramatic effect by decreasing the total organic in the system.

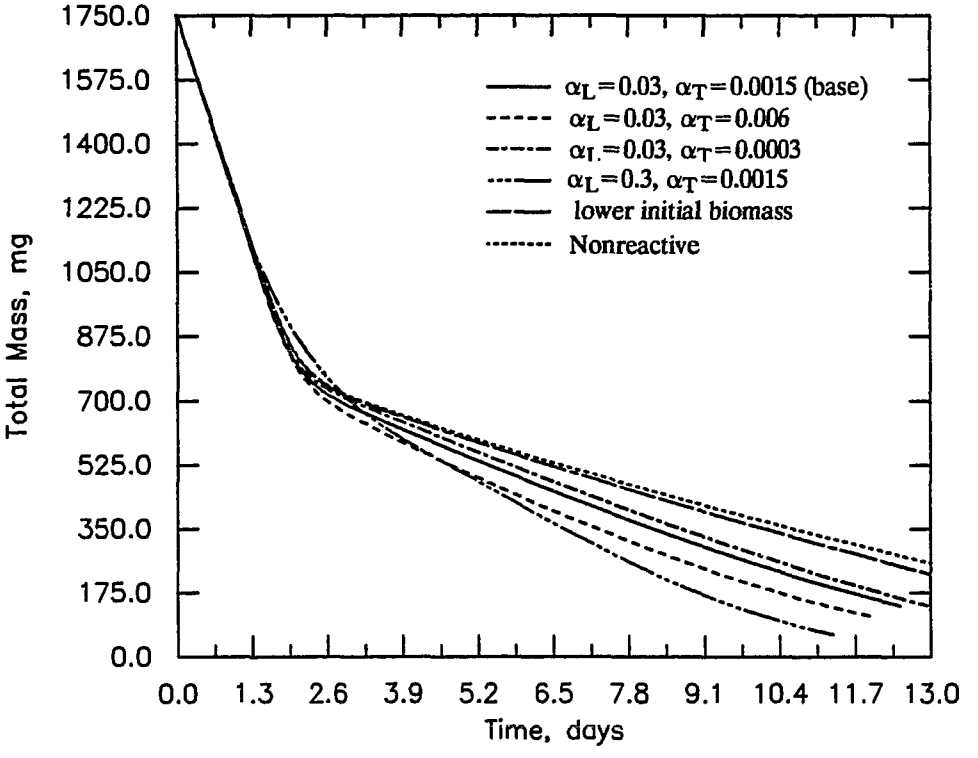


Figure 6.9. Total organic mass in the system for the four runs examining the effect of dispersion and the run examining lower initial biomass.

Figure 6.10 is a plot of the total amount of electron acceptor in the system for the same series of numerical runs. The same general behavior in response to changes in the amount of transverse dispersion are reflected in the curves. Increased transverse dispersion resulted in decreased electron acceptor mass at a given time, because electron donor and electron acceptor mixed more near the interface of the two layers, allowing biodegradation to occur for both. This means that increased transverse mixing of the

electron acceptor results in more biodegradation in dual-substrate systems. Again, a dramatic increase in biodegradation occurred for the case of increased longitudinal dispersion.

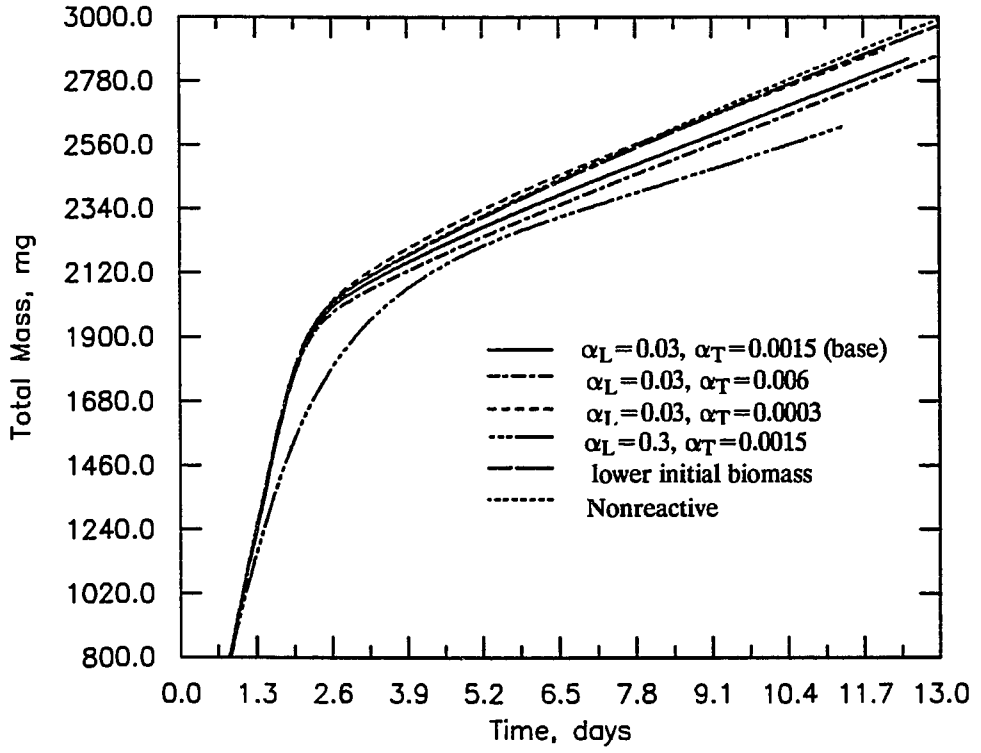


Figure 6.10. Total mass of electron acceptor in the system for the four runs examining the effect of dispersion and the run examining lower initial biomass.

Figure 6.11 shows curves of the total amount of biomass in the system for the runs described above. Increased transverse dispersion results in increased biomass. Again, increasing longitudinal dispersion has a large influence upon the total amount of biomass. The dramatic differences in the total amount of biomass clearly demonstrate that the increased removals of the electron donor and electron acceptor for increased transverse and longitudinal dispersion of the electron acceptor are mainly due to biodegradation.

It is important to visualize the spatial distribution of the substrates and biomass for this complicated stratified system. The following series of contour plots illustrates both the complexity and transient nature of these simulations. Figure 6.12 presents contour plots of

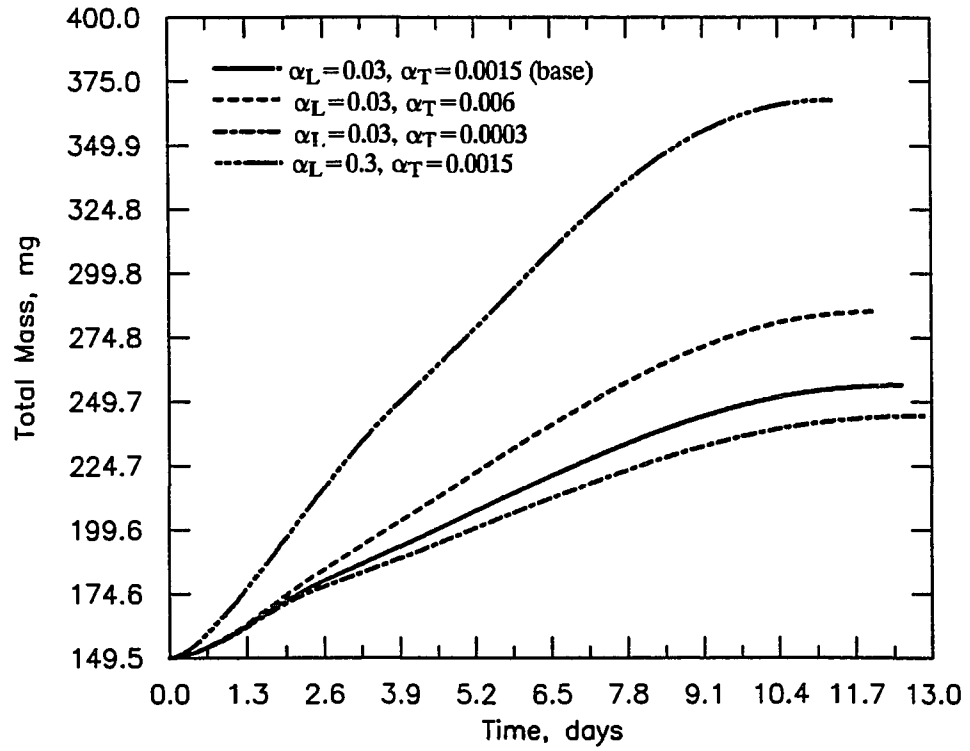


Figure 6.11. Total mass of biomass in the system for the four runs examining the effect of dispersion.

the electron donor, electron acceptor, and biomass distributions at day 1.65 into the simulation for the base case. The organic mass in the fast layer is very close to being washed out of the system at this point in the run. There is some amount of removal as a result of the transverse dispersion of the electron acceptor from the fast to the slow layer.

The second contour plot in Figure 6.12 is of the electron acceptor and shows evidence of substantial transverse dispersion of the electron acceptor into the slow layer. Also, the injection electron acceptor concentration in the top layer is very close to reaching the downstream boundary of the system. The gradient at the interface between the layers is extremely high due in large part to the tenfold difference in the velocity between the two layers.

The snapshot of the biomass distribution shown on the bottom plot in Figure 6.12 reveals a good history of what has happened thus far in the system. The closed loop

protruding into the upper layer is the effect new biomass growth resulting from transverse dispersion of the electron acceptor into the slower layer combined with decaying biomass following previous growth at the electron donor/ electron acceptor interface. From the examination of earlier contour plots, there are also remnants of decaying biomass near the upstream end of the upper layer. The maximum biomass concentration occurs close to the source in the bottom layer and along the layer interface near the source. This growth reflects contact between the electron donor and electron acceptor. This contour plot truly exemplifies the two–dimensional nature of the stratified flow and transport problem and illustrates the complexities involved in a strongly nonlinear problem.

Figure 6.13 is a snapshot of the electron donor, electron acceptor, and biomass at day 11.55 and is close to the simulation stopping point of 12.485 days. An enormous amount of transverse dispersion has caused the removal of the electron donor, as shown in the first contour plot of Figure 6.13. At this point in the simulation, all the electron donor and electron acceptor has advected out of the top layer. The transverse removal of the electron donor is attributed to the electron acceptor spreading transversely into the electron donor plume, causing a substantial amount of biomass growth at their interface. There is also a large longitudinal penetration of the electron acceptor into the electron donor plume, due to the intermixing of electron donor and electron acceptor and subsequent biomass growth at their interface.

The snapshot of the electron acceptor plume in Figure 6.13 reveals less transverse penetration of the electron acceptor than the electron donor. This is due to the electron donor being the rate–limiting substrate at the edge of the electron donor plume, which allowed the excess of electron acceptor to disperse further laterally, thereby initiating increased lateral biomass growth and subsequent removal of electron donor. This means that there is more electron acceptor in the system than is necessary to completely oxidize the electron donor; therefore, there are no longer any transverse gradients of the electron acceptor once it is in excess.

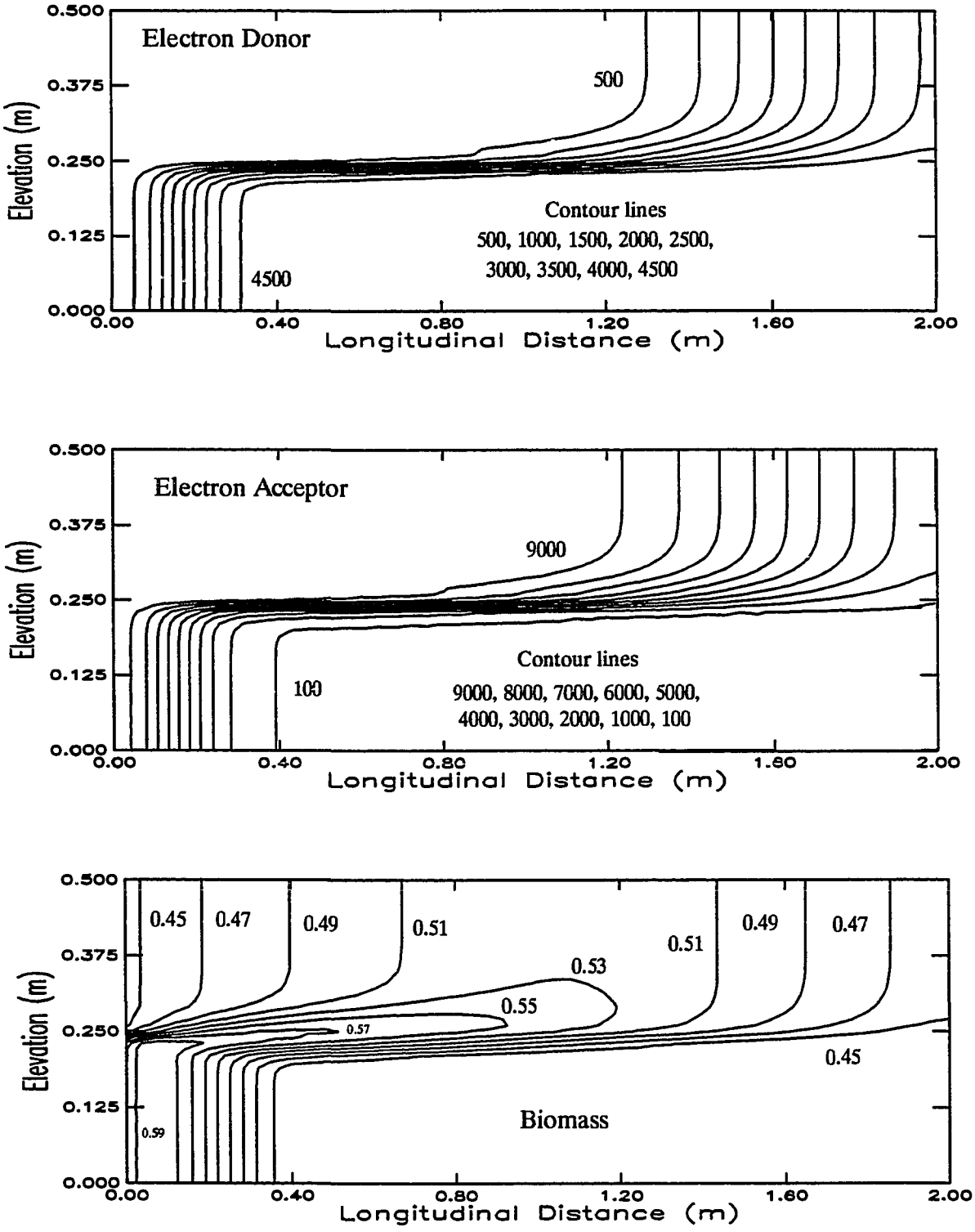


Figure 6.12. Contour plots of the electron donor (μg/L), electron acceptor (μg/L), and biomass (mg/L) at time 1.65 days.

The final snapshot in Figure 6.13 is of the biomass and again reveals a time history of events in the simulation. The upper layer has remnants of slowly decaying biomass, as evidenced by the 0.50 mg/L contour line, even though there is virtually no electron donor remaining. The biomass is decaying due to lack of electron donor in the upper layer. The fingering at the interface is due to combined effect of longitudinal and transverse spreading of the electron acceptor into the electron donor plume. The new growth of biomass in the system is occurring in the lower right hand corner of the plot, where the electron donor and electron acceptor are intermixing.

The above results demonstrate the relative importance of longitudinal and transverse dispersion of the electron acceptor in a stratified system. The results of the two–dimensional transport simulations of electron donor, electron acceptor, and biomass allowed quantification of these different dispersive variables in terms of their contributions to biodegradation processes. Increased transverse dispersion promoted increased biodegradation of the electron donor as a result of electron acceptor mixing into the lower velocity layer. Conversely, decreased transverse dispersion resulted in lower electron donor degradation and inhibited transverse spreading of the electron acceptor into the slower velocity layer. Increased longitudinal dispersion resulted in greater mixing at the electron donor/electron acceptor interface, which led to increased biomass growth and enhanced biodegradation of the electron donor. The findings in this section support the hypothesis that layering can play an important role in understanding biodegradation processes in the subsurface.

In closing, the key to biomass development and substrate utilization is having electron donor and electron acceptor simultaneously present. As dispersion increases, the mixing region between the injected electron acceptor plume and the background electron donor plume increases. Hence, increased longitudinal dispersion results in an enhanced biologically active zone (BAZ) that travels with the fronts in each layer. Increased transverse dispersion results in increased transport of the electron acceptor from the fast

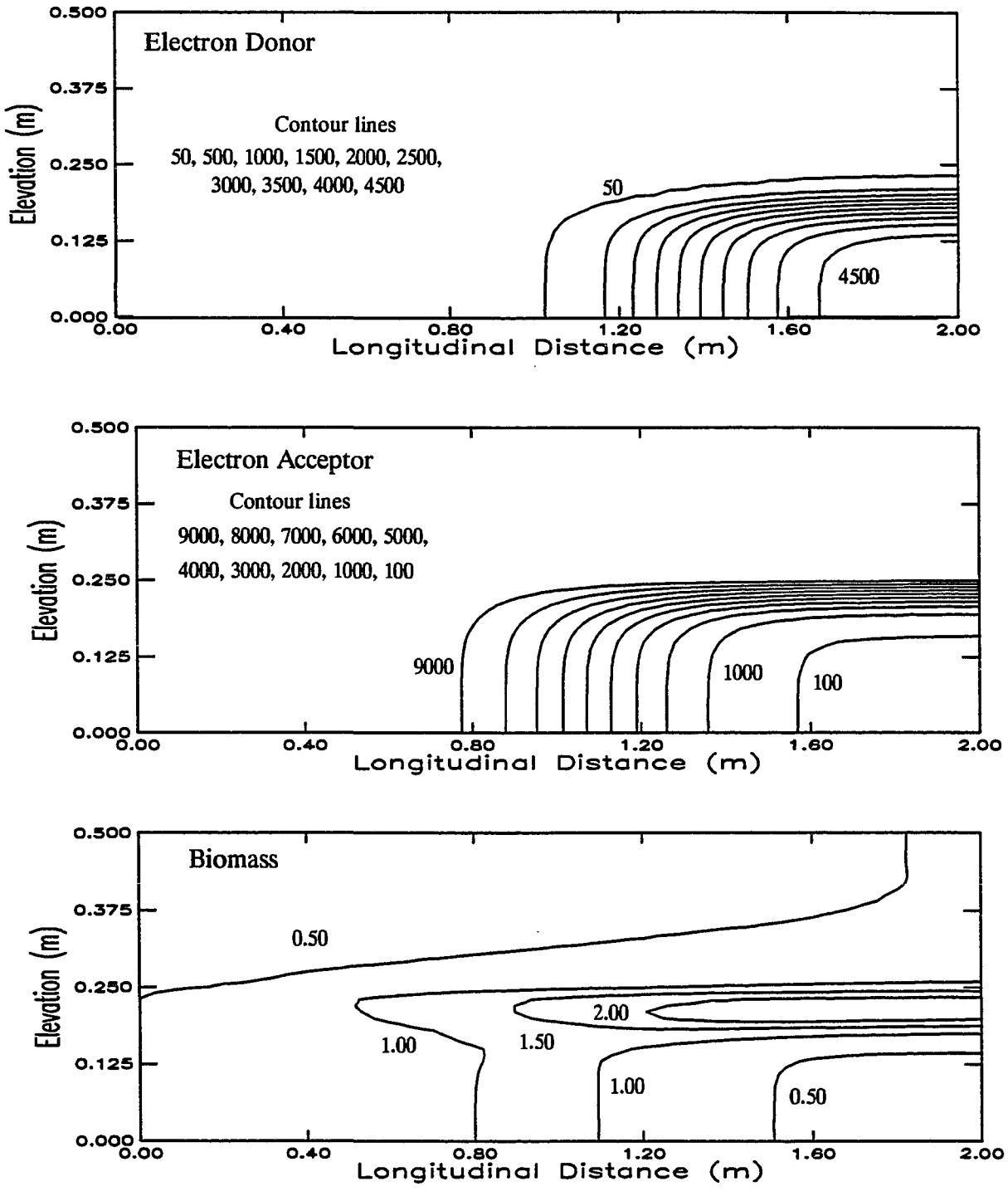


Figure 6.13. Contour plots of the electron donor (μg/L), electron acceptor (μg/L), and biomass (mg/L) at time 11.55 days.

layer into the slow layer and, hence, results in an enhanced BAZ located near the layer interface.

### 6.3.2 Effects of Initial Biomass Concentration

The amount of initial active biomass in an aquifer is a highly uncertain parameter that has an important impact on the development of the amount of biological reaction. In Chapter 4, the initial number of cells per gram of dry soil was chosen to be $10^6$. To gain insight on the relative impact of this parameter on the model system, the initial biomass concentration is lowered by an order of magnitude to $10^5$ cells/gram dry soil, which translates to 0.0427 mg cells/L.

The same problem of the base case was solved; the only change was in the lower initial biomass concentration. Figures 6.9 and 6.10 show curves for the total amount of electron donor and electron acceptor in the system for the run with the order of magnitude lower initial biomass concentration. It is apparent when comparing each curve to the nonreactive curves that a very small amount of biodegradation takes place at this biomass concentration. When the curves are compared to the base case, a substantial amount of biodegradation occurs due to the increased initial biomass concentration. In terms of total new growth of biomass at steady state, the background amount of 14.95 mg of biomass increased 2.16 times to 47.19 mg total biomass at steady state, which implies there was 32.29 mg of total new growth. This is in comparison to the total amount of new growth in the base case, which was 0.71 times the background concentration of 149.5 mg, or 106.52 mg, i.e., there was 3.30 times more total biomass in the base case than in the case of an order of magnitude lower initial biomass concentration. Steady-state occurred at 19.12 days as opposed to the base case, 12.485 days. The total amount of electron donor biodegraded at 12.485 days for the case of lower biomass was 28.91 mg, compared to 137.04 mg for the base case. The amount biodegraded was determined by subtracting the total amount of organic in the system from the nonreactive curve. Therefore, the base case biodegraded 4.74 times more electron donor than did the run with the lower initial

biomass. The main conclusion is that lowering the initial biomass concentration can have a dramatic effect on the total amount of biodegradation that can take place when the domain is small enough that the substrate is washed out before the biomass can grow to a significant mass.

### 6.3.3 Continuous Upstream Source of Electron Donor

The objective of this section is to add injection of electron donor to the base case of Section 6.3.1. Figure 6.14 shows the hypothetical contaminant scenario that motivates the

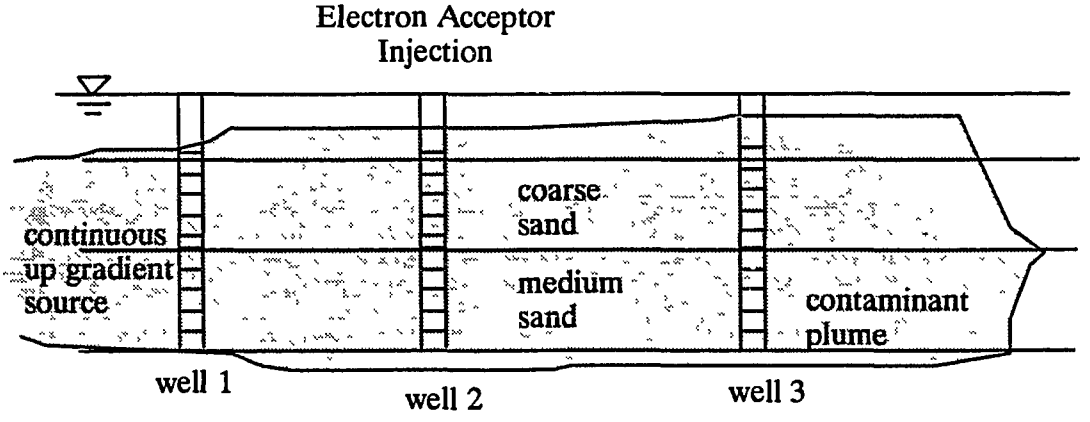


Figure 6.14. Hypothetical contaminant scenario for the numerical experiments of continuous injection and background concentration of electron donor.

numerical simulation of this section. This reflects another potential realistic situation where there is a substantial source of organic contamination upgradient of the biostimulated zone. The continuous upgradient source of electron donor is simulated in the computer model by adding a continuous source at well 2. In the previous simulations, the uniform background concentration was allowed to advect through the domain with no supply at the source. In addition to the phenomena demonstrated in those simulations, the simulation of this section exhibits biomass growth at the source. All the base case parameters were utilized, the only difference being that the electron donor was also injected across the upstream boundary at a concentration equal to 5 mg/L (see Figure 6.7). The results of this simulation are shown in Figures 6.15–6.17.

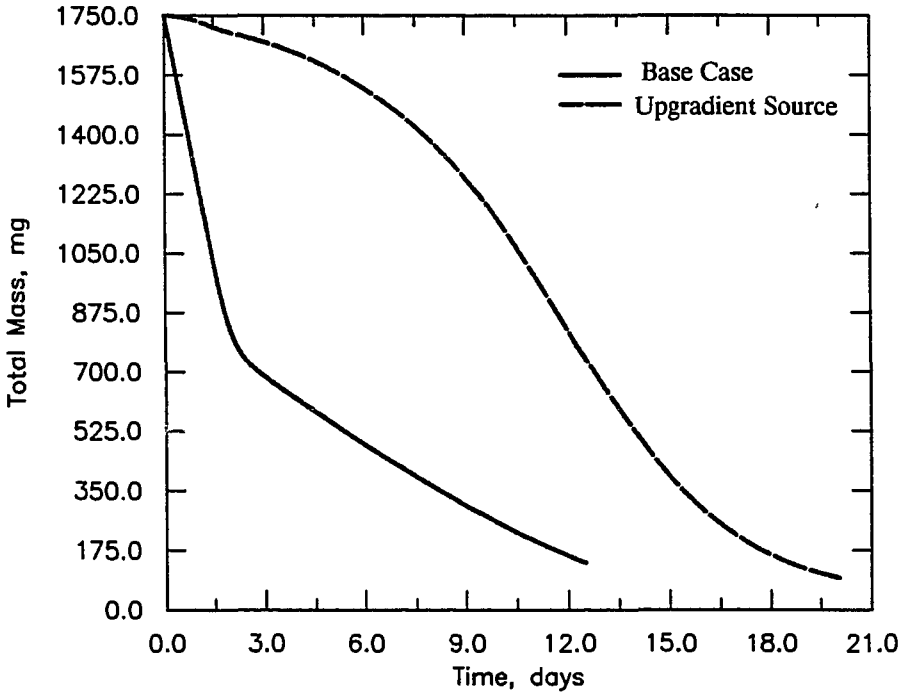


Figure 6.15. Total mass of electron donor in the system for the base case and continuous source of electron donor experiment.

The mass curve of the electron donor is shown in Figure 6.15 and is compared to the base case of section 6.3.1. The mass curve for the electron donor for the simulation of this section would be horizontal at 1750 mg in the absence of biodegradation. Therefore, the difference between 1750 mg and the dashed line in Figure 6.15 represents the approximate amount of biodegradation of the electron donor. This difference is in contrast with the amount of biodegradation that occurred in the base case run. When the base case's nonreactive and reactive organic mass curves are compared in Figure 6.9, the amount of biodegradation is relatively small. The steady-state was defined by $\Omega$ = 0.05%, and occurred at 20.042 days for the continuous source of electron donor simulation. Recall that for the base case, the stopping point was 12.485 days, which was approximately the time when all the electron donor washed out of the system. The convergence criterion defining steady-state for the continuous source experiment was less strict in order to stop the simulation at a reasonable time ( approximately 20 days). This allowed the transient behavior of each system to be compared on the same set of axes and

forced the continuous source of electron donor simulation to stop when the total mass in the system was similar to that of the base case.

Figure 6.16 shows the mass curves of the electron acceptor for the continuous source simulation and the base case. The two curves have nearly the same behavior for the first 3.0 days, when growth at the source starts to increase rapidly for the continuous source of electron donor run. The continuous curve levels off as the biomass near the source has to utilize a stoichiometric amount of electron acceptor for the degradation of the electron donor. This is a key difference when compared to the base case.

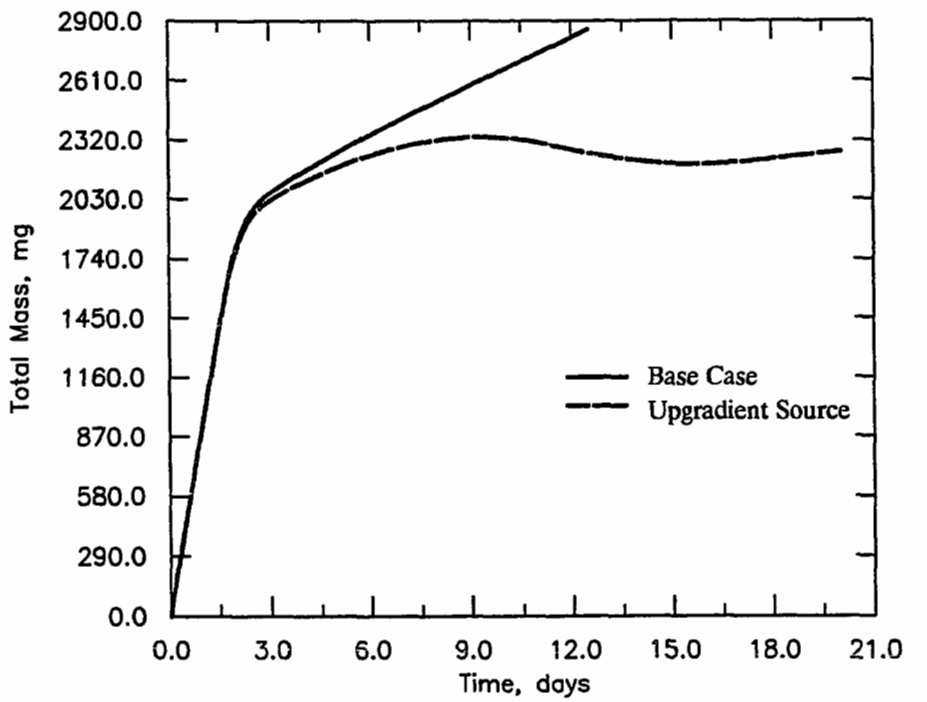


Figure 6.16. Total mass of electron acceptor in the system for the base case and continuous source of electron donor experiment.

The final comparison is of the mass curves of the total biomass in the system, shown in Figure 6.17, for the run of this section and the base case. This plot illustrates biomass build–up at the source as a result of the continuous source of electron donor. There is nearly 20 times more biomass in the system at steady–state compared to the base case. The large biomass growth as a result of the continuous source of electron donor is the major difference between the two scenarios. The maximum biomass concentration in the slow

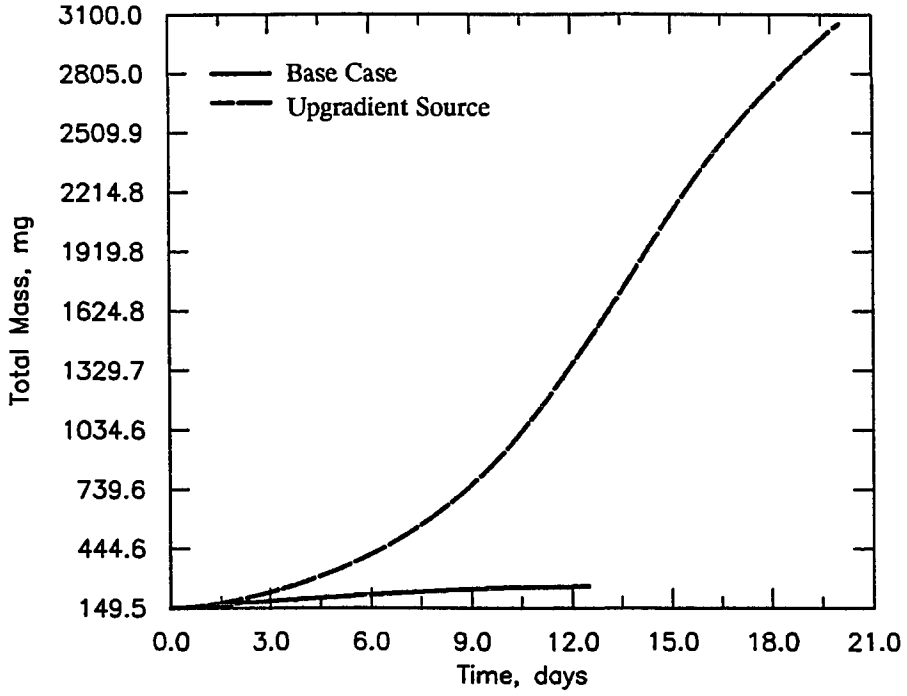


Figure 6.17. Total mass of biomass in the system for the base case and continuous source of electron donor experiment.

and fast layers at steady-state were 28.07 mg/L and 29.38 mg/L, respectively. The maximum concentration in the base case was approximately 2.34 mg/L. Again, this is attributed to the dominant localized biomass growth for the continuous source of electron donor.

The effect of adding a continuous source of electron donor can be seen clearly by examining contour plots of the electron donor, electron acceptor, and biomass at 10 and 20 days into the simulation. Figure 6.18 shows the spatial distribution of the concentration of the two substrates and the biomass at 10 days into the simulation. The electron donor distribution shows evidence in the bottom layer that biomass is beginning to accumulate close to the source and that there is about to be a splitting off of a slug that will slowly biodegrade as it passes out the down-gradient boundary. This behavior is not evident in the fast layer, because the high velocity has carried most of the electron donor out of the down gradient boundary. The electron acceptor snapshot shows a large amount of transverse spreading of the electron acceptor from the fast to the slow layer. This results

in a substantial amount of electron donor biodegradation in the slow layer, as confirmed by the snapshot of the electron donor. The combined effects of transverse migration of the electron acceptor and biomass growth near the influent boundary is revealed in the snapshot of the biomass. The biomass is spread out over a much larger longitudinal distance in the upper layer as a result of the tenfold greater velocity than in the lower layer. There is also a substantial amount of biomass extending into the lower layer as a result of transverse dispersion of the electron acceptor.

The concentration distributions of Figure 6.19 show the two substrates and the biomass at 20 days into the simulation. These snapshots reveal the dramatic effect of adding a continuous source of electron donor. The electron donor distribution illustrates the classic removal of substrate due to biomass buildup near the source as well as the effect of stratification. The transverse concentration gradient near the source is large even at this snapshot close to steady–state conditions. While down gradient of the localized increased biomass concentration, the pinched–off slug of electron donor is slowly advecting and biodegrading as it moves toward the down gradient boundary. The same general trends are apparent for the electron acceptor distribution. The amount of electron acceptor being added to the system is stoichiometrically in excess of that required to remove the electron donor, i.e. there is approximately 7 ppm of electron acceptor moving out the boundary (approximately 3 ppm consumed) while nearly all, 5 ppm, of the electron donor is consumed. The biomass distribution shows how much more the biomass is spread out over the faster top layer than in the bottom layer. Once the slug of electron donor and electron acceptor has moved out the boundary, the 2 and 1 ppm isolines of biomass will move back towards the source.

The snapshots at 10 and 20 days demonstrate the large difference adding the continuous source has on the mechanisms controlling biodegradation. Two regions of biological activity evolve, the near and far field. The near field is characterized by a large buildup of biomass near the source. The far field is characterized by a moving zone of

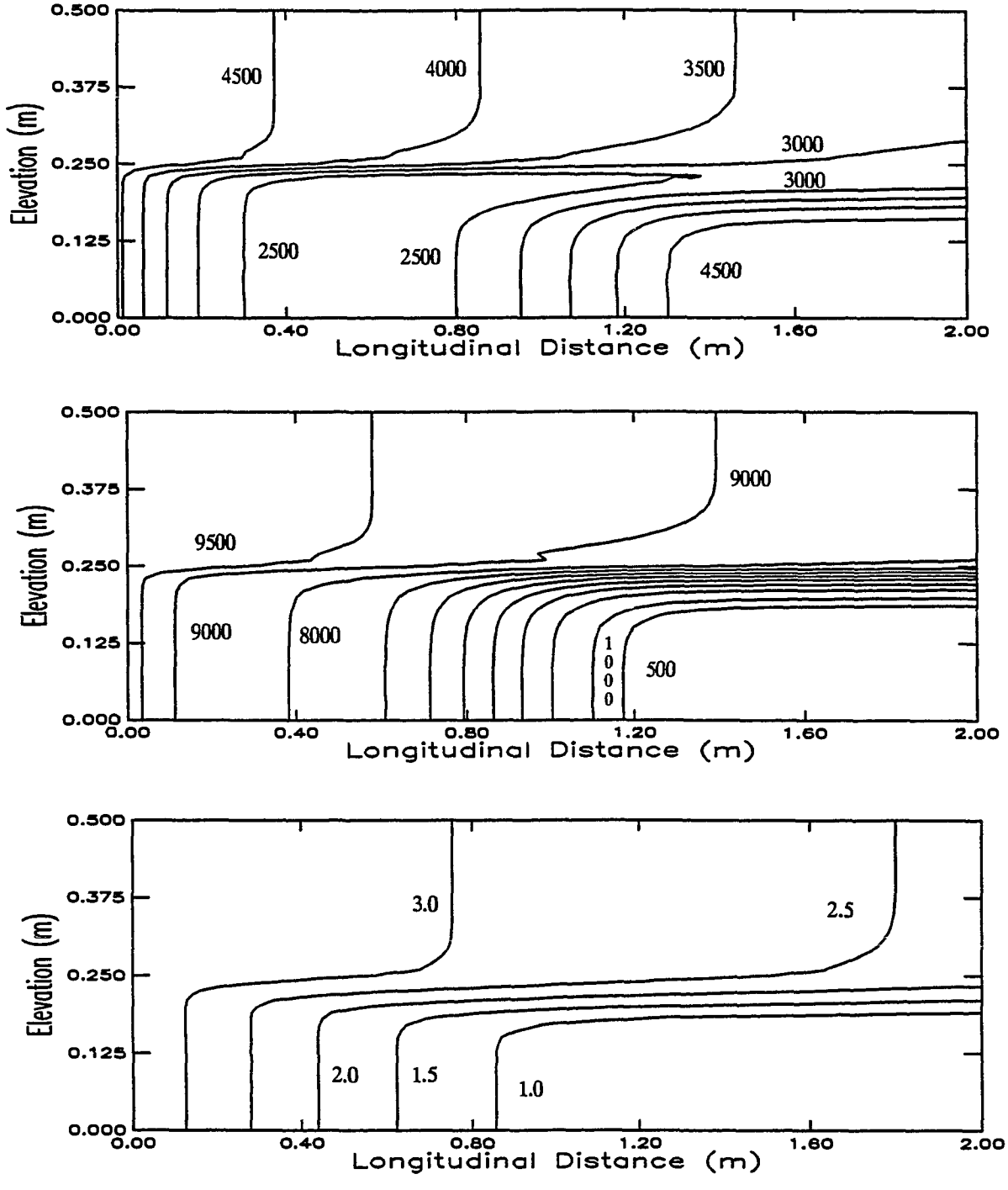


Figure 6.18. Contour plots of the electron donor (μg/L), electron acceptor (μg/L), and biomass (mg/L) at time 10.0 days for a continuous source of electron donor.

increased biological growth or BAZ. These generalizations are compared to the case where there was not a continuous source of electron donor, shown in Figures 6.12 and 6.13. In that previous case, there was no near field growth and all the biomass growth followed the electron donor plume as it advected out the boundary.

Localized biological growth near the sources of electron donor and electron acceptor has a tremendous amount of biodegradation potential compared to the far field transient biomass that develops mainly from inter-layer mixing of electron donor and electron acceptor. A clear designation of the type of biodegradation to which one is referring is important (steady state versus transient biomass growth).

## 6.4 Summary and Conclusions

Two major areas related to biodegradation modeling in stratified groundwater systems were investigated in this chapter. First, the effect of stratification was examined in terms of biomass development and subsequent removal of rate-limiting electron donor by comparison to an equivalent homogeneous system. The behavior of the two systems was evaluated by the use of mass curves of electron donor and biomass and from contour plots of both the stratified and homogeneous systems at selected times. The major finding was that the effect of stratification can be approximated by an equivalent homogeneous system for steady state only; for the transient situation, stratification allowed greatest biodegradation, due to transverse mixing of the electron donor and electron acceptor, across the layer interface.

Second, the behavior of stratified systems of coupled electron donor, electron acceptor, and biomass was investigated in terms of how certain physical, biological, and chemical parameters play a role in the behavior of such systems. More specifically, the effects of longitudinal and transverse dispersion were found to be significant.

The importance of the initial biomass concentration in the system was evaluated through a simulation with an order of magnitude lower biomass concentration than the so-called base case. The combined effect of localized biological growth at the source and

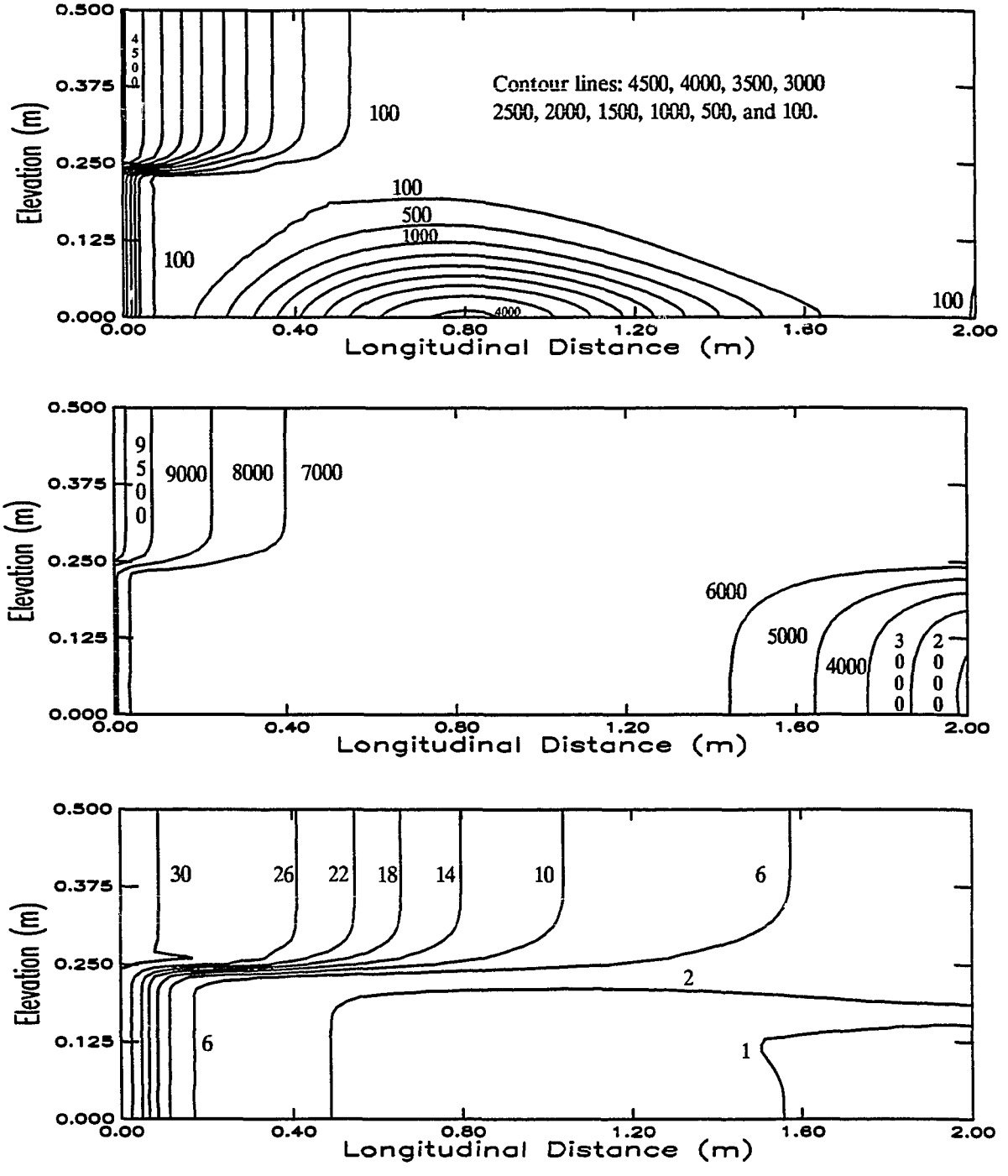


Figure 6.19. Contour plots of the electron donor (μg/L), electron acceptor (μg/L), and biomass (mg/L) at time 20.0 days for a continuous source of electron donor.

far-field behavior were examined by adding a continuous source of electron donor. The previous experiments in the section were performed with only the background concentration of electron donor initially and no supply during the simulation.

The following specific conclusions can be drawn from the results of the numerical experiments of transport and biodegradation in stratified porous media presented in this chapter.

1. The effect of stratification upon substrate removal is dramatic at the early stages of biomass development for a continuous source of rate-limiting substrate. Toward the steady state of the continuous source problem, the effect of stratification became less dominant, as a significant amount of biomass near the source developed. The overall removal of the rate-limiting compound became equal to that in a hydraulically equivalent homogeneous system for steady state.

2. For dual-limitation systems, where electron acceptor is input into a domain with background electron donor, transverse mixing of the electron acceptor caused significant increased biomass growth and subsequent removal of the electron donor. This was mainly due to transverse dispersion of the electron acceptor from the faster layer into the slower. This mixing of the electron donor and electron acceptor led to localized biomass growth near the interface.

3. A tenfold increase in longitudinal dispersion over an initial base case for a fixed amount of transverse dispersion had a substantial effect on electron acceptor mixing into the electron donor plume. It resulted in substantially more biomass and substrate removal than in the base case.

6. Reduction of the background concentration of active bacteria in the base case problem had a noticeable impact on decreasing the amount of biodegradation that took place.

7. When a constant source of electron donor was supplied to a base case problem with only a background concentration of electron donor, a substantial amount of biomass grew at the injection well, and the behavior of the system was drastically different. This steady

state growth versus the localized biomass growth of the base case represent extremes in terms of the behavior of natural systems.

# 7. THE EFFECT OF SORPTION ON TRANSPORT AND BIODEGRADATION IN A DUAL SUBSTRATE, ONE-DIMENSIONAL POROUS MEDIA

## 7.1 Introduction

The previous chapter demonstrated that the key to biological activity for dual substrate systems is to stimulate a Biologically Active Zone (BAZ) where electron donor and electron acceptor are simultaneously high. In the case where the electron acceptor is injected into a background of electron donor, these zones are: (1) a mixing zone controlled by longitudinal dispersion between the migrating electron donor and electron acceptor fronts, and (2) a mixing zone controlled by transverse dispersion between electron acceptor in the fast layer and the electron donor in the slow layer. The former zone is dynamic and is caused by the displacement of the electron donor by the electron acceptor, whereas the latter mixing zone is relatively stationary and is associated with the heterogeneity of the aquifer.

Because of the high solid-water interfacial area of natural porous media, sorption is an additional important process governing the transport of organic compounds. Sorption retards the advective transport velocity of the organic compound, which usually is the electron donor. However, since most electron acceptors are not retarded, the advective velocity of the electron donor may be less than that of the electron acceptor. For cases typical of *in situ* bioremediation, in which the electron acceptor is injected into a contaminated groundwater plume, retardation can cause greater mixing between the migrating fronts, thus increasing the potential for simultaneously high concentrations of electron donor and electron acceptor and for enhanced biological activity .

Due to the nonlinear nature of the transport and biodegradation systems, retardation can have a complex effect. The reaction rate of the electron donor, as explained in Chapter 3, is represented mathematically by the following equation:

$$R_S = \frac{M_T q_m}{R_{fS}} \left( \frac{S}{K_S + S} \right) \left( \frac{A}{K_A + A} \right) \qquad (7.1)$$

Because the electron acceptor front travels faster than the electron donor front, $R_S$ can increase as $R_{fS}$ (the linear equilibrium retardation factor) increases, since a greater portion of the flow domain experiences high electron acceptor and electron donor concentration simultaneously. However, (7.1) shows that retardation effectively lowers the reaction rate, $R_S$, by lowering the electron donor concentration.

The overall objective of this chapter is to examine the influence of sorption upon coupled transport and biodegradation processes in one dimension. To better understand and evaluate the important phenomena related to sorption and biodegradation in homogeneous systems, the following two specific objectives are considered in this chapter:

1. Examine in detail the effect of linear equilibrium retardation of the electron donor of the dual-substrate system undergoing biodegradation and transport processes in a homogeneous porous medium.
2. Determine the effect of velocity and sorption upon the mass of electron donor biodegraded in a dual-substrate, homogeneous system.

## 7.2 Detailed Examination of the Interaction of Biodegradation and Sorption

The objective of this section is to identify the effects that retardation of the electron donor have when electron acceptor is input into a system containing background contamination of electron donor. This section examines in detail the important interacting phenomena that occur in these complicated systems. The visual representation used as the basis for this section is illustrated schematically in the previous chapter as Figure 6.7 for the stratified case; here we consider a homogeneous system in order to eliminate complicating factors due to heterogeneity. The simulations were carried out with the same base-case physical and biological parameters used for the dual-substrate transport problem in Section 6.3 and shown in Figure 6.7. In order to examine the

influence of retardation, transient simulations were performed at a pore–liquid velocity of 0.10 m/day, and with the electron donor having a retardation factor equal to 3. The only differences between this scenario and the base case in Chapter 6 are that the electron donor is retarded, the system is homogeneous rather than stratified, and the length of the computational domain is 6 m, as opposed to 2 m. As in the Chapter 6 simulations, the electron acceptor was injected at a concentration equivalent to 10.0 ppm at the left hand boundary into a background concentration of 5.0 ppm of electron donor.

Figure 7.1 shows the normalized mass of electron donor biodegraded for the base case simulation of this section with a 6 m long computational domain. The mass is normalized by the retardation factor of the electron donor. Two computer simulations, one reactive and the other nonreactive, were required to generate the curve shown in Figure 7.1. In each simulation, the total mass of electron donor present (in the sorbed and dissolved phases) in the system at any particular time was computed by numerically evaluating

$$M_S(t) = \int_0^{L_x}\int_0^{L_z} \epsilon\, R_{fS}\, S(x,z,t)\, dzdx \qquad (7.2)$$

Therefore, the total mass of electron donor biodegraded equals the difference between $M_S(t)$ in the nonreactive and reactive simulations; this quantity divided by $R_{fS}$ is what is plotted on the ordinate of Figure 7.1. However, as the electron donor front migrates out the downstream boundary of the domain, the mass biodegraded is underestimated by this method, because the nonreactive simulation 'loses' greater mass by advection out of the system than does the reactive simulation. The curve plotted in Figure 7.1 reaches a maximum value at day 85, where the electron donor begins to wash out of the system. Therefore, the curves illustrate the change in the mass of electron donor biodegraded only prior to the beginning of washout.

Two different, approximately linear–sloped regions can be defined; these are denoted Regions 1 and 2 in Figure 7.1. The slopes of Regions 1 and 2 are 181 mg/day and 85.5 mg/day, respectively. As will be discussed further, these two regions are indicative of an

early–time rapid growth period and a long–term quasi–steady state. The Region 2 curve also displays a mild cyclic behavior about the mean of the linear trend indicated by the dashed line in Figure 7.1. Longitudinal profiles of the electron donor, electron acceptor, and biomass at selected times help explain these two different regions in detail.

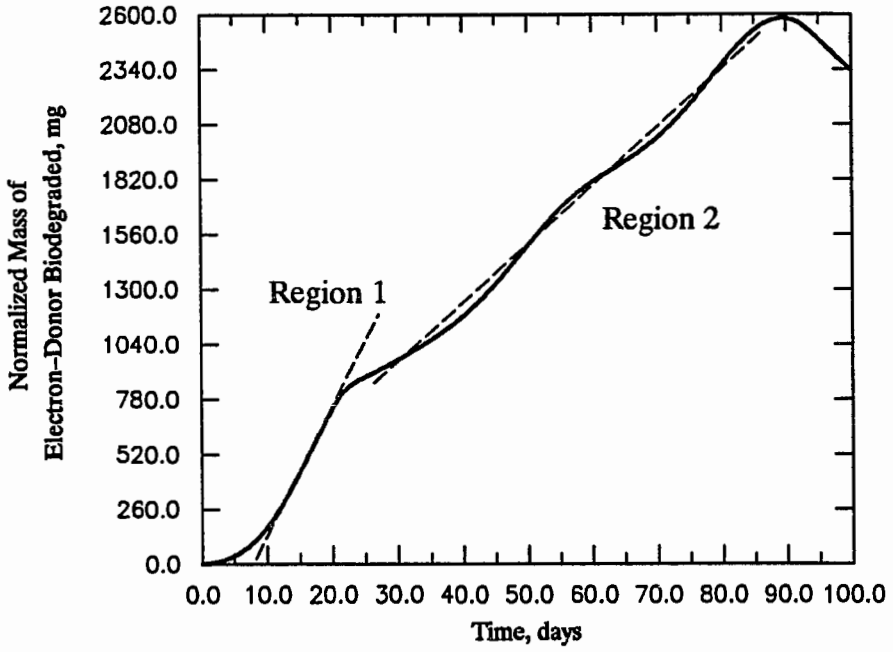


Figure 7.1. Mass of electron donor biodegraded for the simulation with the longer grid length with the retardation factor of 3 and v=0.10 m/day.

Snapshots of the electron donor, electron acceptor, and biomass at eight times are shown in Figure 7.2. The peculiar shape of the electron acceptor front at day 15 is the result of increased electron–acceptor utilization due to rapid biomass growth in the vicinity of the retarded electron–donor front. In the absence of degradation, the injected electron acceptor moves at a speed of 0.10 m/day, and the displaced electron donor front moves at a speed of 0.033 m/day. The forward "limb" of the electron acceptor profile at day 15 appears to be located at x = 1.5 m and, hence, corresponds approximately to nonreactive transport behavior. Due to continuing injection of electron acceptor, a region of enhanced biological activity develops in the vicinity of the retarded electron

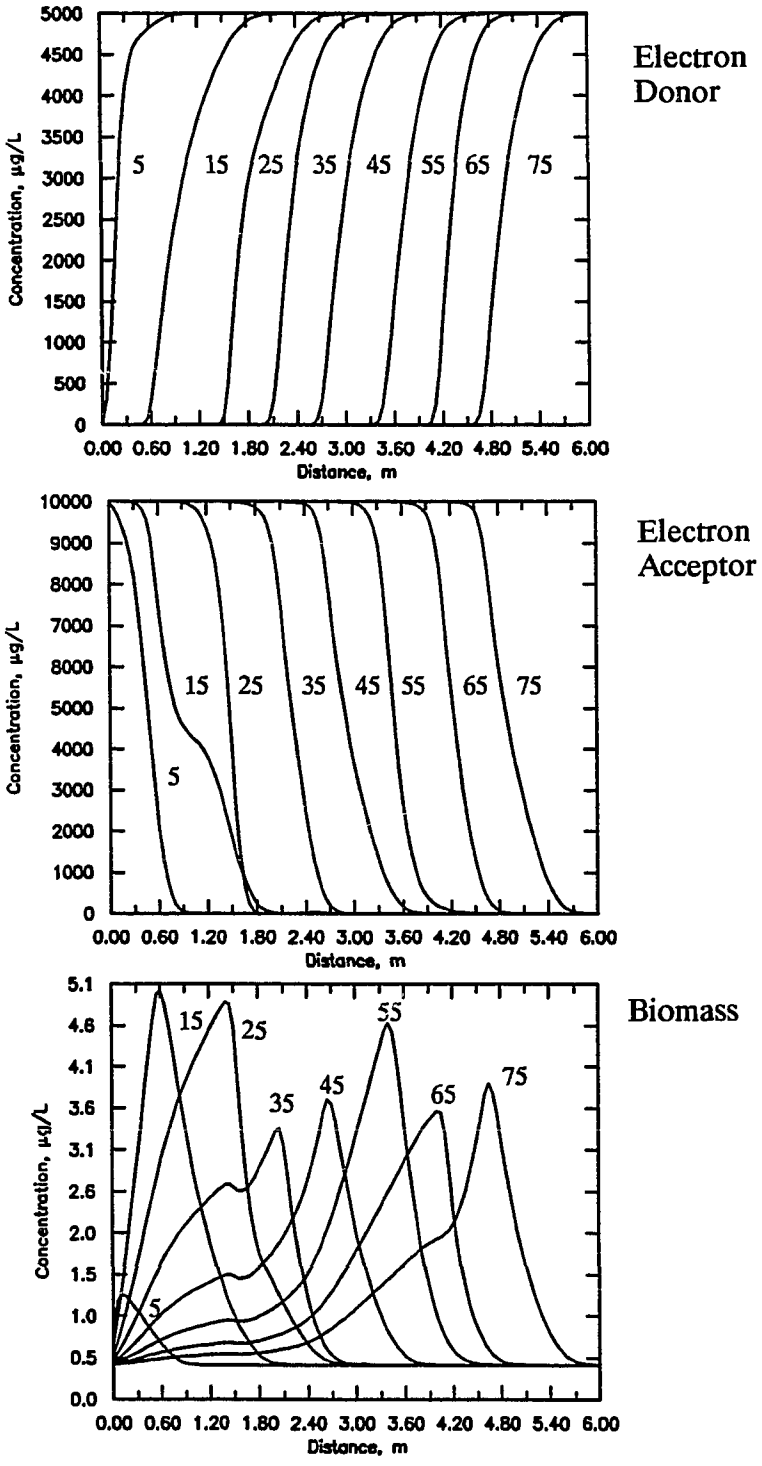


Figure 7.2 . One–dimensional snapshots of the electron donor, electron acceptor, and biomass at the indicated times (days) for a retardation factor of 3 at a velocity of 0.10 m/day for the 6 m domain.

donor front. Most of the injected electron acceptor is utilized in this region. The snapshots of the biomass show that the greatest biomass growth occurs at the interface between the electron donor and electron acceptor fronts. The electron donor profile at day 25, during the transition from Region 1 to Region 2, has a slightly different shape from that at day 15. The profiles from day 35 to 75 vary slightly in shape and are shifted non-uniformly, which is consistent with the apparent cycling about the line drawn through Region 2 in Figure 7.1.

The snapshots of the electron acceptor in Figure 7.2 reveal the apparent upgradient retreat of the electron acceptor toward the vicinity of greatest biomass growth and indicate that different processes are taking place in Region 1 versus Region 2. The profile at day 25 is in the transition between Regions 1 and 2 and takes a shape more similar to the those in Region 2. The profiles within Region 2 again exhibit the apparent cyclic behavior in their shape and the spacing between them.

The snapshots of the biomass shown in Figure 7.2 show a change in the biomass profile shape after day 25. Biomass growth is rapid and concentrated in Region 1, but more spread out in Region 2. The biomass profiles in Region 2 again illustrate cyclic behavior. It is interesting to note the similarities between the profiles at days 45 and 75 and to carefully examine where these times fall within the cycles shown in Figure 7.1. They occur as the cycle moves above the average line. It appears that the fronts at days 45 and 75 correspond to the beginning and end of one approximately complete cycle. The cyclic behavior is illustrated quite clearly in the total amount of biomass curve shown in Figure 7.3.

In order to gain additional insight into the key difference between Regions 1 and 2 and the apparent cyclic phenomena characteristic of Region 2, normalized profiles of the electron donor, electron acceptor, and biomass at selected times are examined. The normalization of the electron donor and electron acceptor was performed by dividing the concentration values by the background and injection concentrations, respectively. The normalization of the biomass was performed by subtracting the background biomass

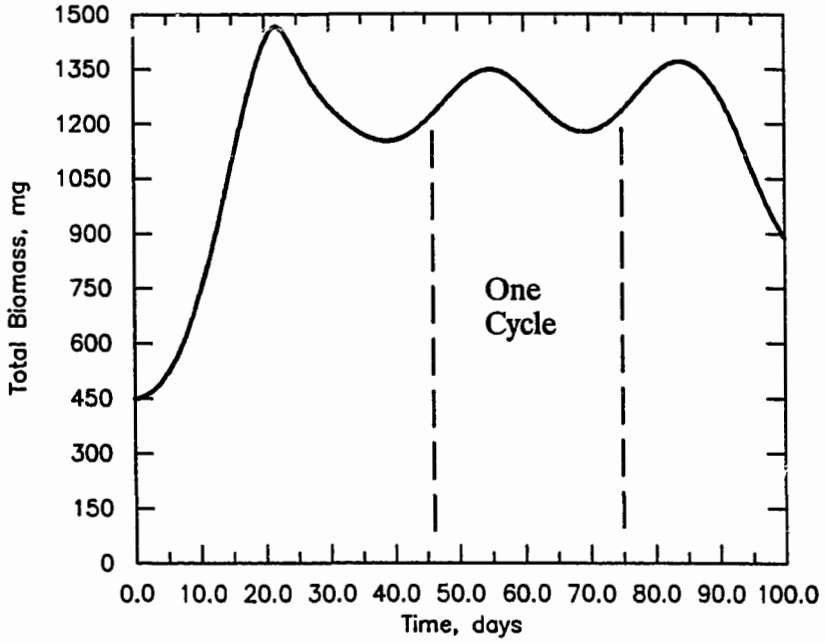


Figure 7.3. Total biomass in the system for a retardation factor of 3 at a velocity of 0.10 m/day for the longer domain experiment.

concentrations from the biomass concentration values and dividing the difference by 5.024 mg/L, the maximum biomass concentration in Figure 7.2. Figure 7.4 shows the normalized profiles of the electron donor, electron acceptor, and biomass for days 15, 55, and 70. The profiles at day 15 are representative of Region 1 behavior. As discussed previously, the Region 1 behavior corresponds to the initial rapid growth phase. The electron–acceptor profile at day 15 is in the process of being "pinched off" by the intense biological reaction kinetics taking place. The peak of the biomass curve at 0.5 m coincides with the bend in the electron acceptor curve at approximately 1 meter into the domain. The key point is that all three profiles overlap quite a lot, especially near 0.9 m.

The normalized profiles of the three constituents at days 55 and 75 in Figure 7.4 demonstrate the cyclic behavior of Region 2. These times correspond to the maximum and minimum of the total biomass curve (Figure 7.3) within the same cycle. A maximum occurred at day 55 and a minimum at day 70 within the cycle bounded approximately by days 46 and 75, i.e. a 29–day cycle length. The influence of dispersion and differential front

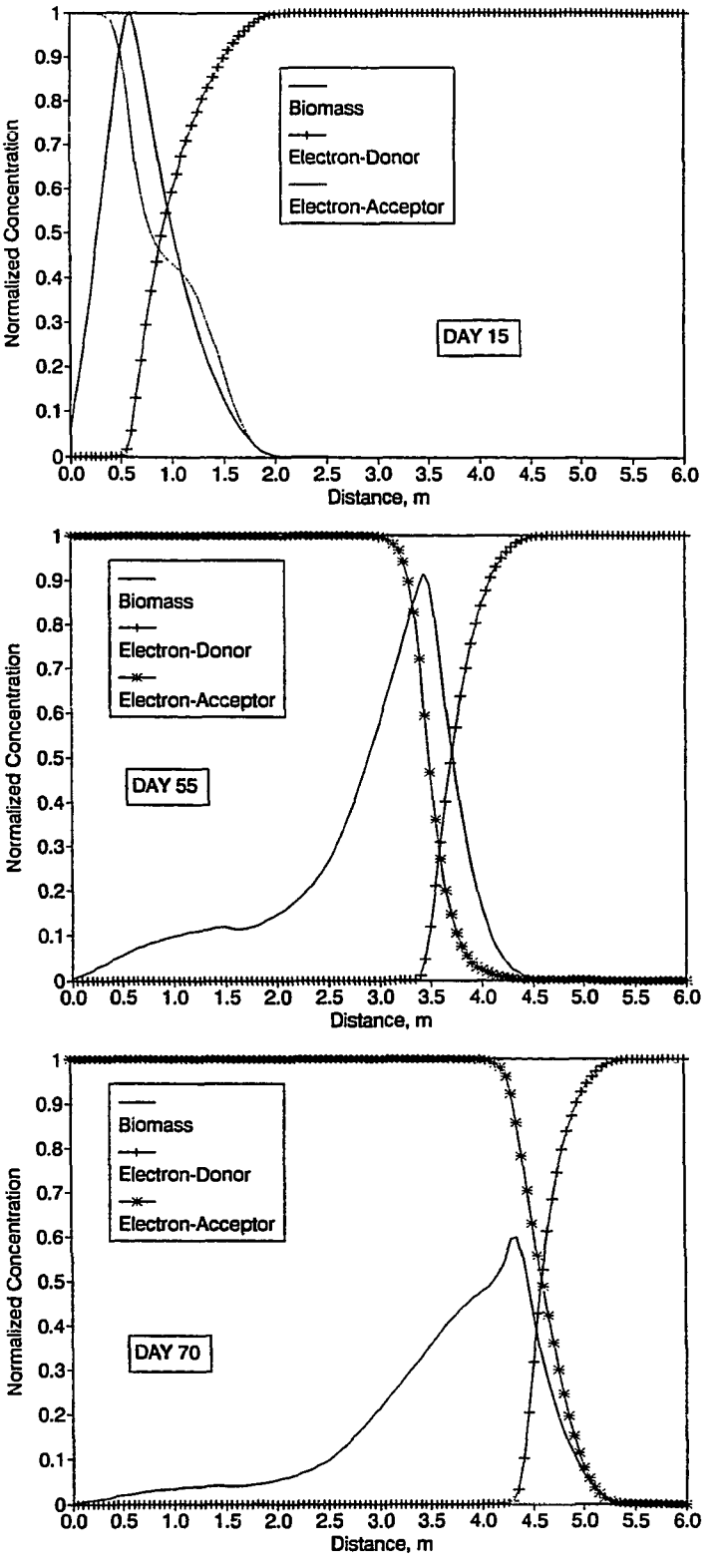


Figure 7.4. Normalized distribution of the electron donor, electron acceptor, and biomass at days 15, 55, and 70.

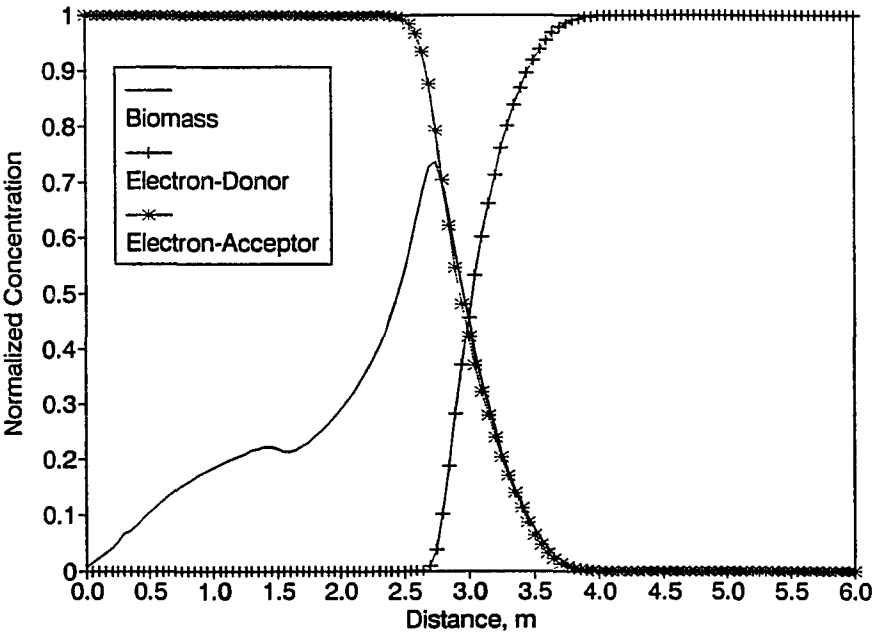


Figure 7.5. Normalized distribution of the electron donor, electron acceptor, and biomass at day 46, the beginning of a cycle.

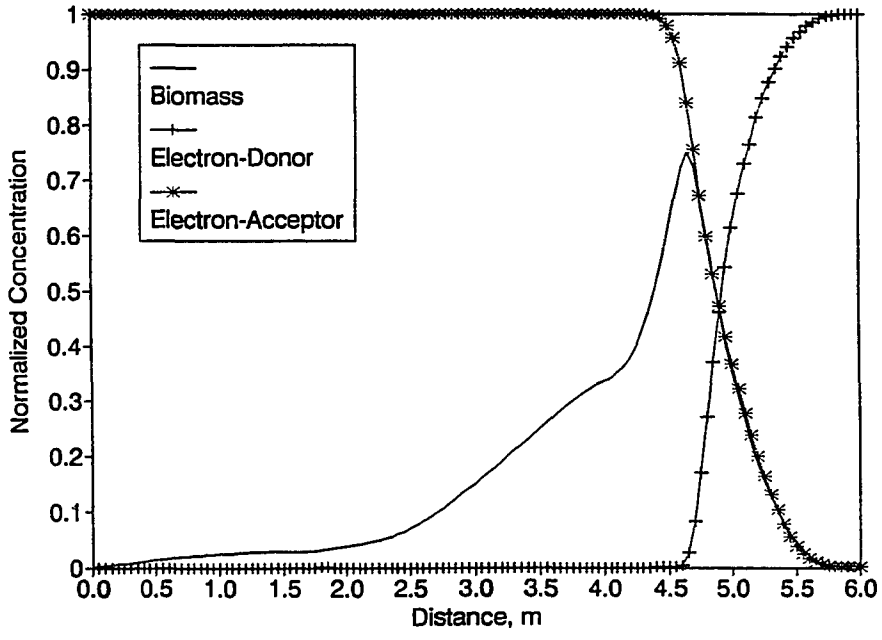


Figure 7.6. Normalized distribution of the electron donor, electron acceptor, and biomass at day 75, the end of a cycle.

speed (because the electron donor is retarded) is to mix the electron donor and electron acceptor plumes. But when mixing occurs, biological growth is induced, and the resulting utilization causes the fronts to sharpen and separate. This separation occurs because the utilization is greatest at the downstream portion of the electron acceptor front and the upstream portion of the electron donor front. Hence, the electron acceptor front slows down relative to the electron donor front, which speeds up. This is depicted at day 55 in Figure 7.4. But, because the region of electron donor and electron acceptor must overlap to have utilization, the growth diminishes, which causes the electron acceptor front to speed up relative to the electron donor. Then, overlap increases again, as shown at day 75 in Figure 7.4. This increased overlap causes increased biological activity, and the cycle begins again.

An interesting way to verify the cyclic behavior of Region 2 is to compare the normalized profiles at the beginning and end of the cycle defined by days 46 through 75. Theoretically, if the behavior is indeed cyclic, then the profiles at the end of a cycle should be a pure translation of those at the beginning. Figure 7.5 shows the normalized profiles of the electron donor, electron acceptor, and biomass for day 46, while Figure 7.6 shows the normalized profiles for day 75. We see that the profiles of the three constituents at days 46 and 75 are very similar in shape and magnitude. They are simply translated by 1.9 meters. Therefore, the hypothesis of the cyclic behavior with Region 2 is supported, and the cycle period is approximately 29 days. An average combined front speed of all three constituents can be determined by dividing the translated distance by the cycle period, i.e. 1.9 m/29 days. The value that results is 0.065 m/day. This implies that the average electron donor speed is approximately two times larger than the retarded pore–water velocity (0.033 m/day), while the average electron acceptor speed is approximately 0.65 times the pore water velocity (0.10 m/day).

In summary, when a nonsorbing electron acceptor is input into a system containing a background level of sorbing electron donor enhanced biological activity results due to the

degree of overlap and mixing of the electron acceptor and donor. This results in a rapid initial growth phase, denoted Region 1. The increase in biomass leads to an increase in the utilization of the electron donor and acceptor; utilization is greatest at the downgradient portion of the electron acceptor front and the upgradient portion of the electron donor front. Hence, the fronts tend to separate, and the initial rapid growth decreases to a steady state growth phase, denoted Region 2. However, Region 2 exhibits some very interesting oscillations about its steady state; the nature of these oscillations were described in detail and are shown in Figures 7.4–7.6. The Region 2 behavior requires that the domain be long enough that the 'steady state' biomass can build up before the electron donor front washes out of the domain. It is conceivable that Region 2 could be totally missed if the modeling or laboratory experiments were conducted over small time–space scales.

## 7.3 Effects of Velocity and Sorption Parameters on Region 1 Biodegradation

The effect of retardation of the electron donor is dependent upon many parameters that comprise the system described in Section 7.2. One of the most highly variable parameters is the velocity of the groundwater. Initial investigation into the effect of varying groundwater velocity and retardation coefficient was performed. The numerical experiments were conducted in the same system as in Section 7.2, with the only difference being a 2–m long grid, as opposed to a 6–m long grid. The results of nine cases are examined to determine the behavior of a retarded organic compound undergoing biodegradation when combined with electron–acceptor transport and biomass growth in a homogeneous system. These nine transient experiments were conducted at three velocities (0.10, 0.55 and 1.0 m/day) and three retardation factors ($R_{fS} = 1, 3$, and 10). The values of the retardation coefficients were selected in part by considering Chiang et al.'s (1989) finding of decreasing biodegradation with increasing adsorption when the retardation factor increased above three.

Because the numerical experiments were conducted with a relatively small distance of 2 m, only Region 1 behavior can be observed and examined for all of the runs. Region 2 is

not evident when the retardation factor is low and/or the velocity is high, because the electron–donor front is washed out of the system before the quasi–steady condition of Region 2 is attained. However, there is evidence of the onset of Region 2 behavior at the lowest velocity (0.10 m/day) and the highest retardation factor (10) examined.

The normalized mass of substrate biodegraded in the system for nine different experiments is shown in Figure 7.7. Based on preliminary runs, it was decided to stop the retardation simulations at day 35.0, because most of the important overall transient changes in the 2–m domain had already occurred by then. In hindsight, better runs would have resulted if a longer grid and longer times had been used. Then, Region 2 behavior could have been observed in all cases. Only the curve for $R_{fS} = 10$ and $v = 0.1$ m/day has a Region 2; the others all have an approximately straight–line portion prior to the maximum value. For all curves, the linear part of Region 1 behavior was used to represent a rate of biodegradation. The approximate slope of each linear limb of Figure 7.7 was estimated by one calculation, as opposed to calculations of the slope of the curve at every time step. A straightedge was used to identify the best slope of the linear portion of each limb, and then selected points were used to the slope. In addition, the lag period was estimated as the time from the start of the simulation until the beginning of the linear portion of the curve. The lag time values are tabulated in Table 7.1, and the Region 1 biodegradation rates are reported in Table 7.2.

The lag time values reported in Table 7.1 increase with greater $R_{fS}$ and lower velocity. The increase in the lag time as a function of increasing $R_{fS}$ illustrates that more retardation results in slowing down the initial biodegradation in the system. Chang and Rittmann (1987) reported this same behavior for bacterial growth on activated carbon. The increase in lag time for lower velocities can be understood better with the aid of the normalized lag time values shown in Table 7.1. The normalization of the lag time by $R_{fS}$ shows that the lag time changes are approximately proportional to $R_{fS}$. The relatively constant values of normalized lag time with increasing $R_{fS}$ shows that increasingly strong

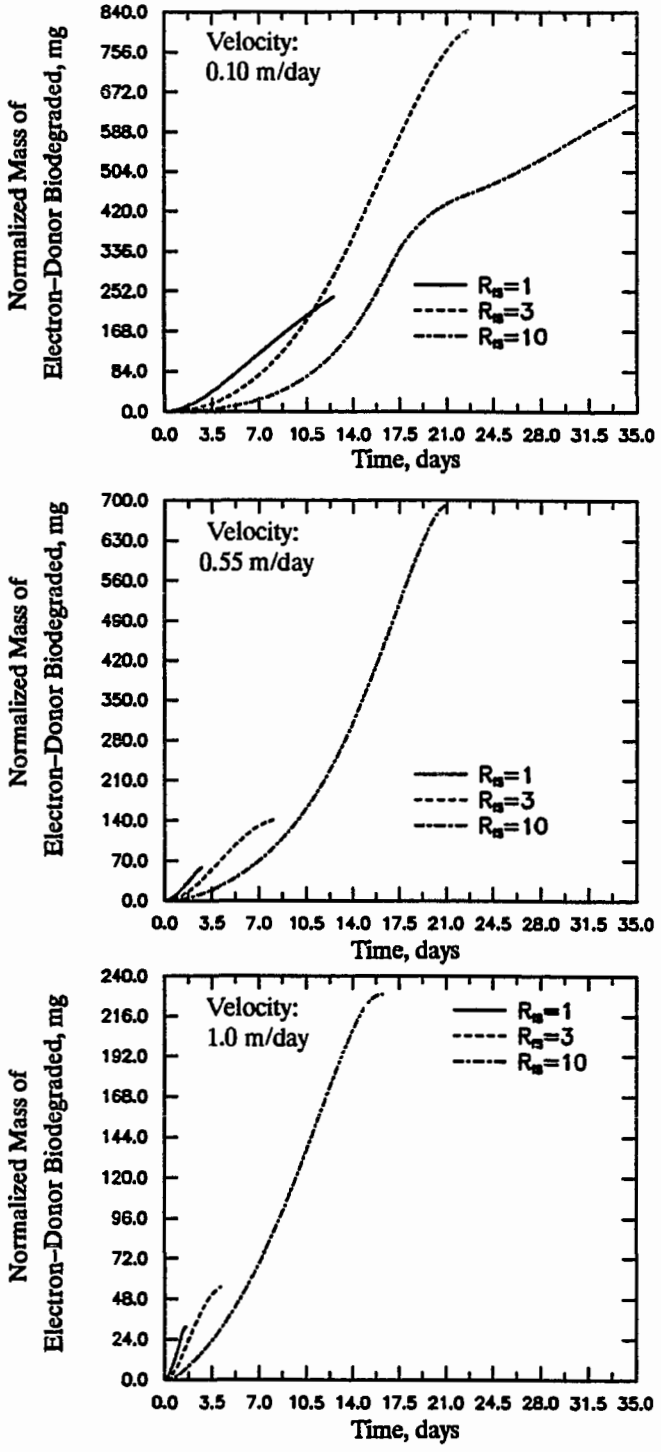


Figure 7.7. Normalized mass of electron donor biodegraded for $R_{fS}$ = 1, 3, and 10 in the one–dimensional retardation experiments for velocities of 0.10, 0.55, and 1.0 m, respectively.

Table 7.1 Approximate Lag Times to Region 1 for the Three Different Velocities in the Homogeneous Numerical Experiments (Values in Parentheses are Normalized by $R_{fS}$).

| | Lag Time (days) | | |
|---|---|---|---|
| $R_{fS}$ | v= 1.0 m/day | 0.55 m/day | 0.10 m/day |
| 1 | 0.3 (0.3) | 1.2 (1.2) | 2.6 (2.6) |
| 3 | 1.1 (0.37) | 2.5 (0.83) | 11.4 (3.8) |
| 10 | 7.0 (0.70) | 11.5 (1.15) | 14.7 (1.47) |

Table 7.2 Approximate Region 1 Biodegradation Rates of the Electron Donor for the Three Different Velocities in the Homogeneous Numerical Experiments (Values in Parentheses are Normalized by $R_{fS}$)

| | Rate of Biodegradation (mg/day) | | |
|---|---|---|---|
| $R_{fS}$ | v= 1.0 m/day | 0.55 m/day | 0.10 m/day |
| 1 | 28.4 (28.4) | 29.5 (29.5) | 23.6 (23.6) |
| 3 | 57.3 (19.1) | 72.6 (24.2) | 181. (60.3) |
| 10 | 214. (21.4) | 619. (61.9) | 510. (51.0) |

adsorption makes the substrate less available for initiating bacterial growth. The normalized lag times are inversely proportional to the flow velocity for a constant $R_{fS}$. This phenomena suggests that the flux of the electron acceptor also is limiting initiation of significant bacterial growth.

The trends with increasing retardation of the Region 1 biodegradation rate presented in Table 7.2 can be explained as follows. First, the absolute value of the linear biodegradation rate increases with increasing $R_{fS}$ for a fixed velocity, but the normalized rates change much less dramatically. These results indicate that two effects are occurring. The first effect is that adsorption creates a "reservoir" of electron donor substrate. As aqueous phase electron donor is degraded, the sorbed phase substrates desorbs (instantly,

because equilibrium is assumed). The sorbed phase, thus, is a source of substrate, and greater $R_{fS}$ makes the reservoir of substrate greater. Having a greater reservoir of electron donor prolongs the extent of high electron–donor and –acceptor overlap, which leads to more significant utilization and growth.

If the reservoir of the electron donor were the only mechanism occurring, the normalized rate values would be approximately equal. However, the normalized rates generally increases with increasing $R_{fS}$. Thus a second mechanism appears to be acting. As $R_{fS}$ increases, the speed of the electron–donor front decreases relative to that of the nonretarded electron acceptor. This results in a greater degree of overlap of the two fronts and, thus, a larger zone in which the electron donor and acceptor are simultaneously high, which leads to faster biological growth. While increased utilization of the electron acceptor causes its front to "retreat" (i.e. the electron acceptor front is "eaten" upgradient) desorption of the electron donor prevents utilization from "advancing" the electron donor front upgradient. Apparently, the increased front overlap augments the reservoir effect and (generally) allows the normalized biodegradation rate to increase with increasing $R_{fS}$.

For the case of a fixed retardation factor, it is necessary to examine the normalized biodegradation rates shown in Table 7.2. For $R_{fS} = 1$, there is little front overlap because longitudinal dispersion is the only factor causing mixing between the electron–donor and –acceptor fronts. Therefore, the biodegradation rate is roughly constant in velocity. (Note, one could interpret the slight increase with velocity as reflecting the fact that longitudinal dispersion = $\alpha_L v$ increases with v). For $R_{fS} = 3$ and 10, front overlap is enhanced due to retardation of the electron–donor front. In this case, a slow velocity allows the full front–overlap to develop within the 2–m grid and permits sufficient contact between the electron–donor and –acceptor that the biomass can grow rapidly. Therefore, for retarded cases, a velocity decrease increases the biodegradation rate within the 2–m domain. The result for $R_{fS} = 10$, $v = 0.10$ m/day is an anomaly to this trend, but this could

be due to inaccuracies in estimating a Region 1 slope: Note from Figure 7.7 that the linear Region 1 is not well defined in this case and that Region 2 behavior seems to truncate Region 1 as its slope is still increasing.

## 7.4 Summary and Conclusions

The importance of sorption processes in combination with transport processes and biodegradation kinetics was examined in a homogeneous system. More specifically, the linear equilibrium adsorption of the electron donor and its subsequent effect on the biodegradation rate gave new insight on the behavior of the homogeneous systems. Two regions of behavior, an initial rapid growth period and a long–term pseudo–steady–state, were identified in the numerical experiments for the one–dimensional homogeneous system. The apparent linear biodegradation rate of the electron donor for the initial rapid growth period also was determined for a series of different retardation factors and velocities. As the retardation factor increased, the Region 1 biodegradation rate also increased.

The following specific conclusions can be drawn from the results of the numerical experiments of transport and biodegradation in homogeneous and stratified porous media presented in this chapter.

1. The results of the experiments revealed two different linear regions, which correspond to an initial rapid growth phase (Region 1) and then a long–term pseudo steady–state of the electron donor, electron acceptor, and biomass profiles (Region 2).

2. The Region 2 cyclic phenomenon was examined in detail in order to determine the cause of this behavior. In the absence of significant biological growth, the injected electron acceptor front travels faster than the retarded electron donor front. This overlap leads to a region of simultaneously high electron donor and acceptor, which leads to biomass growth. Thus, overlap of the electron donor, electron acceptor, and biomass profiles is required in order to achieve substantial biodegradation. But, biodegradation results in utilization of electron donor and acceptor, which results in a speed up of the

retarded electron donor front and a slow down of the electron acceptor front. This separation of the fronts diminishes the region of simultaneously high electron donor and acceptor, resulting in biomass decay.

3. The lag time to the onset of Region 1 behavior increased as a result of increased sorption, which lowers the concentration of the aqueous-phase substrate, and decreased advection, which limits electron acceptor flux into the system.

4. As the retardation factor of the electron donor increases in the homogeneous experiments, the rate of biodegradation of the electron donor also increases. This is caused by the "reservoir" effect with increasing sorption of the electron donor, which is augmented further by increasing overlap of the electron donor and electron acceptor fronts. For a retarded electron donor, decreasing flow velocity increases the biodegradation rate in Region 1, and this effect is due to increasing the overlap of the electron donor and acceptor within the domain.

# 8. CONCLUSIONS

The four specific objectives were:

(a) Develop and test a computationally efficient numerical model that is flexible enough to handle alternative degradation submodels.

(b) Use the transport model to evaluate the implication of selecting alternative biodegradation submodels for simulation of *in situ* bioremediation systems; the alternative models are Monod vs. biofilm, and multiplicative vs. minimum-rate Monod.

(c) Use the transport model to investigate unique phenomena resulting from the coupling between transport and biodegradation in a stratified system.

(d) Use the transport model to investigate in detail the interaction of sorption and biodegradation.

The following are the most important specific conclusions from this work:

1. A flexible, accurate, and efficient two-dimensional groundwater solute-transport model, capable of representing various nonlinear biodegradation and adsorption kinetic models, was based upon the operator-splitting concept. The flexibility of operator splitting was achieved through the modular nature of the reaction terms, which are solved independently from the advection and dispersion terms.

2. The mass-transfer resistances incorporated by the biofilm model were insignificant in the example problem of two-dimensional solute transport. Therefore, the simpler Monod (macroscopic) model could be used in most simulations.

3. A new dimensionless number, $Da_{(mt)}=2L^*L_f^*D_f^*/S^*$, was developed in order to determine when external mass transport is important. In general, external mass transport is significant when $Da_{(mt)} >> 1$, that is when the substrate concentration is low relative to $K_S$, the biomass concentration is high, and the groundwater velocity is slow.

4. The spatial discretization of the numerical simulation was shown to have an effect on the biological resolution. As a larger spatial resolution (grid spacing) is used, the true distinctions between the biological kinetic models become blurred. A new dimensionless number was defined, $Da_{MAC} = \Delta x q_m M_T (S_{in}/(K_S + S_{in})/(\epsilon S_{in})$. The value of $Da_{MAC}$ must be kept less that about 1.0 in order in ensure proper resolution of the biological reaction.

5. For dual-limitation systems, when the K values are low enough that concentrations are in the zero-order range, MR and M kinetic expressions have a negligible difference. The absolute difference between the MR and M expressions was significant when both K values were on the order of the concentration of the electron-donor and electron-acceptor. When both substrates were in the first-order regime, the difference between the M and MR was the greatest. When one substrate was in the first-order regime and the other was in the zero-order regime, the difference between M and MR was moderate. The numerical experiments that were conducted corroborate the conclusions that were determined from the simplifications of the kinetic expressions of M and MR and showed the dramatic effect dual-limitation can have when one or both of the substrates are at subsaturating concentrations.

6. A stratified domain with a continuous source of rate-limiting substrate could be described by an equivalent homogeneous system. The average behavior of the fast and slow layers was equivalent to a homogeneous case close to steady-state. The implication is that some stratified systems could be modeled as an equivalent homogeneous system.

7. For dual-limitation kinetics in a stratified system in which the electron-acceptor is input into a domain with background electron-donor, transverse mixing across the layer interface significantly increased biomass growth and subsequent removal of the electron donor. This was due to transverse dispersion of the electron acceptor from the faster layer into the slower layer. Mixing of the electron-donor and electron-acceptor at the layer led to localized biomass growth at the interface that elongated in time.

8. The results of the numerical experiments in which a nonretarded electron acceptor is injected into a domain of retarded electron donor revealed that there are two distinct regions of transport behavior. These regions correspond to an initial rapid biomass growth phase (Region 1) followed by a long–term pseudo–steady–state of the electron donor, electron acceptor, and biomass profiles (Region 2). The Region 2 phenomenon was examined in great detail in order to determine the cause of this behavior. Since the input nonretarded electron acceptor travels faster than the background retarded electron donor, there is a large region of front overlap and biomass growth. But, as the biomass grows, the rate of electron donor and acceptor utilization increases; this tends to "eat away" the upgradient boundary on the electron donor front and the downgradient boundary of the electron acceptor front, leading to a separation of the fronts. But, as the fronts separate, the biomass decays and the rate of substrate utilization decreases. This leads to the quasi–steady state behavior of Region 2, in which the electron donor, acceptor, and biomass profiles travel together.

9. A series of one–dimensional numerical experiments was conducted to isolate the effects of sorption on biodegradation kinetics and transport. As the retardation factor of the electron donor increased, the rate of biodegradation of the electron donor also increased. This was primarily due to the "reservoir" effect, whereby the stored electron donor in the solid phase increases for increasing retardation factor. In addition, increased overlap of the electron donor and acceptor fronts caused the rate to increase more than in proportion to the increase in stored electron donor. The lag time to reach the onset of Region 1 increased with increasing retardation factor and was caused by lower initial aqueous–phase substrate concentrations at higher retardation factors. The lag time also increased with decreasing groundwater velocity, probably due to the lower advection rate of the electron acceptor into the background electron donor.

## REFERENCES


Atkinson, B. and S.Y. How. 1974. "The Overall Rate of Substrate Uptake (Reaction) by Microbial Films. Part II. Effect of Concentration and Thickness with Mixed Microbial Films." Transactions, Inst. Chem. Engrs. 52: 260–272.

Bailey, J. E., and D. F. Ollis. 1986. Biochemical Engineering Fundamentals. McGraw–Hill, NY, NY: 753 pp.

Balkwill, D.L. 1989. Distribution and Characterization of Bacteria in Deep Aquifers. summary report from "Mobility of Colloid Particles in the Subsurface:Chemistry and Hydrology of Colloid–Aquifer Interactions", Manteno NC. Oct 4–6, eds. J.F. McCarthy and F.J. Wobber, USDOE, DOE/ER–0425.

Baveye, P. and A. J. Valocchi. 1989. "An Evaluation of Mathematical Models of the Transport of Biologically Reacting Solutes in Saturated Soils and Aquifers." Water Resources Research. Vol. 25 No. 6: 1413–1421.

Bird, R.B., W.E. Stewart, and E.N. Lightfoot. 1960. Transport Phenomena. Wiley, New York, 459 pp.

Boucher, D. F. and G. E. Alves. 1959. "Dimensionless Numbers." Chemical Engineering Progress. Vol. 55, No. 9: 55–64.

Borden, R. C. and P. B. Bedient. 1986. "Transport of Dissolved Hydrocarbons Influenced by Oxygen –Limited Biodegradation– 1. Theoretical Development." Water Resources Research, Vol. 22, No.13: 1973–1982.

Bouwer, E.J. and P.L. McCarty. 1984. "Modeling Trace Organics Biotransformation in the Subsurface." Groundwater, Vol. 22, No. 4: 433–440.

Brown, R. A., G. E. Hoag, and R. D. Norris. 1987. "The Remediation Game: Pump, Dig, or Treat." Water Pollution Control Federation, Philadelphia, PA, Oct.

Celia, M. A., J. S. Kindred, and I. Herrera. 1989. "Contaminant Transport and Biodegradation, 1, A Numerical Model for Reactive Transport in Porous Media." Water Resources Research, Vol. 25, No. 6: 1141–1148.

Chang, H. T. and B. E. Rittmann. 1987. "Verification of the Model of Biofilm on Activated Carbon." Environ. Sci. Tech., Vol. 21, No. 3: 280–288.

Chiang, C. S., C. N. Dawson, and M. F. Wheeler. 1989. "Modeling of In–Situ Biorestoration of Organic Compounds in Groundwater." Research Report UH/UH/MD–68, University of Houston: 33 pp.

Colwell, F.S. 1989. "Microbiological Comparison of Surface Soil and Unsaturated Subsurface Soil from a Semiarid High Desert." Appl. and Environ. Microb. 55: 2420–2423.

Daus, A. D., E. O. Frind, and E. A. Sudicky. 1985. "Comparative Error Analysis in Finite Element Formulations of the Advection–Dispersion Equation." Adv. Water Resources, Vol. 8: 86–95.

Daus, A. D., and E. O. Frind. 1985. "An Alternating Galerkin Technique for Simulation of Contaminant Transport in Complex Groundwater Systems.: Water Resources Research, Vol. 21. No. 5: 653–664.

Dennis, Jr., J. E. and R. B. Schnabel. 1983. "Numerical Methods for Unconstrained Optimization and Nonlinear Equations" Prentice–Hall, Englewood Cliffs, NJ: 378 pp.

Frind, E. O. 1982. The Principal Direction Technique: A New Approach to Groundwater Contaminant Transport Modeling. Finite Elements in Water Resources. K. O. Holz et al. (eds,), Springer Verlag, Berlin: 13–23 – 13–41.

Frind, E. O. 1988. "Solution of the Advection–Dispersion Equation With Free Exit Boundary." Numerical Methods for Partial Differential Equations, 4: 301–313.

Frind, E. O. and D. Germain. 1986. "Simulation of Contaminant Plumes With Large Dispersive Contrast: Evaluation of Alternating Direction Galerkin Models." Water Resources Research, Vol. 22, No. 13. 1857–1873.

Frind, E. O., E. A. Sudicky, and J. W. Molson. 1989. "Three–Dimensional Simulation of Organic Transport With Aerobic Biodegradation." Proceedings of IAHS Third Scientific Assembly, Baltimore, MD, May 10–19.

Kindred, J. S. and M. A. Celia. 1989. "Contaminant Transport and Biodegradation, 2, Conceptual Model and Test Simulations." Water Resources Research, Vol. 25, No. 6. 1149–1160.

Kissel, J.C., P.L. McCarty, and R.L. Street. 1984. "Numerical Simulation of Mixed Culture Biofilm." ASCE, Env. Eng., Vol. 110, 393–411.

Harvey, R. W. and L. H George. 1987. "Growth Determinations for Unattached Bacteria in a Contaminated Aquifer." Appl. and Environ. Microb. 53: 2992–2996.

Harvey, R.W., R. L. Smith, and L. H. George. 1984. "Effect of Organic Contamination upon Microbial Distributions and Heterotrophic Uptake in a Cape Cod, Mass. Aquifer." Appl. and Environ. Microb. 48: 1197–1202.

Heath, M. S., Wirtel, S. A., and B. E. Rittmann. 1990. "Simplified Design of Biofilm Processes Using Normalized Loading Curves." J. WPCF, Vol. 62, No. 2: 185–192.

Jensen, B.K. 1989. "ATP-related Specific Heterotrophic Activity in Petroleum Contaminated and Uncontaminated Groundwaters." Canadian Journal of Microbiology, Vol. 35, 814–818.

Klotz, D. and H. Moser. 1974. "Hydrodynamic Dispersion as Aquifer Characteristic Model Experiments With Radioactive Tracers." Isotope Techniques in Groundwater Hydrology, Vol. 2. International Atomic Energy Agency, Vienna, 341–355.

Lapidus, L. and G. F. Pinder. 1982. Numerical Solution of Partial Differential Equation in Science and Engineering. New York: J. Wiley and Sons, Inc.

Lee, E. S. 1968. Quasilinearization and Invariant Imbedding. New York: Academic Press.

Mallette, M. F. 1969. Evaluation of Growth by Physical and Chemical Means. Methods in Microbiology, Vol. 1. J.R. Norris and D.W. Gibbons, eds., Academic Press, Chapter 25.

MacQuarrie, K. T. B., E. A. Sudicky, and E. O. Frind. 1990. "Simulation of Biodegradable Organic Compounds in Groundwater, 1, Numerical Formulation in Principal Directions." Water Resources Research, Vol. 26, No. 2: 207–222.

MacQuarrie, K. T. B., and E. A. Sudicky,. 1990. "Simulation of Biodegradable Organic Compounds in Groundwater, 2, Plume Behavior in Uniform and Random Flow Fields." Vol. 26, No. 2: 223–240.

Molz, F. J., M. A. Widdowson, and L.D. Benefield. 1986. "Simulation of Microbial Growth Dynamics Coupled to Nutrient and Oxygen Transport in Porous Media." Water Resources Research. Vol. 22, No. 8: 1207–1216.

Molz, F. J. and M. A. Widdowson. 1988. "Internal Inconsistencies in Dispersion–Dominated Models That Incorporate Chemical and Microbial Kinetics." Water Resources Research, Vol. 24, No. 4: 615–619.

Monod, J. 1942. Recherches sur la Croissance des Cultures Bacteriennes. Hermann, Paris.

Namkung, E., R.G. Stratton, and B.E. Rittmann. 1983. "Predicting Removal of Trace–Organic Compounds by Biofilms." J. Water Poll. Control Fed. 55: 1366–1372.

Neidhardt, F. C., J. L. Ingraham, and M. Schaechter. 1990. Physiology of the Bacterial Cell: A Molecular Approach. Sinauer Associates, Sunderland, MA. pp. 8.

Nicoud, R. M. and D. Schweich. 1989. "Solute Transport in Porous Media With Solid–Liquid Mass Transfer Limitations: Application to Ion Exchange." Water Resources Research, Vol. 25. No. 6: 1071–1082.

Odencrantz, J. E., W. Bae, A. J. Valocchi, and B. E. Rittmann. 1990. Stimulation of Biologically Active Zones in Porous Media by Electron-Acceptor Injection. J of Contam Hydrol, Vol. 6. 37-52.

Patrick, G. C. and J. F. Barker. 1986. Transport and Fate of Dissolved Aromatic Hydrocarbons and Oxygen in a Shallow Sand Aquifer. Presented at the Chapman Conference on Microbial Processes in the Transport, Fate, and *In Situ* Treatment of Subsurface Contaminants, Snowbird, Utah, October 1-3.

Rifai, H. S. and P. B. Bedient. 1990. "Comparison of Biodegradation Kinetics With an Instantaneous Reaction Model for Groundwater." Water Resources Research, Vol. 26, No. 4, 637-646.

Rittmann, B.E. and P.L. McCarty. 1980a. "Model of Steady-State Biofilm Kinetics." Biotech. and Bioengr. 22: 2343-2357.

Rittmann, B.E. and P.L. McCarty. 1980b. "Verification of Model of Steady-State Biofilm Kinetics." Biotech. and Bioengr. 22: 2343-2357.

Rittmann, B.E. and P.L. McCarty. 1981. "Substrate Flux into Biofilms of any Thickness." J. Environ. Engr. 107: 831-849.

Rittmann, B. E. and K. Dovantzis. 1983. "Dual Limitation of Biofilm Kinetics." Water Research, Vol. 17, No. 12: 1727-1724.

Saez, P.B. and B.E. Rittmann. 1988. "An Improved Pseudo-Analytical Solution for Steady-State Biofilm Kinetics." Biotech. and Bioengr. 32: 362-368.

Semprini, L. and P. L. McCarty. 1989. Biostimulation and Biotransformation Modeling." in In-Situ Aquifer Restoration of Chlorinated Aliphatics by Methanotrophic Bacteria, EPA/600/2-89/033: 172-196.

Shampine, L. F. and M.K. Gordon. 1975. Computer Solution of Ordinary Differential Equations. W. H. Freeman and Company, San Francisco.

Staps, J. J. M. 1989. "International Evaluation of In-Situ Biorestoration of Contaminated Soil and Groundwater." National Institute of Health and Environmental Protection, Bilthoven, The Netherlands, Report No. 738708006: 161-169.

Sudicky, E. A. 1983. An Advective-Diffusive Theory of Contaminant Transport for Stratified Porous Media. Ph.D. Thesis, University of Waterloo, Waterloo, Ontario.

Suidan, M. T. B. E. Rittmann, and U. K. Traegner. 1987. "Criteria Establishing Biofilm-Kinetic Types." Water Research, Vol. 21, No. 4, 491-498.

Taylor, S. W., and P. R. Jaffe. 1990. "Substrate and Biomass Transport in a Porous Medium." Water Resources Research, Vol. 26, No. 9, 2181-2194.

Todd, D.K. 1980. Groundwater Hydrology. John Wiley and Sons, New York, pp. 29.

Van Beelen, P. and A. K. Fleuren-Kemilä. 1989. "Enumeration of Anaerobic and Oligotrophic Bacteria in Subsoils and Sediment." Journal of Contaminant Hydrology, Vol. 4, No. 3: 275–284

Wheeler, M. F. 1988. "Modeling of Highly Advective Flow Problems." Proceedings of the VII International Conference of Computational Methods in Water Resources, MIT, Editors: M. A. Celia, L.A. Ferrand, C.A. Brebbia, W.G. Gray, and G. F. Pinder. Vol. 1. Computational Mechanics Publications, Elsevier: 35–44.

Wheeler, M. F. and C. N. Dawson. 1987. An Operator–Splitting Method for Advection–Diffusion–Reaction Problems. Department of Mathematical Sciences, Technical Report 87–9, Rice University

Widdowson, M. A., F. J. Molz, and L. D. Benefield. 1987. "Development and Application of a Model for Simulating Microbial Growth Dynamics Coupled to Nutrient and Oxygen Transport in Porous Media." Proceedings of the NWWA/IGWMC Conference on Solving Groundwater Problems With Models, Feb. 10–12, Denver, CO.

Widdowson, M. A., F. J. Molz, and L. D. Benefield. 1988. "A Numerical Transport Model for Oxygen– and Nitrate–Based Respiration Linked to Substrate and Nutrient Availability in Porous Media." Water Resources Research, Vol. 24, No. 9: 1553–1565.

Williamson, K. and P. L. McCarty. 1976. "A Model of Substrate Utilization by Bacterial Films" J. WPCF, Vol. 48, No. 1: 9–24.

Wilson, J.T., J. F. McNabb, D. L. Balkwill, and W. C. Ghiorse. 1983. "Enumeration and Characterization of Bacteria Indigenous to a Shallow Water–Table Aquifer." Groundwater, Vol. 21, No. 2, 134–142.

# APPENDIX

The purpose of this Appendix is to present the general procedure of finding $\eta$, the effectiveness factor for biofilm modeling. The procedure is a summary of the methodology presented by Rittmann and McCarty (1981).

The following dimensionless parameters are defined for use with the pseudo–analytical solution of Rittmann and McCarty (1981), which is appropriate for biofilms at any thickness:

$$L_f^* = \frac{L_f}{\tau}\ L^* = \frac{L}{\tau}; S_s^* = \frac{S_s}{K_S}; S^* = \frac{S}{K_S}; D_f^* = \frac{D_f}{D_m}; \tau = \left[\frac{2K_s D_f}{(q_m X_f)}\right]^{1/2} \quad (A.1)$$

where $S_s$ in the solute concentration at the biofilm/diffusion layer interface and $D_f$ is the molecular diffusion coefficient of the solute in the biofilm

The basic equation for the flux is given by the following equation

$$J^* = 2D_f^* L_f^* \eta \frac{S_s^*}{S_s^* + 1} \quad (A.2)$$

where $\eta$ = the effectiveness factor. The effectiveness factor is a measure of how deep the biofilm is. If $\eta = 1$, the biofilm is fully penetrated, and, if $\eta = 0$, the biofilm is completely deep. The method of flux determination for transient biofilm model presented by Rittmann and McCarty (1981) can be summarized as follows:

1. A starting estimate of an effectiveness factor $\eta$ is required. Rittmann and McCarty (1981) suggested starting from

$$\eta = \frac{\tanh(\sqrt{2}L_f^*)}{\sqrt{2}L_f^*}$$

2. A trial $S_s^*$ is estimated from

$$S_s^* = \frac{1}{2}[(S^* - 1 - 2L^* L_f^* D_f^* \eta) + \sqrt{(S^* - 1 - 2L^* L_f^* D_f^* \eta)^2 + 4S^*}\ ]$$

3. A trial flux is calculated from $S_s^*$.

$$J^* = 2L_f^* D_f^* \eta \frac{S_s^*}{S_s^* + 1}$$

4. A checking $S_s^{*'}$ is calculated from the external mass transport requirement

$$S_s^{*'} = S^* - J^* L^*$$

5. A value $\phi$ is computed from

$$\phi = \frac{\sqrt{2}\, L_f^*}{(1 + 2S_s^{*'})^{\frac{1}{2}}}$$

6. A checking $\eta'$ is calculated from $\phi$

$$1 - \frac{\tanh(\sqrt{2}\, L_f^*)}{\sqrt{2}\, L_f^*}\left[\frac{\phi}{\tanh\phi} - 1\right] \qquad \text{if } \phi \le 1$$

$$\frac{1}{\phi} - \frac{\tanh(\sqrt{2}\, L_f^*)}{\sqrt{2}\, L_f^*}\left[\frac{\phi}{\tanh\phi} - 1\right] \qquad \text{if } \phi \ge 1$$

7. If $\eta'$ and $\eta$ are within 0.1% of each other , then $\eta$ has converged to an acceptable value, and it is proper to proceed to the next step. If not, it is necessary to go back to step 3 and repeat the process.

8. When an acceptable value of $\eta$ is found, $J^*$ is calculated from

$$J^* = 2\eta D_f^* L_f^* \frac{S_s^*}{1 + S_s^*}$$

9. The dimensional flux is then calculated by the following expression

$$J = J^*\left(\frac{K_s D}{\tau}\right)$$

The $\eta$ iteration usually converges in no more than five iterations.

# VITA

Joseph Odencrantz was born in Millinocket, Maine in 1962. He grew up in Augusta, Maine where he graduated from Cony High School in 1980. During his high school days he worked afternoons and evenings as a bag-boy, a bottle return handler, and a grocery clerk. Upon graduation from high school, he decided to attend college.

He attended the University of Maine at Augusta for one year and then transferred to the University of Maine at Orono where he completed his undergraduate studies in Civil Engineering in 1984. During his undergraduate studies he worked as a mathematics tutor, a resident assistant in the dormitories, and as a hydrologic field assistant for the United States Geological Survey's Water Resource Division. From there he decided to attended graduate school at the University of Illinois where he completed his master's degree in water resources in the summer of 1986. During his master's study he worked one year as a research assistant for the Illinois State Water Survey's Surface Water Section. Upon completion of his master's degree, he decided to continue his graduate studies toward the doctoral degree at the University of Illinois in the Hydrosystems and Environmental Engineering Department within the Department of Civil Engineering. He started his doctoral studies in the fall of 1986 and remained in central Illinois until the completion of his graduate studies. Upon completion of his doctoral studies, he joined Levine-Fricke, Consulting Engineers and Hydrogeologists in Irvine, California.

Mr. Odencrantz is a member of several professional societies in his field of interest.